E.O. Paton Electric Welding Institute of the National Academy of Science of Ukraine
International Association “Welding”

The Paton Welding Journal

04
2025

International Scientific-Technical and Production Journal ♦ Founded in January 2000 (12 Issues Per Year)

EDITORIAL BOARD

Editor-in-Chief
Igor Krivtsun
E.O. Paton Electric Welding Institute of the NASU, Kyiv, Ukraine

Deputy Editor-in-Chief
Michael Gasik
Aalto University, Espoo, Finland

Deputy Editor-in-Chief
Jacob Kleiman
Integrity Testing Laboratory, Markham, Canada

Editorial Board Members

Serhii Akhonin
E.O. Paton Electric Welding Institute of the NASU, Kyiv, Ukraine

Chunlin Dong
Guangzhou Jiao Tong University, China

Shiyi Gao
China-Ukraine Institute of Welding,
Guangdong Academy of Sciences, Guangzhou, China

Len Gelman
The University of Huddersfield, UK

Andrey Gumenyuk
Bundesanstalt für Materialforschung und –prüfung (BAM),
Berlin, Germany

Vitalii Knysh
E.O. Paton Electric Welding Institute of the NASU, Kyiv, Ukraine

Volodymyr Korzhyk
E.O. Paton Electric Welding Institute of the NASU, Kyiv, Ukraine

Victor Kvasnytskyi
NTUU «Igor Sikorsky Kyiv Polytechnic Institute», Ukraine

Yuliia Kvasnytska
Physico-Technological Institute of Metals and Alloys
of the NASU, Kyiv, Ukraine

Leonid Lobanov
E.O. Paton Electric Welding Institute of the NASU, Kyiv, Ukraine

Eric Macdonald
The University of Texas at El Paso, USA

Anatoliy Maistrenko
V. Bakul Institute for Superhard Materials
of the NASU, Kyiv, Ukraine

Serhiy Maksymov
E.O. Paton Electric Welding Institute of the NASU, Kyiv, Ukraine

Dhanesh G. Mohan
School of Engineering University of Sunderland England,
United Kingdom

João Pedro Oliveira
Universidade NOVA de Lisboa, Portugal

Valerii Peremitko
Dniprovsky State Technical University, Kamianske, Ukraine

Valeriy Pozniakov
E.O. Paton Electric Welding Institute of the NASU, Kyiv, Ukraine

Uwe Reisgen
Welding and Joining Institute, Aachen, Germany

Massimo Rogante
Rogante Engineering, Civitanova Marche, Italy

Cezary Senderowski
Mechanics and Printing Institute, Warsaw University
of Technology, Poland

Magdalena Speicher
Kempten University of Applied Sciences, Germany

Mattias Thuvander
Chalmers University of Technology, Goteborg, Sweden

Valentyn Uchanin
Karpenko Physico-Mechanical Institute of the NASU, Lviv, Ukraine

Gerald Wilhelm
University of Applied Sciences of Munich, Germany

Yongqiang Yang
South China University of Technology, Guangzhou, China

Executive Editor
Oleksandr Zelnichenko
International Association “Welding”, Kyiv, Ukraine

Address of Editorial Office:
E.O. Paton Electric Welding Institute, 11 Kazymyr Malevych Str., 03150, Kyiv, Ukraine
E-mail: office@paton.kiev.ua; https://paton.org.ua/en/

Address of Publisher:
International Association “Welding”, 11 Kazymyr Malevych Str., 03150, Kyiv, Ukraine
Tel.: (38044) 205 23 90, E-mail: patonpublishinghouse@gmail.com; journal@paton.kiev.ua
https://patonpublishinghouse.com/eng/journals/tpwj

The Journal was registered by the National Council of Ukraine on Television and Radio Broadcasting on 09.05.2024, carrier identifier R30-04569
ISSN 0957-798X (Print), ISSN 3041-2293 (Online)
DOI: https://doi.org/10.37434/tpwj, from #01, 2020 to now; DOI: https: //doi.org/10.15407/tpwj from #01, 2014 to #12, 2019.

Subscriptions, 12 issues per year:
348 Euro — annual subscription for the printed (hard copy) version, air postage and packaging included;
288 Euro — annual subscription for the electronic version (sending issues in pdf format or providing access to IP addresses).

Representative Offices of “The Paton Welding Journal”:

BRAZIL, Arc Dynamics
Address: Nova Iguacu, Rio de Janeiro, Brazil
Daniel Adolpho, Tel.: +55 21 9 6419 5703,
E-mail: dadolpho@arcdynamics.com.br

CHINA, China-Ukraine Institute of Welding, Guangdong Academy of Sciences
Address: Room 210, No. 363 Changxing Road, Tianhe, Guangzhou, 510650, China
Zhang Yupeng, Tel.: +86-20-61086791,
E-mail: patonjournal@gwi.gd.cn

BULGARIA, Bulgarian Welding Society
Address: Blvd. Asen Yordanov No.10, Sofia 1592, Bulgaria
Pavel Popgeorgiev, Tel.: +359 899 96 22 20,
E-mail: office@bws-bg.org

POLAND, PATON EUROPE Sp. z o. o.
Address: ul. Kapitałowa 4, 35-213, Rzeszów, Poland
Anton Stepakhno, Tel.: +38067 509 95 67,
E-mail: Anton.Stepakhno@paton.ua

The content of the Journal includes articles received from authors from around the world in the field of welding, cutting, cladding, soldering, brazing, coating, 3D additive technologies, electrometallurgy, material science, NDT and selectively includes translations into English of articles from the following journals, published in Ukrainian:

- «Avtomatychne Zvaryuvannya» (Automatic Welding), https://patonpublishinghouse.com/eng/journals/as;
- «Suchasna Elektrometalurhiya» (Electrometallurgy Today), https://patonpublishinghouse.com/eng/journals/sem;
- «Tekhnichna Diahnostyka ta Neruinivnyi Kontrol» (Technical Diagnostics & Nondestructive Testing), https://patonpublishinghouse.com/eng/journals/tdnk.

© E.O. Paton Electric Welding Institute of NASU, 2025
© International Association “Welding” (Publisher), 2025

CONTENTS

ORIGINAL ARTICLES

INFORMATION

*Translated Article(s) from “Avtomatychne Zvaryuvannya” (Automatic Welding), No. 1, 2025.

**Translated Article(s) from “Avtomatychne Zvaryuvannya” (Automatic Welding), No. 2, 2025.

***Translated Article(s) from “Tekhnichna Diahnostyka ta Neruinivnyi Kontrol” (Technical Diagnostics & Nondestructive Testing), No. 1, 2025.

Indexing: The electronic edition of the Journal is stored in the V.I. Vernadsky National Library of Ukraine (eVerLib), included in the OPEN UKRAINIAN CITATION INDEX database and international databases: CROSSREF, EBSCO, Google Scholar, INDEX COPERNICUS, ULRICHSWEB.

DOI: https://doi.org/10.37434/tpwj2025.04.01

FEATURES OF INITIATION AND PROPAGATION OF FATIGUE CRACKS UNDER CYCLIC MECHANICAL LOADS ON SURFACED PLATES

I.O. Ryabtsev[1], V.V. Knysh[1], Yu. Kudryavtsev[2], A.A. Babinets[1], S.O. Solovej[1], I.I. Ryabtsev[1], I.P. Lentyugov[1]

[1]E.O. Paton Electric Welding Institute of the NASU
11 Kazymyr Malevych Str., 03150, Kyiv, Ukraine
[2]Structural Integrity Testing and Technologies (SINTEC), Inc.
Suite #469, 1136 Centre Street, Unit 3, Thornhill, ON L4J 3M8, Canada

ABSTRACT

The features of initiation and propagation of fatigue cracks were investigated at cyclic mechanical loads on specimens, deposited in one wear-resistant layer or with an additional plastic sublayer. Fundamentally different nature of propagation of fatigue cracks was revealed in the specimens, deposited with a ductile sublayer of low-carbon steel compared to the specimens without a sublayer. In the specimens deposited with a ductile sublayer unlike the specimens deposited without a sublayer when the main fatigue crack passed through the deposited layer and the sublayer, at the boundary of the wear-resistant layer and the plastic sublayer, as well as the sublayer and the base metal, branching and a kind of inhibition of the main fatigue crack are observed.

KEYWORDS: arc surfacing, cyclic loading, fatigue life, fatigue cracks, single-layer surfacing, multilayer surfacing, wear-resistant layer, ductile sublayer

INTRODUCTION

Term of service of machines and mechanisms operating in different industries, depends primarily on their operating conditions and properties of materials, from which these parts are made. Many of these parts are operating under the conditions of different kinds of wear and cyclic mechanical loads of different intensity. A combination of such operating conditions most often leads to premature, and sometimes emergency failure of these parts, as a result of fatigue fracture. It may also lead to failure of technological equipment, including such parts.

This problem is particularly relevant for mining and metallurgy, mechanical engineering and other industries, where high-efficient technological equipment is used. Stopping such equipment to replace the worn parts leads to losses from unreleased products, which can be several times higher than the direct costs of purchasing new parts and replacement of the worn ones. Such parts include cold and hot rolling rolls for various purposes; rolls of continuous casting machines; knives for cold and hot metal cutting etc. [1–4].

It is known that many of these parts are clad during manufacture. Practically all of them are many times reconditioned by the surfacing methods after a certain term of service and partial wear, and are used again [1]. During further long-term service under the conditions of simultaneous action of wear and cyclic mechanical loads fatigue cracks can initiate and propagate in the deposited and base metal, which may lead to emergency destruction of the part. Harmful tensile residual stresses induced by such manufacturing processes as welding, deposition/cladding could also significantly decrease the fatigue life of parts both at the stages of initiation and propagation of fatigue cracks. From other side the application of stress relieving techniques could significantly increase the fatigue performance [5, 6]. Therefore, relevant and important is the problem of investigations of the influence of materials and technologies, used in manufacturing and restoration surfacing of the above-mentioned parts, on their fatigue life, in particular on the peculiarities of initiation and propagation of fatigue cracks in themHighly wear-resistant carbon or high-carbon materials having poor weldability are applied for surfacing the working surfaces of the above-mentioned parts. In order to improve it, preheating or deposition of ductile sublayers and sometimes both are used [1]. Deposition of a ductile sublayer can influence the fatigue life of the surfaced part, and, primarily, the nature of initiation and propagation of fatigue cracks in it.

THE OBJECTIVE OF THE WORK

is to study the features of fatigue crack initiation and propagation under cyclic mechanical loading of the specimens, deposited in one wear-resistant layer or with additional deposition of a ductile sublayer.

INVESTIGATION MATERIALS AND PROCEDURES

In order to study the features of fatigue crack initiation and propagation, prismatic blanks of specimens from 40Kh steel of 25×45×300 mm size were prepared with 12.5×150 mm area treated for surfacing in the specimen blank center.

Copyright © The Author(s)

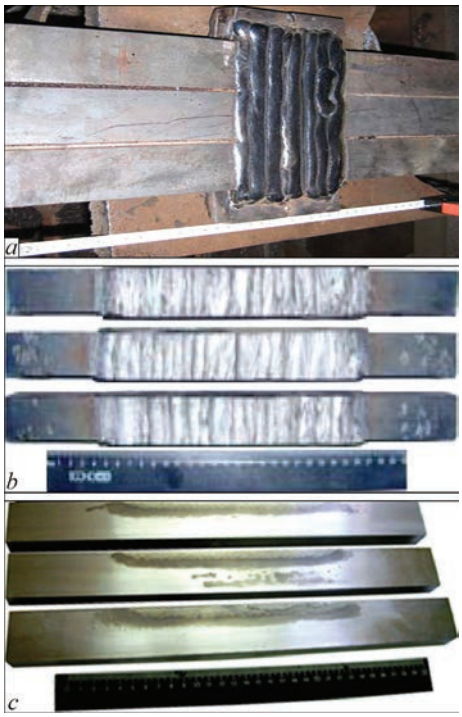

Figure 1. The blank package after surfacing (*a*), specimen blanks after cutting (*b*), specimens after final grinding (*c*)

For arc surfacing of a wear-resistant layer on specimen blanks, 2.4 mm flux-cored wire PP-Np-25Kh-5FMS was used, which provides deposited metal of the type of heat-resistant tool 25Kh5FMS steel. Surfacing was performed with fusible AN-26P flux. Solid Sv-08A wire 2 mm in diameter and fusible AN-348A flux were used for arc surfacing of a ductile sublayer.

To minimize distortion of the deposited specimens and to reduce the scope of machining work, the blanks for surfacing were stacked into a packet of 3–5 pieces, special gaskets between them were used, and they were fastened with tack-welds. Run-off tabs were welded to the sides of the packet.

Before surfacing blank packets were preheated to 250–300 °C. This was followed by automatic submerged-arc surfacing of the blank packets. Some blank packets were surfaced by PP-Np-25Kh5FMS flux-cored wire using AN-26P flux without a ductile sublayer, others — with a ductile sublayer deposited with Sv-08A wire using AN-348A flux. After surfacing, the blank packets were placed under a layer of flux for slow cooling.

After cooling each blank packet was cut along the gaskets with abrasive wheels into individual specimens. Magnitudes of deformation in the surfaced specimens were measured. The value of out-of-plane bending of the blanks in the vertical plane after surfacing did not exceed 1.5 mm on a 300 mm length, which did not require any additional straightening before specimen grinding from the four sides to the size of 20×40×300 mm with 10×150 mm deposited layer in the specimen center (Figure 1, *a–c*).

Before the start of fatigue testing, a sharp notch 1 mm deep with 0.25 mm radius in its tip was made in the deposited layer center of all the produced prismatic specimens. The initial crack was grown from the sharp notch during three-point bending with additional load from the base metal side with cycle asymmetry of 0.01 and 5 Hz frequency at the levels of maximal applied stresses, not exceeding the service stresses.

Despite the presence of a sharp notch in the specimen center, after initiation all the fatigue cracks developed on the specimen side surfaces from one or two of its side edges. Nature of fatigue cracks initiation and propagation on the specimen side surfaces was photographed and they measured using calipers.

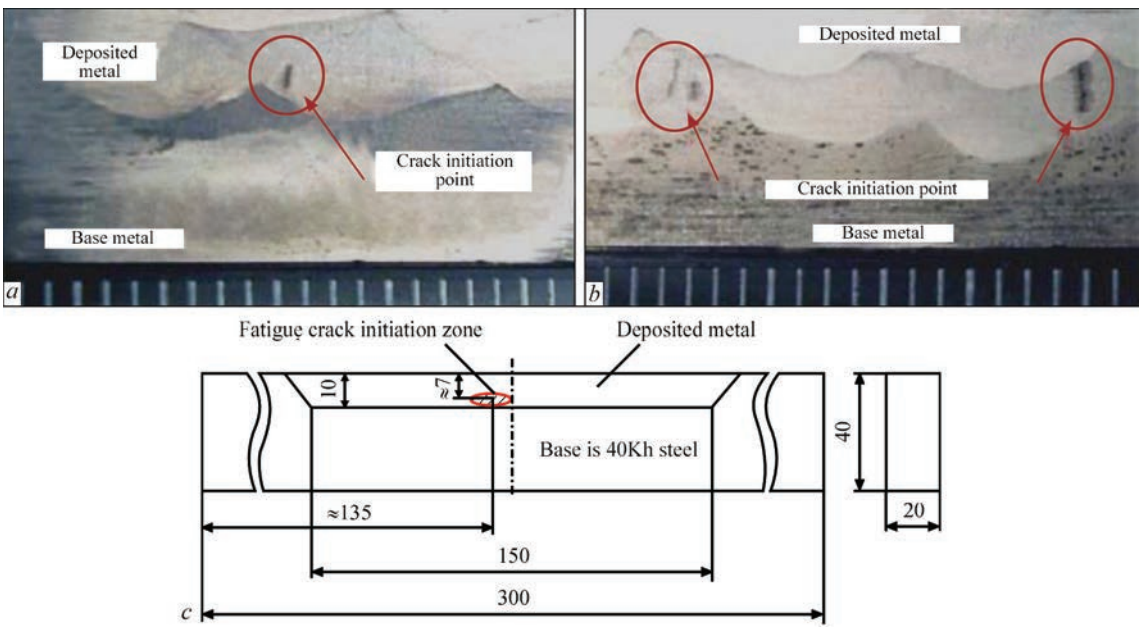

Figure 2. Points of fatigue crack initiation in specimens deposited without the sublayer (*a*, *b*), schematic image of their arrangement in the surfaced specimen (*c*)

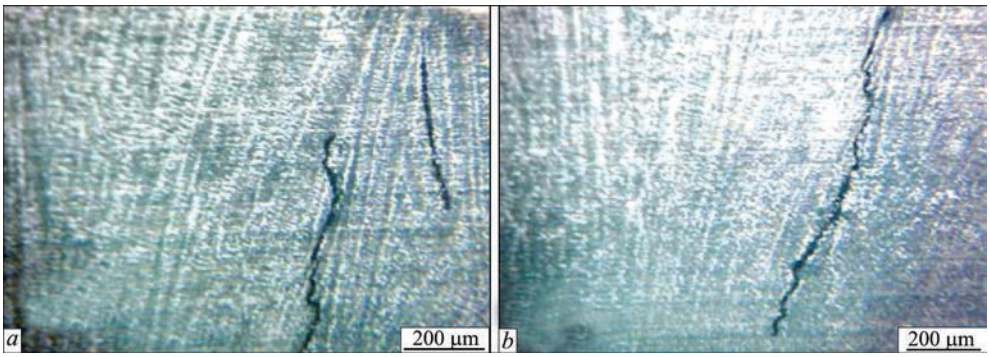

Figure 3. Nature of fatigue crack propagation in deposited metal 25Kh5FMS

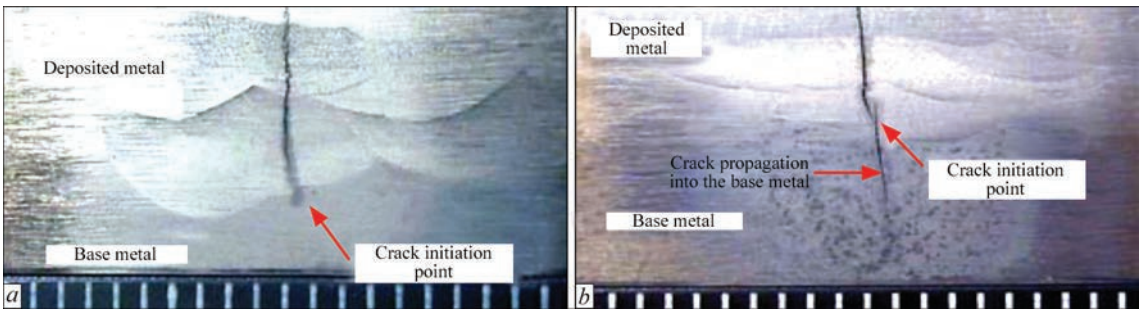

Figure 4. Nature of initiation and propagation of fatigue cracks in specimens deposited without a sublayer

INVESTIGATION RESULTS AND THEIR DISCUSSION

INITIATION AND PROPAGATION OF FATIGUE CRACKS IN SPECIMENS OF 40Kh STEEL DEPOSITED WITH PP-Np-25Kh5FMS FLUX-CORED WIRE WITHOUT A SUBLAYER

During cyclic mechanical loading in specimens deposited without a sublayer the fatigue cracks formed predominantly in the deposited layer at 1–3 mm distance from the fusion line between the base metal and the deposited wear-resistant layer (Figure 2, *a–c*).

The line of fusion of the deposited and base metal has the role of a stress concentrator, so that the fatigue cracks predominantly initiate near it (215–760 μm), and at the first stage of cyclic mechanical loading they are located in the deposited metal, which is attributable to its lower ductility and higher hardness, compared to base metal. Microstructural studies of etched sections of the specimens deposited without the sublayer after fatigue testing showed that the fatigue cracks predominantly propagate in the direction of the axes of dendrite formation in 5Kh5FMS deposited metal (Figure 3, *a*, *b*).

Several parallel cracks most often formed at the distance of 1–15 mm from each other and, as a rule, near the fusion zones of two adjacent beads (Figure 4, *a*). During fatigue testing, the cracks first propagated in the deposited metal only towards the surface. Having passed the entire deposited metal, the cracks started propagating in the other direction — towards the base metal (Figure 4, *b*). After the crack reaching and propagating through the base metal, specimen destruction took place.

INITIATION AND PROPAGATION OF FATIGUE CRACKS IN SPECIMENS OF 40Kh STEEL, DEPOSITED WITH PP-Np-25Kh5FMS WIRE WITH A LOW-CARBON STEEL SUBLAYER

As in the case of specimens deposited without a sublayer, in specimens deposited with a sublayer, a sharp notch 1 mm deep with 0.25 mm radius at the tip was made in the deposited layer center, from which the initial crack up to 1 mm deep was grown.

When studying the kinetics of fatigue crack growth during cyclic mechanical loading it was determined that the main fatigue crack propagates predominantly along the fusion boundary of individual beads. No fatigue cracks parallel to the main one, were found in specimens with a low-carbon sublayer (unlike specimens without the sublayer). However, during fatigue fracture, side branches from the main crack were observed in the zones of transition of one metal layer into another one, which propagated along the fusion line of the wear-resistant layer with the sublayer (Figure 5) and along the line of fusion of the sublayer with the base metal (Figure 6). After the crack has passed the wear-resistant layer and

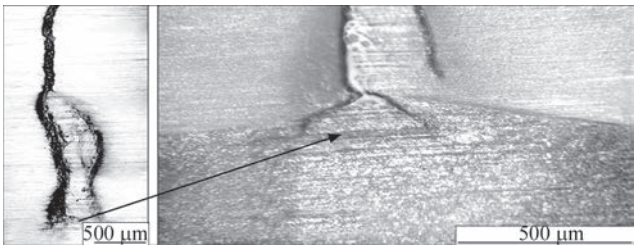

Figure 5. Fatigue crack branching near the fusion boundary of the wear-resistant layer and the sublayer

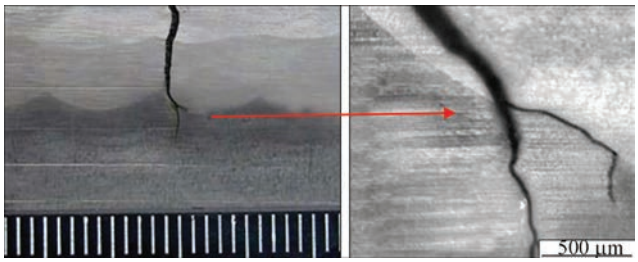

Figure 6. Fatigue crack branching near the fusion boundary of the sublayer and the base metal

the sublayer from low-carbon steel, specimen destruction occurred in the base metal.

Such kinetics of specimen fatigue fracture is explained by manifestation of several factors. First, a zone of chemical and structural heterogeneity is located in the zone of overlapping of adjacent deposited beads, which has a negative influence on material properties [7]. Secondly, during multibead multilayer surfacing relatively sharp angles can form on the fusion boundary of adjacent beads and layers, which will be stress concentrators, and which will initiate formation of side cracks along the fusion line, accordingly [8, 9].

Thus, similar to specimens deposited without a sublayer, it is found that the fusion boundaries of individual beads and layers have an important role in the process of fatigue fracture of the surfaced parts, as the cracks mainly propagate either along the fusion boundary of individual beads, or directly near this boundary (Figure 6).

The only important difference between these two surfacing technologies as regards fatigue crack propagation consists in formation of side branches from the main fatigue crack during deposition with a sublayer, leading to a kind of deceleration of these cracks.

CONCLUSIONS

Proceeding from the conducted experimental studies, a fundamentally different mode of fatigue crack development was found in the specimens deposited with a ductile sublayer from low-carbon steel, compared to specimens deposited without the sublayer. In specimens, deposited with a ductile sublayer, during the main fatigue crack passing through the deposited layer, branching and a kind of deceleration of the main fatigue crack occur on the boundary of the wear-resistant layer and the ductile interlayer, as well as the sublayer and the base metal.

REFERENCES

1. Ryabtsev, I.A., Senchenkov, I.K., Turyk, E.V. (2015) *Surfacing. Materials, technologies, mathematical modeling* [in Russian]. Gliwice, Poland.
2. Makhnenko, V.I. (2006) *Safe service life of welded joints and assemblies of modern structures* [in Russian]. Kyiv, Naukova Dumka.
3. Kravtsov, T.G., Stalnichenko, O.I., Olejnik, N.V. (1994) *Surfacing restoration of parts and assessment of their strength* [in Russian]. Kyiv, Vyshcha Shkola.
4. Marek, A., Junak, G., Okrajni, J. (2009) Fatigue life of creep resisting steels under conditions of cyclic mechanical and thermal interactions. *Archives of Mater. Sci. and Eng.*, 40(**1**), 37–40.
5. Kudryavtsev, Y. (2008) *Residual stress*: Springer Handbook on Experimental Solid Mechanics, 371–387.
6. Kudryavtsev, Y. (2019) *Fatigue improvement of welded elements by ultrasonic impact treatment — 30 years of practical application*. IIW Doc. XIII-2803–19.
7. Du Toit, M., Van Niekerk, J. (2010) Improving the life of continuous casting rolls through submerged arc cladding with nitrogen-alloyed martensitic stainless steel. *Welding in the World*, 54(**11–12**), R342–R349. DOI: https://doi.org/10.1007/BF03266748
8. Kaierle, S., Overmeyer, L., Alfred, I. et al. (2017) Single-crystal turbine blade tip repair by laser cladding and remelting. *CIRP J. of Manufacturing Sci. and Technol.*, **19**, 196–199. DOI: https://doi.org/10.1016/j.cirpj.2017.04.001
9. Caccese, V., Blomquist, P.A., Berube, K.A.et al. (2006) Effect of weld geometric profile on fatigue life of cruciform welds made by laser/GMAW processes. *Marine Structures,* 19(**1**), 1–22. DOI: https://doi.org/10.1016/j.marstruc.2006.07.002

ORCID

I.O. Ryabtsev: 0000-0001-7180-7782,
V.V. Knysh: 0000-0003-1289-4462,
Yu. Kudryavtsev: 0009-0002-9456-7149,
A.A. Babinets: 0000-0003-4432-8879,
S.O. Solovej: 0000-0002-1126-5536,
I.I. Ryabtsev: 0000-0001-7550-1887,
I.P. Lentyugov: 0000-0001-8474-6819

CONFLICT OF INTEREST

The Authors declare no conflict of interest

CORRESPONDING AUTHOR

I.O. Ryabtsev
E.O. Paton Electric Welding Institute of the NASU
11 Kazymyr Malevych Str., 03150, Kyiv, Ukraine.
E-mail: ryabtsev39@gmail.com

SUGGESTED CITATION

I.O. Ryabtsev, V.V. Knysh, Yu. Kudryavtsev, A.A. Babinets, S.O. Solovej, I.I. Ryabtsev, I.P. Lentyugov (2025) Features of initiation and propagation of fatigue cracks under cyclic mechanical loads on surfaced plates. *The Paton Welding J.*, **4**, 3–6.
DOI: https://doi.org/10.37434/tpwj2025.04.01

JOURNAL HOME PAGE

https://patonpublishinghouse.com/eng/journals/tpwj

Received: 26.08.2024
Received in revised form: 24.10.2024
Accepted: 29.04.2025

DOI: https://doi.org/10.37434/tpwj2025.04.02

MAGNETIC PULSE TREATMENT OF WELDED JOINTS IN FUSION WELDING

L.M. Lobanov[1], M.O. Pashchyn[1], O.L. Mikhodui[1], A.N. Timoshenko[1], K.V. Shyian[1], O.M. Karlov[2], I.P. Kondratenko[2], R.S. Kryshchuk[2], V.V. Chopyk[2]

[1]E.O. Paton Electric Welding Institute of the NASU
11 Kazymyr Malevych Str., 03150, Kyiv, Ukraine. E-mail: olha.mikhodui@gmail.com
[2]Institute of Electrodynamics of the NASU
56 Beresteiskyi Prosp, 03057, Kyiv, Ukraine. E-mail: ied1@ied.org.ua

ABSTRACT

Treatment with a pulsed electromagnetic field (TPEMF) of welded joints leads to a decrease in the level of residual welding stresses. TPEMF in the welding process contributes to an increase in the efficiency of the welding process (compared to TPEMF after welding) and the simplicity of its technical implementation. On the basis of mathematical modeling and experimental studies of magnetic pulse processes, an automated complex for TIG welding has been developed that is compatible with the TPEMF of the weld metal under the conditions of a thermal deformation welding cycle.

KEYWORDS: pulsed electromagnetic field, welded joints, residual welding stresses, TIG welding, structure dispersion, mathematical modeling, aluminium alloy

INTRODUCTION

Industrial development initiates research into progressive technologies to improve the service properties of welded structures. A promising method in this area is treatment with a pulsed electromagnetic field (TPEMF) of welded joints [1–20]. Based on investigation results [1–5, 11] it should be noted that the impact of a pulsed electromagnetic field (PEMF) is an effective tool of influencing the stressed state of the welded joints. The effectiveness of the impact is enhanced at its application under the conditions of welding [5]. TPEMF can be the base for development of effective technologies of controlling the stress-strain state of the welded joints from non-ferromagnetic metallic materials, which include aluminium alloys, applied in the aerospace and ship-building industry.

THE OBJECTIVE

of this work is development of scientific principles of TPEMF application during welding of non-ferromagnetic materials in the case of aluminium alloy AMg6.

INVESTIGATION PROCEDURE

Increase in TPEMF effectiveness during welding, compared to treatment at room temperature, is based on the following principles: increase in welding process productivity as a result of transition from sequential to simultaneous performance of the main technological operations; possibility of automation; improvement of treatment effectiveness to reduce the residual welding stresses, in keeping with the mechanism, given in [11]; dispersion of the weld metal structure during magnetodynamic impact under the conditions of increased temperatures; use of assembly fixture elements as screens to increase the magnitude of electromagnetic pressure on the treated metal.

It is known that at flowing of an electric current pulse (ECP) in the inductor conductors, eddy currents are excited in the adjacent electrically conductive medium. As was proved in [12, 13], interaction of the induced currents with PEMF which excited these currents, generates electrodynamic force P. Its normal component applies active load to the metallic material section being treated, and, as a result, changes its stressed state. Under the condition that density j of the induced electric current reaches the value of $j \geq 1$ kA/mm^2 in the metal being treated, conditions are in place for realization of the electroplasticity effect (EPE) [11–13]. This promotes intensification of plastic deformation of the material and, as a consequence, relaxation of its residual stressed state. A flat inductor with 95 mm outer diameter and inductance L = 120 μH was used for TPEMF realization [12]. A power source based on a capacitor system of the general capacity C = 5140 μF, charging voltage U of up to 800 V, and stored energy $E_{st} \sim 1.6$ kJ was used for PEMF generation. To assess TPEMF effectiveness, specimens in the form of a disc of thickness $\delta = 1$ mm and diameter D_s = 90 mm from aluminium alloy AMg6 with a TIG weld were used. Welded joints on the disc surface were made in the form of a ring with diameter D_w = 5 mm. Thus, there was a distance of 45 mm between the weld and the free edge of the disc.

The method of electron speckle-interferometry [12, 14] was used for assessment of σ_x of the tangen-

Copyright © The Author(s)

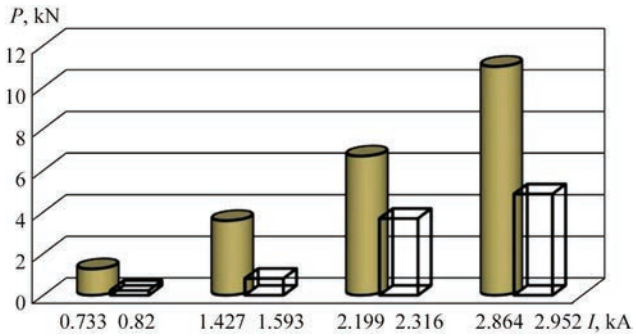

Figure 1. Influence of ECP amplitude values — *I* on pressure *P* during TPEMF of specimens of circumferential welded joints from AMg6 alloy with δ = 10 mm: □ — TPEMF without a screen; ■ — TPEMF with a screen

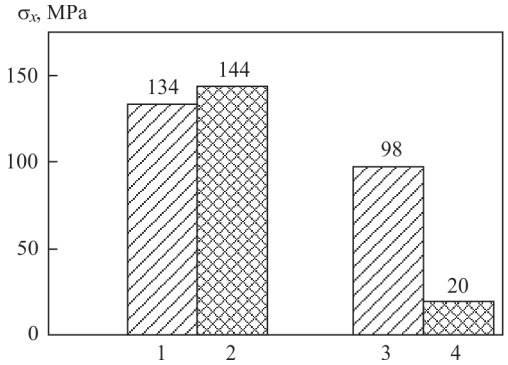

Figure 2. Influence of the weld TPEMF without application (*1*, *3*) and with application (*2*, *4*) of a screen on residual stresses σ_x in the weld metal of AMg6 alloy welded joint: *1*, *2* — before TPEMF; *3*, *4* — after TPEMF

tial component of the welded joint stressed state in points on the line of the circumferential weld.

INVESTIGATION RESULTS

TPEMF of specimens of thickness δ = 1.0 mm and an assembly of a specimen with δ = 1.0 mm and current-conducting screen from AMg6 alloy also in the form of a disc with δ = 5.0 mm (Σδ = 6 mm) and a diameter of 90 mm was performed. TPEMF was conducted as a series of eight ECP in a mode with increase of *U* values in the following sequence: U_1 = 200 V, U_2 = 400 V, U_3 = 600 V; U_4–U_8 = 800 V. ECP at U_1–U_3 facilitated gradual achievement of the nominal mode, and ECP at U_4–U_8 promoted generation of PEMF for specimen treatment. Selection of the quantity of ECP in the nominal treatment mode (at the voltage of 800 V) was based on the results of [15].

In [16] evaluation of intensity *H* of the inductor magnetic field used in this work, was performed with application of a procedure based on Hall sensor. It was found that *H* values of the inductor at capacitor discharge at voltage *U* = 200 and 500 V reached 10 and 30 kA/m, respectively.

With increase in the thickness, electromagnetic force *P* will rise, as it is defined as an integral value in a certain volume, which is confirmed by the data in Figure 1 and the results of [12]. With δ increase to 6.0 mm (due to the screen application), *P* values rise more than two times, compared to TPEMF of specimens with δ= 1.0 mm without a screen. For effective treatment of thin specimens, the current pulse duration should be decreased. Such a method, obviously, requires a change in the discharge circuit parameters, which is not rational. A simpler and more effective approach is proposed in the work in the form of applying additional layers of a similar material, with which the equivalent thickness will be optimal in terms of achieving the largest value of force *P* of electromagnetic pressure. The proposed approach is similar to application of metal "satellites" in the technology of electromagnetic forming, for instance expansion or crimping [10, 11, 17]. Figure 2 gives the distributions of residual stresses σ_x before TPEMF, as well as σ_x after TPEMF of the specimen with and without application of the screen, which confirm the effectiveness of screening during TPEMF. In view of the above, it should be noted that TPEMF can be an effective method of controlling the residual stressed state of welded structures from aluminium alloys. Results of

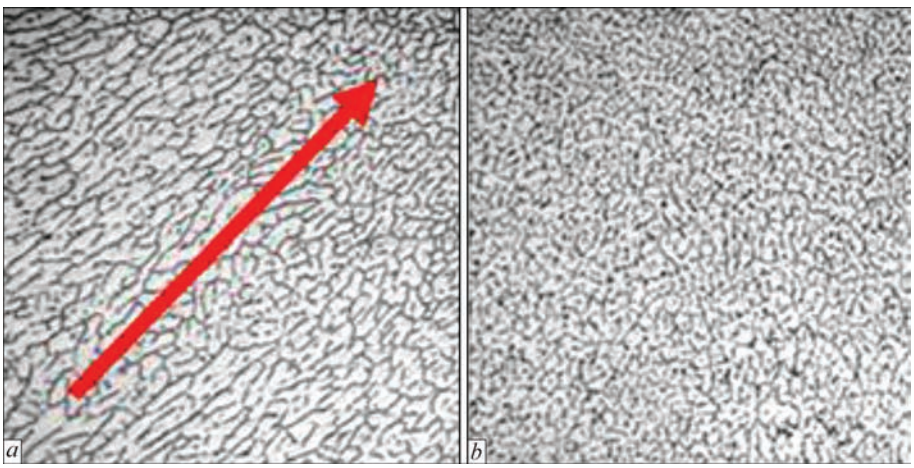

Figure 3. Microstructure (×200) of the metal of AMg6 alloy weld: in the initial state (before TPEMF) (*a*), where the arrow shows the direction of crystal growth; after TPEMF (*b*)

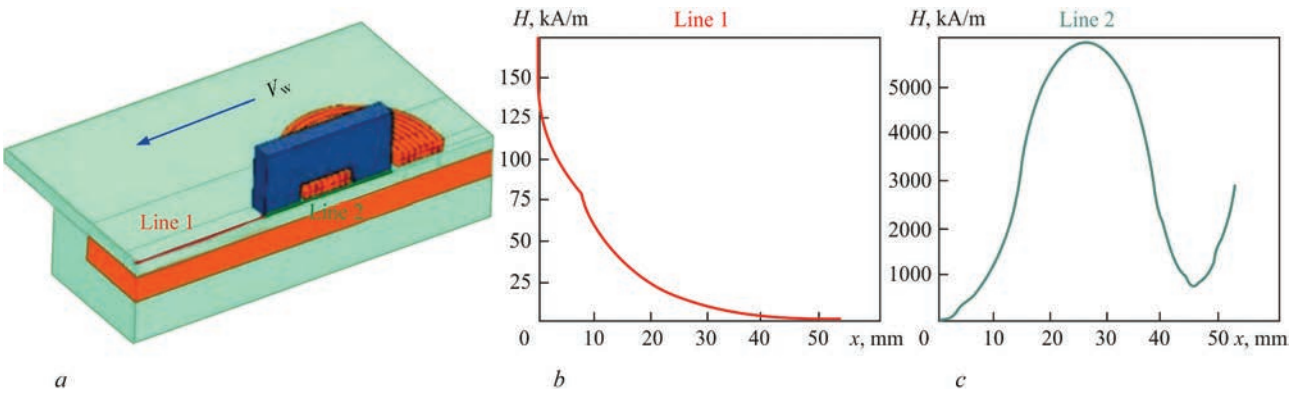

Figure 4. Mathematical modeling of electrophysical parameters of TPEMF (weld) during welding; *a* — schematic of a U-shaped TPEMF inductor along the welding direction V_w; *b* — distribution of TPEMF intensity *H* along line 1; *c* — distribution of TPEMF intensity *H* along line *2*

metallographic investigations of specimens before and after TPEMF confirmed the positive influence of treatment on evolution of the weld metal structure (Figure 3). In the general case the microstructure is a light matrix — an α-solid solution with precipitation of the excess phase in the form of a network along the crystal boundaries. However, while without TPEMF the crystals are of a predominantly elongated shape, oriented along the direction of their growth (arrow in Figure 3, *a*), after TPEMF with screening an equiaxed orientation of the grains is observed (Figure 3, *b*), which is accompanied by their refinement. Obtained results are attributable to dynamic impact of force *P* and eddy currents on intergranular boundaries during TPEMF, accompanied by local Joule heating of the grains [18–20].

Based on the results of [20], mathematical modeling of electrophysical parameters of TPEMF of the weld during welding was performed. Modeling results (Figure 4) should promote optimization of TPEMF parameters for relaxation of residual stresses in sheet welded joints. Figure 4, *a* shows the scheme of positioning a U-shaped inductor along the welding direction V_w (arrow) for TPEMF, where line 1 is the weld surface in front of the inductor, line 2 is in the zone of direct TPEMF impact on the weld metal. Figure 4, *b* shows the distribution of intensity *H* of PEMF, which allows determination of the optimal position of the inductor relative to the welding torch, which is determined by maximum value *H* along line 1 (beginning of the line on the side surface of a U-shaped inductor). From the results in Figure 4, *b* we can come to the

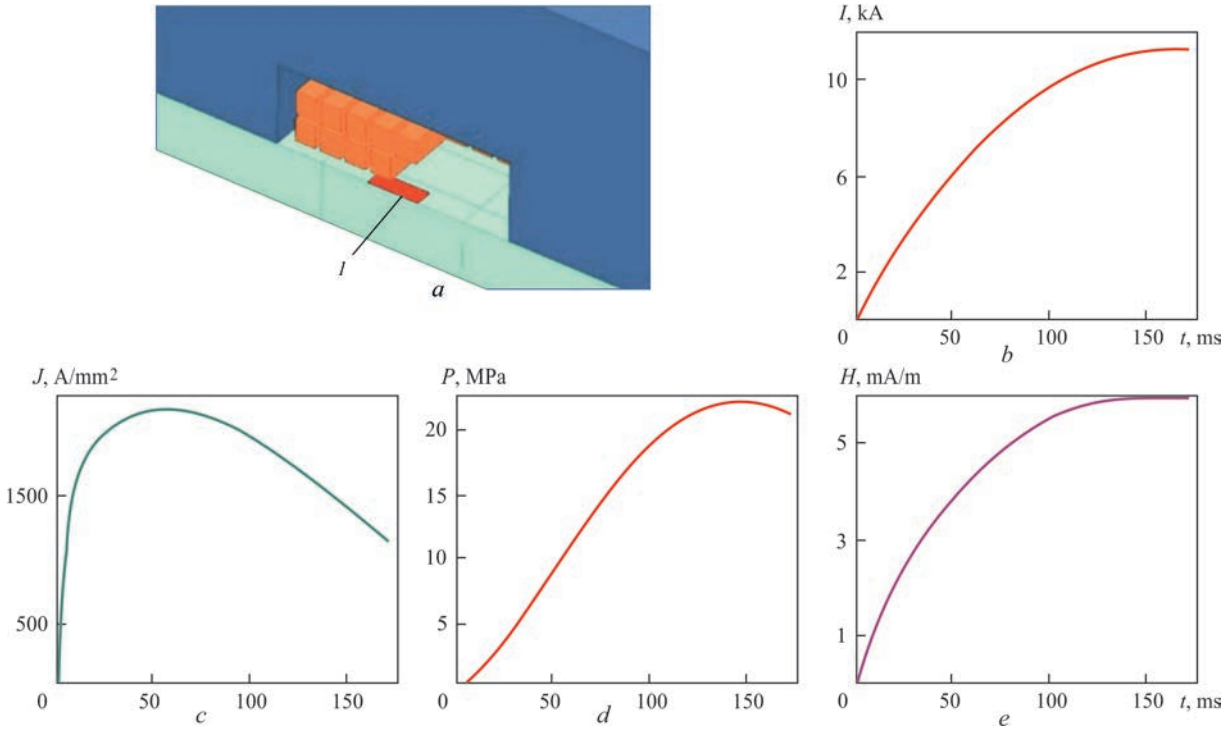

Figure 5. Results of modeling the time distributions of electrophysical parameters of the weld TPEMF (for explanations of Figure 5, *a–d* see the text)

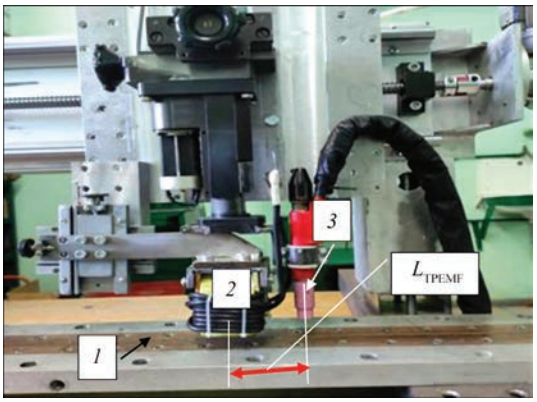

Figure 6. Automated complex for TIG welding under the conditions of accompanying TPEMF of the weld: *1* — forming backing acting as a screen; *2* — inductor; *3* — torch; L_{TPEMF} is the distance between the torch and line 1 of the indoor (Figure 4)

conclusion that at 40 mm distance from the edge of the magnetic core ($x = 0$), H value is close to zero. The diagram in Figure 4, *b* allows determination of the distance between the inductor and the welding torch, on which PEMF influence on the welding process is minimal. Figure 4, *c* shows H distribution of TPEMF along line 2 (Figure 4, *a*).

Figure 5 gives the results of modeling the time distributions of electrophysical parameters of the weld TPEMF. In Figure 5, *a* area *I* of 3.5×5.0 mm size is highlighted (which corresponds to the weld pool rear edge), for which we determined average current density J (Figure 5, *c*) and average value of pressure P (Figure 5, *d*) during the impact of ECP — *I* (Figure 5, *b*) on the solidifying weld, which promotes relaxation of welding stresses. At moment of time of about 50 μs the average current density J on the metal surface is close to 2200 A/mm^2 (Figure 5, *c*), while pressure P reaches the maximal value of 23 MPa at 150 μs (Figure 5, *d*). This should provide relaxation of welding stresses at the stage of their formation during the weld solidification due to realization of electroplasticity effect [7]. Figure 5, *e* gives the distribution of PEMF intensity H in the inductor cross-section for the moment of highest I and H values of PEMF, providing stress relaxation.

Based on the results of investigations [1–8, 11–12, 20], an automated complex was developed for TIG welding under the conditions of TPEMF of the solidifying metal of the weld (Figure 6), where forming backing *I* from a non-ferromagnetic material is used as the screen (enhancing the action of force P), and distance L_{TPEMF} between line 1 (Figure 4) of inductor *2* and TIG torch *3* ensures the maximal efficiency of TPEMF during welding.

CONCLUSIONS

1. It is shown that TPEMF has a positive effect on the residual stressed state and structure of the welded joints, and the effectiveness of the impact is enhanced under the TIG welding conditions.

2. It was established that improvement of TPEMF effectiveness during welding, compared to treatment at room temperature, is based on increase of the welding process productivity, as a result of transition from successive to simultaneous performance of the main technological operations, possibility of treatment automation, and positive influence of the thermal cycle of welding.

3. It is shown that TPEMF application promotes lowering of residual stresses and refinement of the weld metal structure in welded joints of AMg6 alloy.

4. A mathematical model of the TPEMF process was developed, on the base of which it was proved that the value of electrophysical parameters of treatment ensure relaxation of the residual stresses through realization of the electroplasticity effect.

5. An automated complex for TIG welding under the conditions of accompanying TPEMF was developed and produced, proceeding from the results of mathematical modeling and experimental studies of the magnetic-pulse processes.

REFERENCES

1. Lobanov, L.M., Pashchin, N.A., Cherkashin, A.V. et al. (2012) Efficiency of electrodynamic treatment of aluminium alloy AMg6 and its welded joints. *The Paton Welding J.*, **1**, 2–6.
2. Lobanov, L.M., Pashchin, N.A., Mihodui, O.L. (2014) Repair of the AMg6 aluminum alloy welded structure by the electric processing method. *Weld. Res. Appl.*, **1**, 55–62.
3. Lobanov, L.M., Pashchin, N.A., Yashchuk, V.A., Mikhodui, O.L. (2015) Effect of electrodynamic treatment on the fracture resistance of the AMg6 aluminum alloy under cyclic loading. *Strength of Materials*, **47**, 447–453. DOI: https://doi.org/10.1007/s11223-015-9676-5
4. Lobanov, L.M., Pashchin, N.A., Timoshenko, A.N. et al. (2017) Effect of the electrodynamic treatment on the life of AMg6 aluminum alloy weld joints. *Strength of Materials*, **49**, 234–238. DOI: http://dx.doi.org/10.1007/s11223-017-9862-8
5. Korzhik, V.N., Pashchin, N.A., Mikhodui, O.L. et al. (2017) Comparative evaluation of methods of arc and hybrid plasma-arc welding of aluminum alloy 1561 using consumable electrode. *The Paton Welding J.*, **4**, 30–34. DOI: https://doi.org/10.15407/tpwj2017.04.06
6. Batygin, Y.V., Lavinsky, V.I., Khimenko, L.T. (2003) *Pulsed magnetic fields for advanced technologies*. Ed. by Yu.V. Batygin. Kharkov, MOST-Tornado [in Russian].
7. Andrea, D., Burleta, T., Körkemeyerb, F. et al. (2019) Investigation of the electroplastic effect using nanoindentation. *Materials & Design*, **183**, 108153. DOI: https://doi.org/10.1016/j.matdes.2019.108153
8. Nayanathara Hendeniya, Gayan Aravinda Abeygunawardena, Indika De. Silva, Shiranga Wickramasinghe (2020) The tensile electroplasticity of low carbon steel with low amplitude pulse current. In: *2020 Moratuwa Engineering Research Conf. (MERCon)*, 165–169. DOI: https://doi.org/10.1109/MERCon50084.2020.9185238
9. Turenko, A.N., Batygin, Y.V., Gnatov, A.V. (2009*)* Pulsed magnetic fields for advanced technologies. Monography. In: Vol.3. *Theory and experiment of attraction of thin-walled*

metals by pulsed magnetic fields. Kharkiv, KhNADU [in Russian].
10. Batygin, Y.V., Lavinskyi, V.I., Khavin, V.L. (2009) *Method of magnetic pulsed processing of thin-walled metal billets.* Pat. UA 74909, 15.02.2006 [in Ukrainian].
11. Lobanov, L.M., Pashchyn, M.O., Mikhodui, O.L. et al. (2022) Stress-strain state of welded joints of AMg6 alloy after electrodynamic treatment during welding. *Strength of Materials*, 54(**6**), 983–996. DOI: https://doi.org/10.1007/s11223-023-00474-y
12. Lobanov, L.M., Pashchyn, M.O., Mikhodui, O.L. (2021) Pulsed electromagnetic field effect on residual stresses and strains of welded joints of AMg6 aluminum alloy. *Strength of Materials*, 53(**6**), 834–841. DOI: https://doi.org/10.1007/s11223-022-00350-1
13. Vasetsky, Y.M., Dzyuba K.K. (2017) Analytical method of calculation of quasi-stationary three-dimensional electromagnetic current field flowing along a contour of arbitrary configuration near an electrically conductive body. *Tekhnichna Elektrodynamika,* **5**, 7–17 [in Russian]. DOI: https://doi.org/10.15407/techned2017.05.007
14. Lobanov, L.M., Pivtorak, V.A., Savitsky, V.V., Tkachuk, G.I. (2006) Procedure for determination of residual stresses in welded joints and structural elements using electron speckle-interferometry. *The Paton Welding J.,* **1**, 24–29.
15. Lobanov, L.M., Pashchin, N.A., Mikhodui, O.L. (2012) Influence of the loading conditions on the deformation resistance of AMg6 alloy during electrodynamic treatment. *Strength of Materials*, 44(**5**), 472–479. DOI: https://doi.org/10.1007/s11223-012-9401-6
16. Lobanov, L.M., Pashchin, N.A., Cherkashin, A.V. et al. (2012) Repair welding of intermediate cases of aircraft engines from high-temperature magnesium alloy ML10 with application of electrodynamic treatment. *The Paton Welding J.*, **11**, 28–33.
17. Belyi, I.V., Fertik, S.M., Khimenko, L.T. (1977) *Handbook on magnetic pulse treatment of metals.* Kharkiv, Vyshcha Shkola [in Russian].
18. Batygin, Yu.V., Chaplygin, E.A. (2006) Eddy currents in flat sheet metal blanks. *Elektrotekhnika i Elektromekhanika*, **5**, 54–59 [in Russian].
19. Strizhalo, V.A., Novogrudsky, L.S., Vorobiev, E.V. (2008) *Strength of materials at cryogenic temperatures with regard to the influence of electromagnetic fields*. Kyiv, IPP [in Russian].
20. Rashchepkin, A.P., Kondratenko, I.P., Karlov, O.M., Kryshchuk, R.S. (2019) Electromagnetic field of an inductor with a W-shaped core for magnetic pulse treatment of materials. *Tekhnichna Elektrodynamika*, **6**, 5–12 [in Ukrainian]. DOI: https://doi.org/10.15407/techned2019.06.005

ORCID
L.M. Lobanov: 0000-0001-9296-2335,
M.O. Pashchyn: 0000-0002-2201-5137,
O.L. Mikhodui: 0000-0001-6660-7540,
K.V. Shyian: 0000-0001-9198-6554,
O.M. Karlov: 0000-0002-1350-1870,
I.P. Kondratenko: 0000-0003-1914-1383,
R.S. Kryshchuk: 0000-0002-1933-0144,
V.V. Chopyk: 0000-0002-5046-5223

CONFLICT OF INTEREST
The Authors declare no conflict of interest

CORRESPONDING AUTHOR
O.L. Mikhodui
E.O. Paton Electric Welding Institute of the NASU
11 Kazymyr Malevych Str., 03150, Kyiv, Ukraine.
E-mail: olha.mikhodui@gmail.com

SUGGESTED CITATION
L.M. Lobanov, M.O. Pashchyn, O.L. Mikhodui, A.N. Timoshenko, K.V. Shyian, O.M. Karlov, I.P. Kondratenko, R.S. Kryshchuk, V.V. Chopyk (2025) Magnetic pulse treatment of welded joints in fusion welding. *The Paton Welding J.*, **4**, 7–11. DOI: https://doi.org/10.37434/tpwj2025.04.02

JOURNAL HOME PAGE
https://patonpublishinghouse.com/eng/journals/tpwj

Received: 08.01.2025
Received in revised form: 28.02.2025
Accepted: 08.05.2025

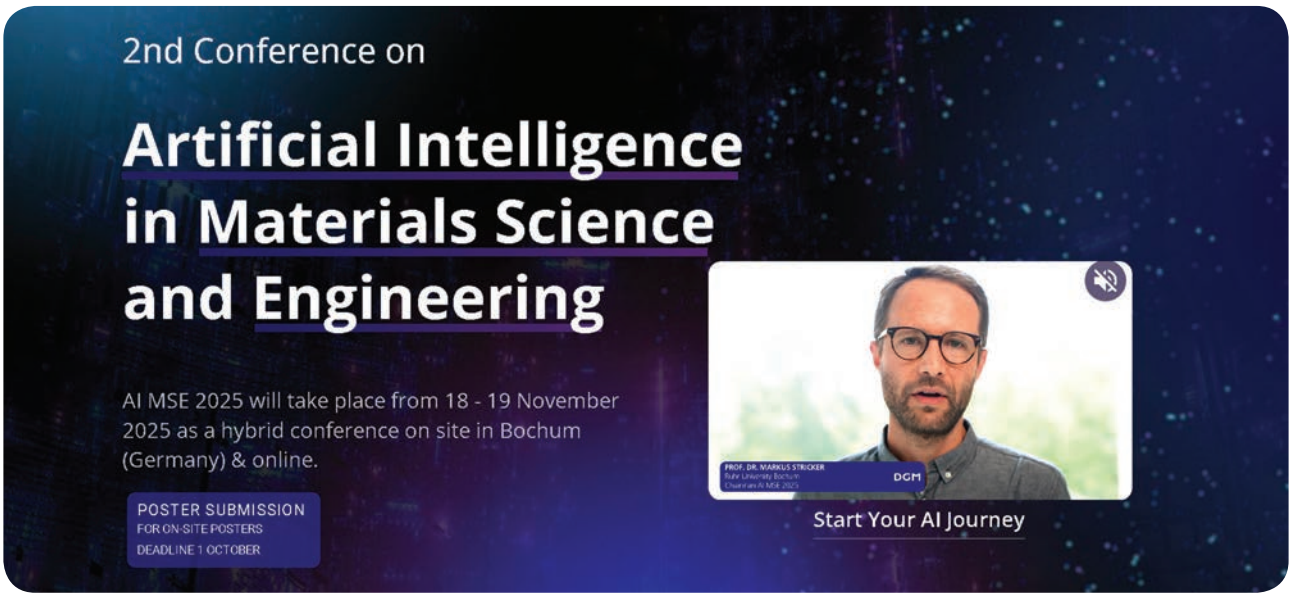

DOI: https://doi.org/10.37434/tpwj2025.04.03

APPLICATION OF MICROPLASMA DEPOSITION FOR 3D PRINTING OF AEROSPACE ENGINE PARTS

V.Yu. Khaskin[1], **K.M. Sukhyi**[2], **O.V. Ovchynnykov**[1], **O.V. Zaichuk**[2]

[1]E.O. Paton Electric Welding Institute of the NASU
11 Kazymyr Malevych Str., 03150, Kyiv, Ukraine
[2]Ukrainian State University of Science and Technologies
2 Lazaryana Str., 49010, Dnipro, Ukraine

ABSTRACT

The work is devoted to establishing the basic technological regularities and features of the formation of characteristic structures of metal layers during additive microplasma deposition with powders of corrosion- and heat-resistant alloys and determining the prospects of this process for 3D printing of aircraft parts. The work established that the choice of the mode of additive microplasma deposition of the selected group of powders is mainly determined by the size of the filler powder fraction. The energy input and thermal power of the constricted arc for growing metal products with a wall thickness of up to 3 mm using powders based on Fe and Ni with a fraction of 40–100 μm were determined. The main features of the structure formation of the metal of samples produced by microplasma deposition, and their mechanical characteristics were determined, and the tendency to burnout of alloying elements of the deposited alloy was assessed. It is shown that despite the need for finishing mechanical treatment of critical functional surfaces, the use of microplasma deposition can be considered a fairly promising direction for 3D printing of metal parts of aircraft equipment.

KEYWORDS: 3D printing, nickel alloy, microplasma deposition, metal powders, technological modes, dendritic structure, heat dissipation, mechanical properties

INTRODUCTION. ANALYSIS OF PUBLISHED DATA AND PROBLEM DEFINITION

Application of 3D printing with metallic powder materials is a promising direction in modern aerospace industry. When designing rapidly adaptable technologies of manufacturing unmanned aerial vehicles (UAV) there is the need for development of fuel-efficient and flexible technological solutions. Such products can be produced quite simply and quickly from polymer and metallic materials [1]. 3D printing technologies are the most suitable for development of such parts [2]. These technologies can be used to manufacture both the body elements and engine components [3].

To shorten the aircraft downtime during its repair, it is often necessary to apply multilevel production systems, which manufacture complex expensive components, and considerable investments into storage facilities are required, so as to ensure timely delivery of the manufactured parts [4]. Instead, the use of additive technologies allows carrying out on-site production of complex parts in good time, based on digital data without complex tools or mechanisms. Such an approach is particularly relevant for additive deposition (or 3D printing) of metal powders with manufacturing of finished metal products [5].

At present during maintenance and repair of aerospace vehicles various additive technologies are used for 3D printing of finished metal parts, in particular, supersonic particle deposition (SPD) and laser additive deposition (LAD) [6]. Such technologies are used to lower the cost of repair and maintenance, and increase the operational readiness of the vehicles. However, these technologies in themselves are rather costly in industrial application, and they also have comparatively low productivity [7]. Note that one of the main advantages of such additive technologies is the high precision of manufacturing these products. Such precision, however, is not always necessary, and in a number of cases it can be achieved by simultaneous application of additive deposition and machining [8].

One of the ways of further lowering the cost of metal 3D products with a simultaneous increase of their manufacturing productivity is application of arc methods of additive deposition of metals. In this sense, microplasma powder deposition is both interesting and promising [9]. Additive microplasma 3D printing with metal powders is an innovative technology based on welding, which allows creating parts of a relatively small size with a low cost and high productivity [10]. Such a technology enables, in particular, development of parts with functionally graded components [11] or low specific weight [12]. However, at present the 3D printing by additive microplasma powder deposition has not become widespread, because of insufficient scope of data on the rational modes of the process, which requires conducting technological research.

RESEARCH OBJECTIVE AND TASKS

The objective of the work to establish basic technological regularities and features of formation of the characteristic structures of metal layers in additive

Copyright © The Author(s)

microplasma deposition with powders of corrosion- and heat resistant alloys, based on iron and nickel, determination of the prospects of this process for 3D printing of parts of aerospace engines.

To achieve this objective, the following tasks were solved:

1. Establishing the basic technological regularities of additive microplasma deposition of powders of corrosion- and heat-resistant alloys during manufacture of 3D products.

2. Determination of the features of formation of the characteristic structures of metal layers in additive microplasma deposition of the selected alloy powders.

3. Determination of basic mechanical characteristics of the deposited metal by conducting mechanical testing of samples produced by additive microplasma deposition.

MATERIALS, EQUIPMENT AND INVESTIGATION METHODS

To achieve the objective of this study and solve the posed tasks, the following procedure was accepted:

- selection and preparation of powder filler materials for additive microplasma deposition;
- selection of the parameters of the technological mode of microplasma deposition;
- modeling the plasmatron design and flow speeds/rates of plasma-forming and shielding gases, in order to achieve a stable laminar mode of constricted plasma generation;
- creation of a laboratory stand to carry out the technological research;
- conducting experiments on deposition of spatial geometrical primitives by microplasma method with application of the selected powder filler materials;
- performance of metallographic examination of the deposited samples, determination of the characteristic defects and ways to remove them, establishing the regularities of formation of the characteristic structures of the deposited layers and prospects for application of this process for 3D printing of aircraft parts.

When producing the 3D metal objects, layer-by-layer deposition was performed on substrates from Q235 steel of 100×100×10 mm size. The compositions of the materials of the substrate and surfacing powders are given in Table 1. Corrosion-resistant powders HYF 103, 316L and PG SR2 were used to conduct preliminary research and to optimize the deposition modes, which allowed reducing the scope of experimental work with heat-resistant powders KhN50VMTYuB (EP648) and KhN60VT (VZh98). Chemical composition of powders from KhN50VMTYuB (EP648) alloy corresponded to the requirements of special technical conditions and industry standard (OST1 90126–85 and TU14-1-3046–97), powder from KhN60VT alloy (VZh98) — to TU 14-1-4296–87.

A specialized microplasma torch was developed for deposition, which will be discussed below. A disperser-feeder of an original design with a regulated range of powder flow rates G = 1.0–4.0 g/min was used for feeding the powders.

There are a number of requirements to powders used for 3D printing of parts with application of additive technologies. Among them, the following are mandatory: spherical form of the powder and size, which should not exceed 100 μm. These are exactly the powders that are the most technologically advanced, and have high bulk density, which was determined in keeping with DSTU 2640. High bulk density was indicative of compact ar-

Table 1. Chemical composition of filler powders and substrate for deposition

Material	Elemental composition, wt.%										
	Fe	B	C	Si	Mn	Ni	Cr	Cu	P	S	Others
Substrate metal											
Q235 steel	Base	–	0.14–0.22	0.05–0.15	0.4-0.65	<0.3	<0.3	<0.3	<0.04	<0.05	–
Filler (surfacing) materials											
HYF-103 powder (40–60 μm granulation)	Base	1.15	–	0.75	0.6	7.85	15.55	–	<0.02	<0.01	Mo <3.0
Powder of 316L stainless steel (40–60 μm granulation)		–	0.03	<0.6	<0.8	14–16	15–17	–	<0.02	<0.015	Mo 2.5–3.0
Powder of Ni–Cr–B–Si system (60–100 μm granulation)	<5.0	2.0–2.8	0.4–0.7	2.5–3.5	–	Base	13.5–16.5	–	<0.04	<0.04	Al <0.8
Powder KhN50VMTYuB (EP648) 40–100 μm	<4.0	0.008	<0.03	<0.04	<0.5		32–35	–	<0.010	<0.015	Nb – 0.5–1.1; Ti – 0.5–1.1; Al – 0.5–1.1; Mo – 2.3–3.3; W – 4.3–5.3
Powder KhN60VT (VZh98) 60–100 μm	<4.0	–	<0.1	<0.8	<0.5		23.5–26.5	–	<0.013	<0.013	Ti – 0.3–0.7; W – 13–16

Table 2. Results of determination of bulk density of powders from heat-resistant alloys

Data on powder	Bulk density, g/cm³	
Alloy	KhN60VT	KhN50VMTYuB
60–100	3.41	3.52
≤63	4.25	4.72

rangement of the powder particles, which is important to form products on their base. Table 2 gives the results of determination of bulk density for powders from KhN60VT (VZh98) and KhN50VMTYuB alloys (EP648). The size and fractional distribution of the studied powders were determined by sieve analysis.

Powders of a regular spherical shape were used for microplasma deposition. The size of powder particles, determined on an unetched transverse microsection, was in the range of 48–101 μm. An example of metallographic study of powder from heat-resistant nickel alloy is given in Figure 1.

To perform the deposition, preliminary preparation of filler materials was conducted, which consisted of selection of powders of a certain fractional composition, by their sieving through a set of the appropriate calibration sieves. Before calibration, the powders were preheated in a muffle furnace at the temperature of 150–200 °C to remove residual moisture, the presence of which is associated with their hygroscopicity.

Used as the microplasma power source was Tetrix 421 AC/DC (EWM GmbH Company, Germany) fitted with a plasma module with the range of current regulation of 5–50 A. Welding plasmatron of the microplasma welding unit MPU-4 (Ukraine) was selected as the base for creation of a laboratory experimen-

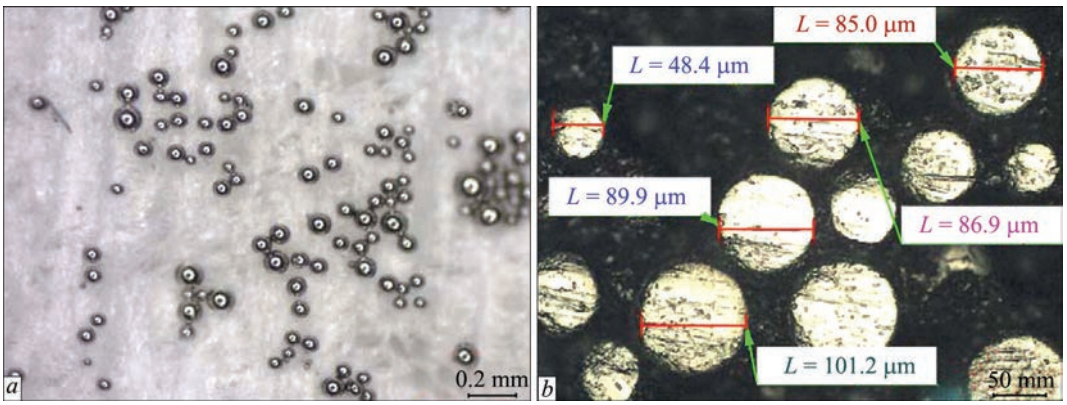

Figure 1. Powder from heat-resistant nickel alloy KhN50VMTYuB: *a* — appearance (binocular), ×40; *b* — unetched transverse section (powder embedded in Bakelite), ×200

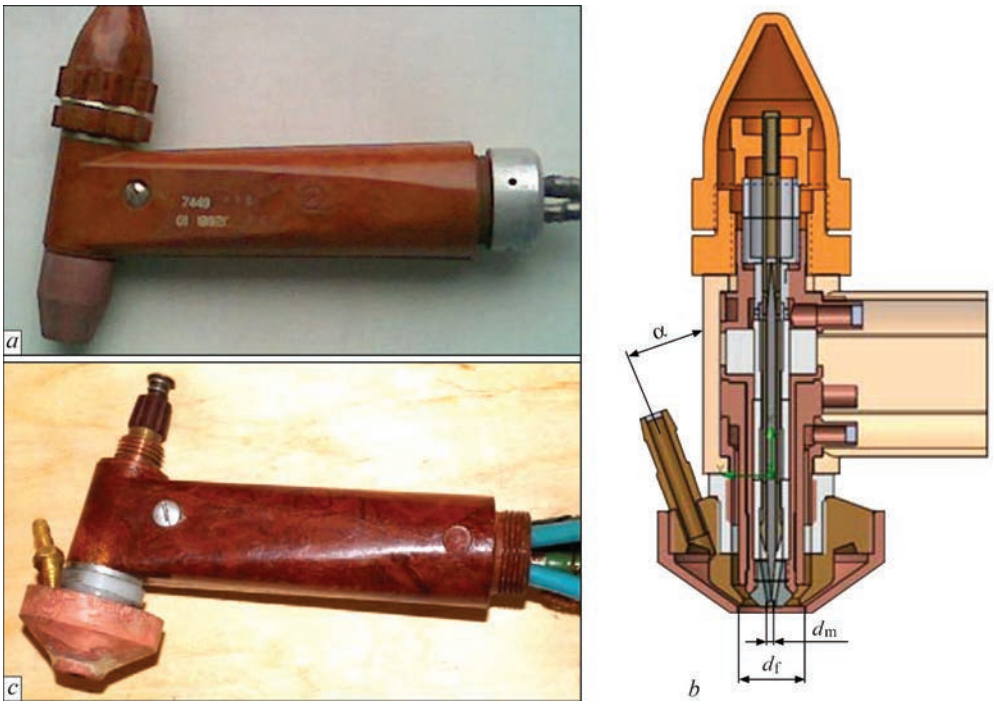

Figure 2. General view of MPU-4 plasmatron for microplasma welding (*a*), scheme of the upgraded structure (*b*) and its appearance after upgrading (*c*) with nozzle assembly for powder injection into the plasma jet (through a nipple located at an angle α ≤ 45° to plasmatron axis)

tal torch for additive deposition, which was subjected to the necessary upgrading (Figure 2). A specialized nozzle assembly was designed for powder feeding. The assembly has a system of nozzles, which allowed, in addition to protection of the deposition zone, also controlling the transporting gas with the powder relative to the plasma column coordinate. Cooling of plasmatron assemblies was also improved for its reliable operation in the range of currents of 5–100 A. The plasmatron was moved relative to the sample being surfaced, using an anthropomorphous robot-manipulator of ARC Mate 50D type (FANUC, Europe).

Computational software SolidWorks Flow Simulation was applied during design of the specialized nozzle assembly [13]. This software was used to model and optimize by the flow laminarization criterion the dynamics of plasmatron gas flows and design of the specialized nozzle assembly for powder feeding to perform additive microplasma deposition.

Table 3. Technological parameters of microplasma deposition process, used in modeling the operation of MPU-4 plasmatron with nozzle assembly for powder deposition

Number	Parameter description	Value
1	Speed of plasma-forming Ar gas flow (Q_{pl}), l/min	1.0–1.5
2	Speed of shielding Ar gas flow (Q_{sh}), l/min	10
3	Speed of transporting Ar gas flow (Q_{pl}), l/min	12
4	Powder flow rate Q_p, g/min	2.4
5	Speed of cooling liquid flow (for each circuit) Q_p, l/min	1.5
6	Thermal power released by constricted arc, W	840
7	Powder particle size, μm	100

Table 3 gives the technological parameters of the microplasma deposition process, used in modeling the operation of MPU-4 plasmatron with the nozzle

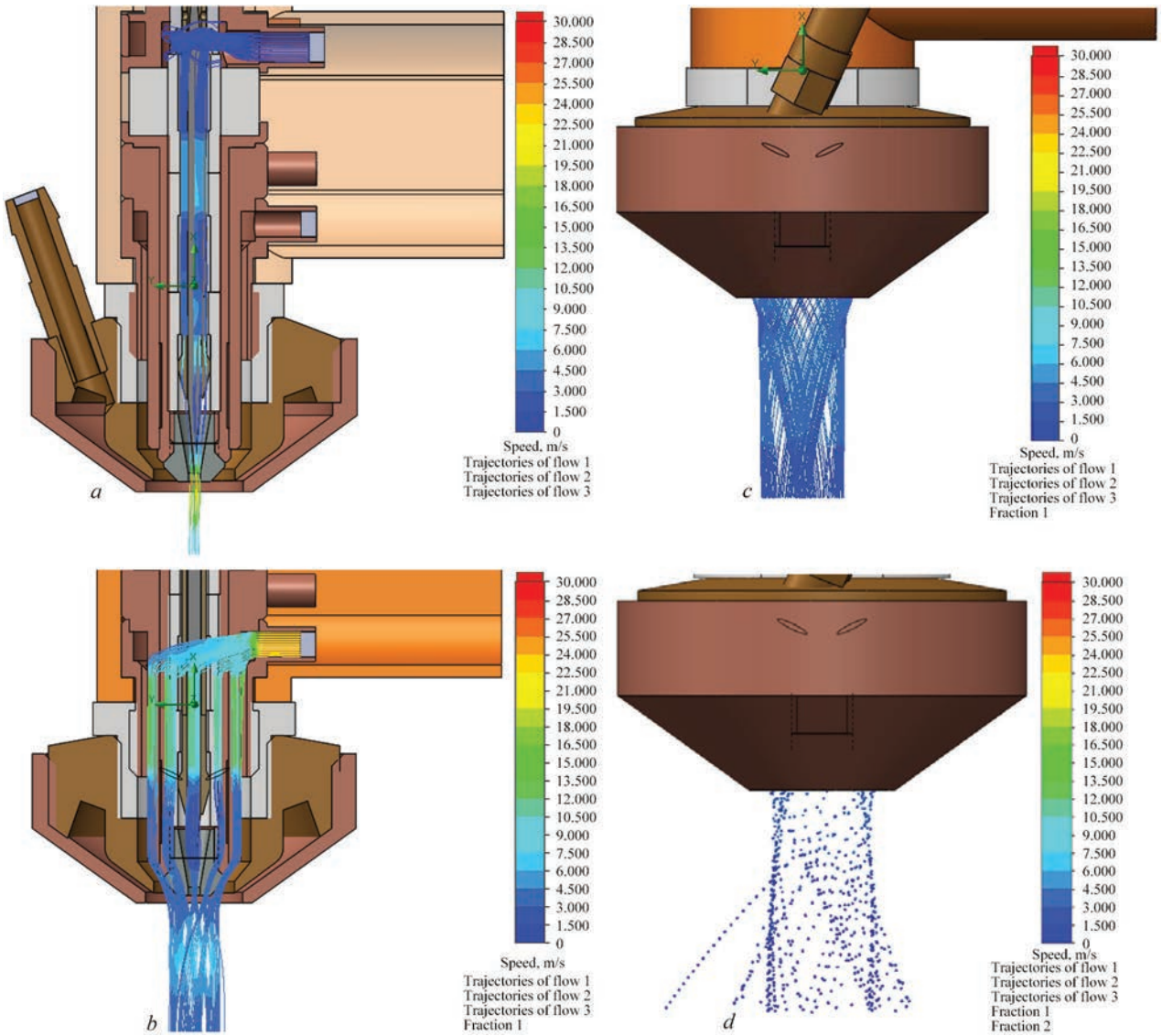

Figure 3. Speed and direction of gas flows in upgraded MPU-4 plasmatron: *a* — plasma-forming; *b* — shielding; *c* — transporting; *d* — powder particle flow

assembly for powder deposition. Modeling the gas dynamics allowed creation of an upgraded plasmatron design with satisfactory results for the flows of plasma-forming, shielding and powder transporting gases. Figure 3 shows the lines of plasma-forming, shielding and transporting gas flows and the flow of deposited powder particles. The design of the specialized nozzle assembly allowed achieving laminarity of the flows in the zones of the respective channels and at the plasmatron outlet.

Transverse templates were cut out of the samples produced by additive deposition and microsections were prepared to conduct metallographic analysis. After their grinding and polishing, electrolytic etching in chromic acid or ammonium sulphate was applied to reveal the microstructures [14]. Obtained structures of the samples were studied by the methods of optical (Neophot-30 microscope from Carl Zeiss, Germany) and analytical scanning electron microscopy (JSM-840 microscope from PHILIPS, Holland). Analytical scanning electron microscopy was applied to determine the chemical composition of the phases and metal grains (general and local point analysis). Optical microscopy was used to study the structural changes. Microhardness was measured with microhardness meter LM-400 (LECO series, USA) at 50 g load. Mechanical static tensile testing was conducted in an all-purpose tensile servohydraulic system MTS 810 (Material Test System, USA), using standard samples (GOST 6996–66) which were cut out of 3D printed walls across the deposited beads.

RESULTS OF TECHNOLOGICAL RESEARCH

Technological research was performed in keeping with the scheme given in Figure 4 [15]. The minimal wall thickness of the grown product in the conducted research on microplasma deposition was up to 3 mm. Investigations showed that during production of volumetric items by additive layer building-up by successive deposition, a very important parameter is the size of the built-up layer (deposited metal bead), as it determines the characteristics of the shape and the surface, as well as the precision of product formation. Therefore, a priority task, which was solved during selection of the deposition mode parameters, was determination of the best relationship between the flow of filler powder particles (Figure 3, *d*) and microplasma arc diameter. The difference in the conditions of deposition on the substrate and on the previously deposited bead was taken into account. In the latter case, when current is increased, the bead volume is reduced due to deterioration of the heat dissipation, penetration of the previous bead and increase of the pool length.

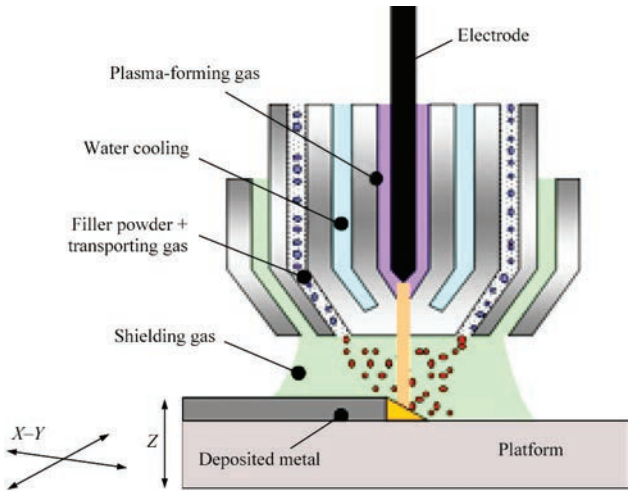

Figure 4. Scheme of conducting the technological research [15]

Another task, solved in order to select the mode, was increase in the fraction of useful filler powder consumption (UPC coefficient) during additive growing of the part. Experiments showed that the main cause for the powder filler losses is the movement of its dispersed particles on the periphery of the plasma arc column and further on their elastic reflection from the surface of the product being deposited, beyond the zone of the formed pool of deposited metal.

Thus, in case of realization of additive technology of growing thin-walled metal products with up to 3 mm wall thickness, it is important to be able to control such process characteristics, as concentration of the microplasma arc and addition of powder filler. In particular, in order to optimize the trajectories of filler material movement in the plasma arc, it is recommended to add filler powders to the arc at up to 40–45° to the plasmatron axis (Figure 2, *b*).

Research was performed with application of a microplasmatron with lateral distributed injection of the filler powder and diameters of plasma-forming nozzle channels d_{pl} = 1.8 and 2.5 mm and of focusing nozzle d_f = 2.5 mm and 4.5 mm (Figure 2, *b*). With these dimensions, its stable operation at welding current in the range of 5–50 A is ensured. The concentration of filler powder injection with flow rate G = 1.0 = 3.5 g/min through the microplasma arc to the anode plane (substrate, on which the first layer was deposited) was assessed by determination of the weight of powder, which penetrated into the weld pool, during successive increase of its dimensions. Width B of the molten metal pool (or deposited bead) changed with increase of welding current at a constant speed of microplasma arc movement in the range of 2–5 and 4–10 mm (Figure 5, Table 3). During the experiment, with gradual increase of the weld pool width by 5 times, dependencies of the change in the deposited bead specific mass M_d and UPC coefficient were derived which characterize the radial distribution of the filler powder.

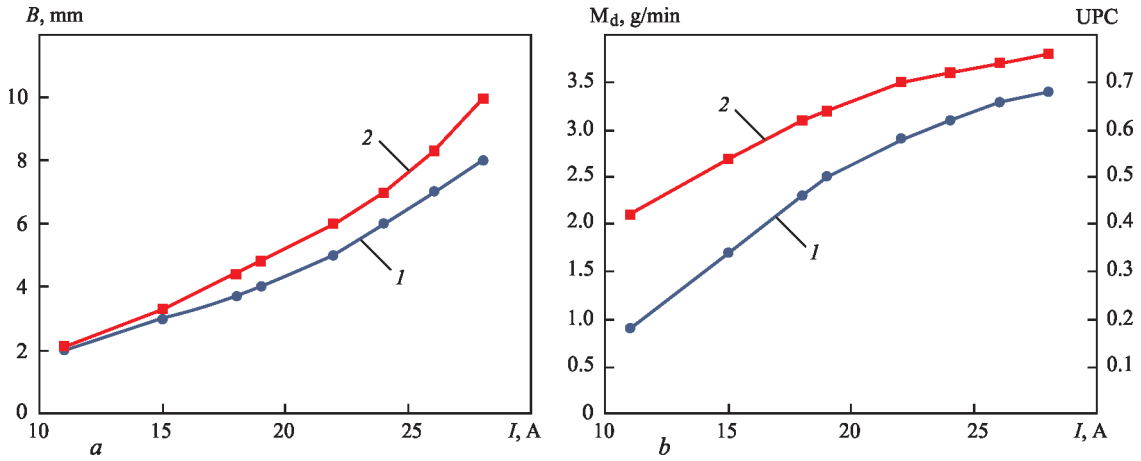

Figure 5. Dependence of bead width B (*a*), specific weight of deposited metal (HYF 103 alloy powder) M_d and UPC (*b*) on welding current I at deposition rate V = 3.24 mm/s: *1* — microplasmatron with d_{pl} = 2.5 mm, d_f = 4.5 mm, G = 3.2 g/min, B = 2–5 mm; *2* — d_{pl} = 1.8 mm, d_f = 2.5 mm, B = 4–10 mm

In keeping with the data in Figure 5, in order to produce volumetric products with up to 3 mm wall thickness (or with deposited bead width $B \leq 3$ mm), it is necessary to perform microplasma deposition at up to 15 A arc current. However, application of up to 30 A current is undesirable, because of the low process stability. To increase the stability, it is rational to increase the plasmatron arc current to 30–35 A, which requires increasing the deposition rate from 10–15 to 30 m/h to preserve the 3 mm wall thickness.

Further technological research was conducted with filler powder flow rate G = 3.0 g/min. The modes of additive microplasma deposition of the used powders were refined by the criteria of optimization of the deposited bead shape and formation of reliable fusion with the substrate and/or previous bead. The following main parameters of the deposition mode were selected: arc current I = 35 A, arc voltage U = 40 V, deposition rate V = 35 m/h (9.66 mm/s), energy input of deposition E = 87 J/mm (allowing for process efficiency of 0.6 [16]). Other parameters of the deposition mode are given in Table 3. Conducted research showed that in additive microplasma deposition with the selected powders (Table 1) the thickness of the deposited wall is preserved in the range of 3.0±0.3 mm with satisfactory stability (Figure 6). Here, the UPC coefficient is in the range of 0.84–0.88 (powder losses are equal to 16–12 %, respectively), which is an acceptable value.

RESULTS OF METALLOGRAPHIC STUDIES

In additive microplasma deposition complete melting of the powder occurred in all the cases of application of filler materials listed in Table 1. The deposited metal structure was characterized by a clearly expressed layering; deposited layer thickness was equal to 550–650 μm. Surfacing was performed in several passes, with successive deposition of the metal layers — one per pass. The structure of the fusion zones between the layers was homogeneous. The macrostructure of each deposited layer was homogeneous without formation of any defects, cracking or incomplete melting.

In case of application of powder of Ni–Cr–B–Si system for single-pass deposition, an equiaxed finely dispersed structure was produced in the deposited bead metal. The deposited material microstructure consisted of a two-phase matrix (Figure 7), in which a component prevailed, which appeared light when etching with hardness HV 4640–5720 MPa. Light-gray precipitates of higher hardness of HV 6030–7010 MPa are present alongside it (Figure 8). Thus, as a result of microplasma growing of the product, the microstructure of the heat-resistant nickel alloys consisted of a matrix of γ-solid solution (light-coloured), with intermetallic phases of the type of γ′-phase (Ni, Cr), (Al, Ti, Nb) and Ni(Cr, Mo, W) + carbides observed against its background. To increase the dispersion-hardening effect, these alloys, in the classical sense, should be heat treated. However, selection of the required temperatures and duration of holding during heat treatment of the innovative material produced by 3D layer-by-layer plasma deposition has not been performed so far. This can be the subject of further studies. No signs of overheating or burnout with a

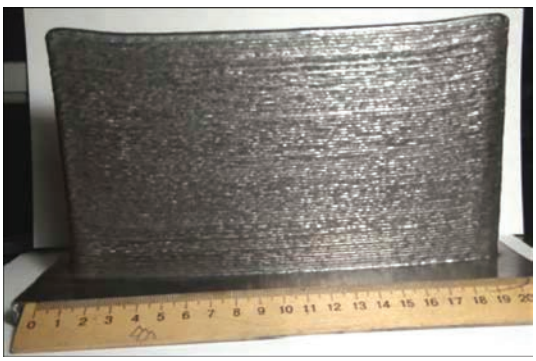

Figure 6. Appearance of a plate of metal produced by layer-by-layer microplasma deposition of HYF-103 powder

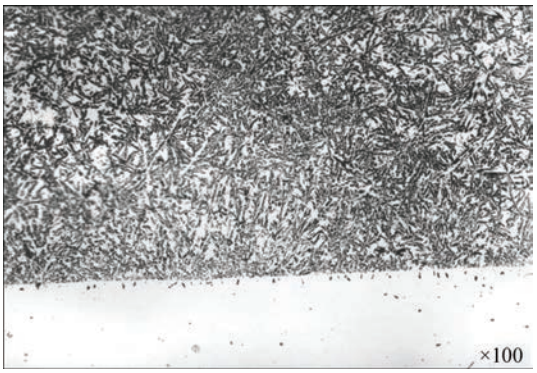

Figure 7. Structure of microplasma deposit, ×100

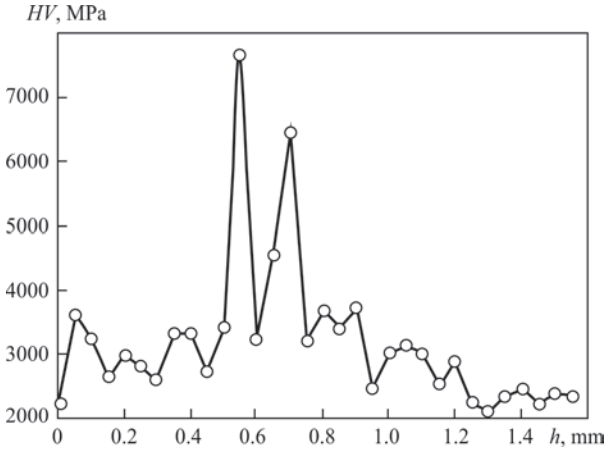

Figure 8. Distribution of microhardness $HV_{0.05}$, MPa with depth h, mm

jump-like increase in the grain size and intergranular melting were found in the microstructure of the grown samples.

Judging from the presence of peaks in the results of microhardness measurements and data of microstructural investigation, we can conclude that harder carbides of different shapes are included in the solid solution of the matrix. Strengthening phases had the shape of plates of different thicknesses, and their horseshoe-shaped and diamond-shaped precipitations were also found. The carbides were characterized by high hardness (HV > 20000 MPa). In addition to coarse (primary) carbides, their finer precipitates were also observed in the grown material matrix that, probably, promoted an increase in the strength and hardness of the material. Eutectic carbide precipitates of hardness on the level of HV 2340–3030 MPa are also observed over the entire deposit.

A thin light-coloured strip of hardness HV 2540–2860 MPa is also observed along the line of fusion with the base metal. This structural component is homogeneous along the entire length of the deposit, and its thickness is 10–12 μm. Note that the deposit structure is refined in the direction from the upper edge to the base metal of the substrate. Microanalysis of individual areas of the structure showed that the deposited metal composition is close to that of the deposited powder (see Table 1).

In case of application of HYF-103 powder for three-pass additive deposition, according to the data of electron microscopy, a fine dendritic structure of the deposited metal was produced, which contains both relatively large grains and fine ones. The large and fine dendrites form colonies, disoriented relative to each other (Figure 9). Crystals of different sizes were formed in the upper and lower parts of the sample, which resulted from the non-equilibrium conditions of solidification at microplasma 3D growing of the sample. So, in the lower part of the deposited metal the heat was removed through the base substrate, while in the sample upper part it was removed predominantly through thermal radiation and heat dissipation into the lower deposited layers. This resulted in slower cooling of the metal in the sample upper part and, thus, led to grain growth.

In the longitudinal direction the dendrites formed extended crystallite branches, oriented predominantly in the direction of heat removal and united into colonies. Microstructural analysis of the sample cut out in the lower part, showed that crystallite growth proceeds in one direction (Figure 9, *c*). The dendrites consist of grain blocks with similar crystal orientation, the boundaries of which were revealed as a result of etching. A comparison of the structure of metal in the samples, cut out in the longitudinal direction in the sample upper and lower parts, points to different nature of crystallization, during upward formation of the sample (Figure 9). Microanalysis in different individual sections of the structure showed that the depos-

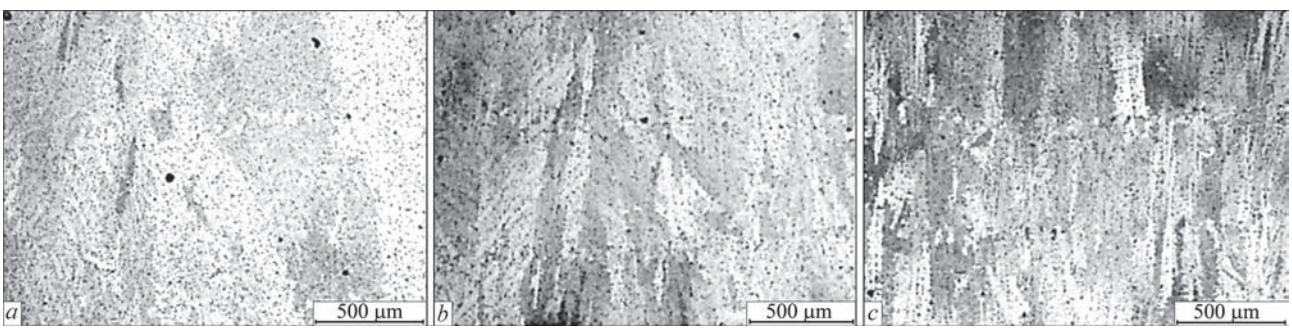

Figure 9. Microstructure of metal, produced by three-layer additive microplasma deposition of HYF-103 powder (×100): *a* — top of deposited sample; *b* — middle of deposited sample; *c* — bottom of deposited sample

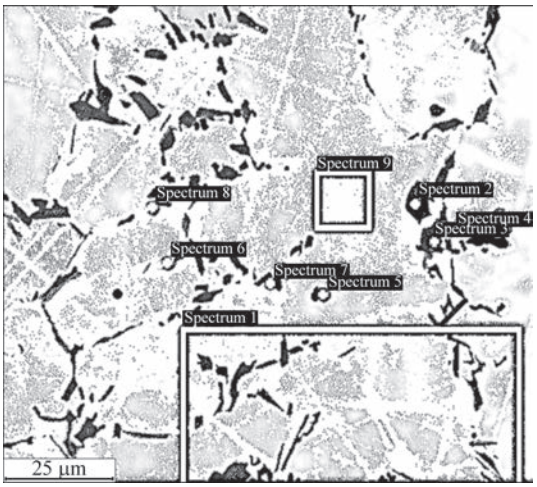

Figure 10. Microstructure of metal produced by additive microplasma deposition of HYF-103 powder, with indication of areas of element content microanalysis

ited metal composition is close to that of the deposited powder (Figure 10, Tables 1 and 4).

During examination in a reflected light optical microscope, the microstructure of samples of KhN50VMTYuB and KhN60VT alloys in the dendrite body appeared to be less homogeneous (Figure 11, *a*). Studying their structure in an electron microscope revealed that the dendrites of γ-solid solution have an internal structure with thin and intermittent boundaries of the block walls (Figure 11, *b*).

As one can see from the above microstructure, dispersion hardening during rapid cooling of the layers of microplasma deposited metal either did not occur, or occurred only to a minor extent.

DISCUSSION OF INVESTIGATION RESULTS

Conducted technological research showed that for the selected group of powders (see Table 1) the parameters of the mode of additive microplasma deposition predominantly depend on the fractional composition of the filler powder. Complete melting of the powder occurs under the conditions of application of microplasma deposition with the energy input of 85–90 J/mm and thermal power of ~800–900 W released by the constricted arc at additive growing of metal products. The metal structure is characterized by a clearly expressed layering; thickness of the deposited layer is equal to 500–650 μm.

Based on the results of the conducted technological research, it was determined that successive deposition of metal is manifested in formation of a relief on the sample side surface (Figure 6). Metal rolls are observed, which are an alternation of protrusions and depressions, caused, probably, by partial flowing of liquid metal down the side surface. Dimensions of these rolls approximately correspond to the height of the metal layer deposited in one pass. One of the ways to minimize this parameter is stabilization of additive microplasma deposition due to selection of its rational

Table 4. Element content in individual areas of the structure according to Figure 10

Spectrum	Chemical composition, wt.%												
	B	N	O	Mg	Si	V	Cr	Mn	Fe	Co	Ni	Mo	Total
1	–	–	–	–	0.95	–	16	0.31	72.16	0.32	9.1	1.17	100
2	–	–	–	–		–	49.26	–	47.38	–	1.12	2.24	100
3	–	–	–	–		0.24	48.64	–	48.09	0.4	0.91	1.72	100
4	–	–	17.41	9.17	8.85	–	9.37	–	48.21	0.41	6.06	0.52	100
5	20.25	19.63	–	–	0.26	–	7.85	0.32	45.51	0.28	5.09	0.81	100
6	–	–	–	–	0.65	0.41	15.52	–	56.74	0.4	6.47	19.8	100
7	–	–	–	–	0.67	0.26	17.15	–	59.99	0.44	6.64	14.85	100
8	–	–	–	–	0.72	0.25	14.86	–	61.16	0.31	7.41	15.28	100
9	–	–	–	–	0.95	–	13.68	–	74.64	0.36	9.79	0.58	100

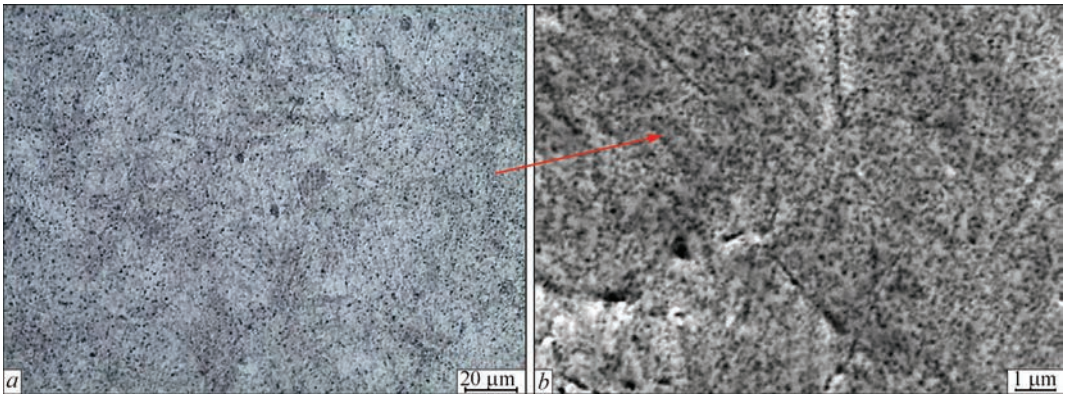

Figure 11. Microstructure of a sample, grown by microplasma deposition of KhN50VMTYuB alloy: *a* — ×500 (optical metallography); *b* — ×10 000 (electron microscopy)

Table 5. Mechanical properties of metal produced by additive microplasma deposition of HYF-103 powder

Sample number	F_0	L_0	L_k	σ_t, MPa	σ_y, MPa	δ, %
1	7.15	20.02	20.49	606	474	3.165
2	7.16	19.78	20.78	627	510	5.056
3	7.15	22.14	22.94	618	462	3.613
Averaged value	–	–	–	617	482	3.95

process modes. Another method to minimize this parameter is reduction of the height of the layer deposited in one pass. Such an approach, however, lowers the productivity of 3D printing of the product and requires individual optimization measures.

In multilayer microplasma deposition no such defects, as separation of the adjacent layers inside the deposit, because of incomplete fusion between the layers; molten material solidification in the form of spheres, and not a continuous layer; deformation through the difference in the coefficients of thermal expansion of the layers, were found. Fusion zones between the layers are not identified structurally, and a homogeneous structure is observed. The macrostructure of each surface-melted layer is quite homogeneous without formation of any defects, or cracking. The methods of optical and electron microscopy established that the sample metal structure is dendritic and contains both coarser and finer grains. Large and fine grains form colonies, disoriented relative to each other (for instance, Figure 8). Crystallite formation at successive deposition of the metal layers in the sample upper and lower parts is different, and it is determined by differences in the crystallization process. So, in the lower part of the deposited metal heat removal is more intensive, as it occurs through the base substrate, which has rather good heat conductivity. In the sample upper part heat removal is less intensive, as it is performed predominantly due to thermal radiation, while heat conductivity of the predeposited layer is due to the applied filler alloy, and it is predominantly low. This results in slower cooling of the metal in the sample upper part and, thus, leads to a certain grain growth.

Electron microscopy studies of phase composition of HYF-103 alloy layers, deposited by microplasma method in the selected rational mode showed trends of slight burnout of individual alloying components (Tables 1 and 4). So, manganese content decreased from 0.6 to ~0.3 wt.%. Boron burnout was also observed in individual sections. On the whole, however, reduction of the content of alloying components of the studied deposited alloys, is rather limited, and cannot be considered significant.

Ultimate strength σ_t, conditional yield limit $\sigma_{0.2}$ and relative elongation δ of the deposited metal at uniaxial tension were measured on samples 30 mm long, which were cut out along the vertical of a plate produced by layer-by-layer building up (see Figure 6). The deposited metal strength was assessed by the results of uniaxial tensile testing of three samples.

Conducted studies of mechanical properties (Table 5) allow us to conclude that the metal deposited by additive technology ensures rather high strength, reaching more than 600 MPa, where F_0 is the cross-sectional area of the sample; L_0 and L_k are the initial and final lengths of the sample; δ is the relative elongation.

Over the recent years the process of 3D printing of aircraft parts has become ever more relevant. Application of 3D printers significantly lowers the cost of the created products, increases the production flexibility and accelerates manufacture of the required repair kits of the parts. One of the most complicated tasks in this respect is 3D printing of metal parts, both finished and with additional machining. Application of additive microplasma deposition with metal powders for manufacture of 3D products for aviation equipment will allow a significant productivity improvement, compared to the currently available methods. So, application of microplasma deposition will allow reaching the productivity of ~3–4 kg/h, whereas laser deposition can provide the productivity of up to 1.5 kg/h. Moreover, microplasma deposition allows creating composite or functionally gradient metal layers, which will promote material saving, and will enable creating wear-resistant friction surfaces relative to a soft base during 3D printing. Equipment applied for microplasma deposition is much less expensive and easier to maintain, compared to laser equipment. On the whole, despite the need for final machining of critical functional surfaces, application of microplasma deposition can be regarded a promising direction of 3D printing of metal parts for aviation equipment. It is rational to focus further research on studying the influence of heat treatment on the structure and properties of products grown by innovative 3D microplasma deposition from heat-resistant nickel alloys, considered in the work.

CONCLUSIONS

1. It was determined that selection of the mode of additive microplasma deposition of the chosen group of iron- and nickel-based powders is predominantly due to filler powder granulation. At additive microplasma growing of metal products with up to 3 mm wall thickness with application of Fe- and Ni-based powders with fraction size of 40–100 μm complete melting of the powder occurs in the modes, ensuring the energy input of 85–90 J/mm with thermal power of ~800–900 W released by the constricted arc.

2. It was established that the metal structure in samples produced by microplasma deposition, consists of dendrite colonies disoriented one relative to another, which contain both relatively large and finer grains. In the deposited metal lower layer small-

er-sized crystallites are formed, due to more intensive heat removal through the steel substrate of the base. In the upper layers of the deposited metal larger-sized crystallites are formed, owing to reduction in the heat removal intensity, which is promoted by application of filler alloys with rather low heat conductivity.

3. Mechanical testing for static tension of samples cut out of the deposited metal across the deposited beads showed that the strength of HYF-103 alloy exceeded 600 MPa at yield limit values higher than 480 MPa and relative elongation close to 4 %. Such results are attributable to absence of deposition defects and small fraction of burning out of the deposited metal alloying elements.

4. Conducted research showed the fundamental possibility of formation of dispersed dendritic structures with grains of different spatial orientation, structural homogeneity of the deposited layers without clearly expressed fusion zones, and absence of pores or cracking. Such trends of structure formation are indicative of the good prospects for further application of additive microplasma deposition for 3D printing of parts from iron- and nickel-based corrosion- and heat-resistant alloys, in particular, parts of aerospace engines.

REFERENCES

1. Moon, S.K., Tan, Y.E., Hwang, J., Yoon, Y.-J. (2014) Application of 3D printing technology for designing light-weight unmanned aerial vehicle wing structures. *Inter. J. of Precision Eng. and Manufacturing-Green Technology*, **1**, 223–228. DOI: https://doi.org/10.1007/s40684-014-0028-x
2. Chee, K.C., Kah, F.L., Chu, S.L. (2010) *Rapid prototyping: Principles and applications.* 3rd Ed. World Scientific Publ. Co Pte Ltd. DOI: https://doi.org/10.1142/6665
3. Martinez, D.W., Espino, M.T., Cascolan, H.M. et al. (2022) A comprehensive review on the application of 3D printing in the aerospace industry. *Key Eng. Materials*, **913**, 27–34. DOI: https://doi.org/10.4028/p-94a9zb
4. Singamneni, S., Lv, Y., Hewitt, A. et al. (2019) Additive manufacturing for the aircraft industry: A review. *J. of Aeronautics & Aerospace Eng.*, 8(**1**), 214. DOI: https://doi.org/10.35248/2168-9792.19.8.215
5. Gadagi, B., Lekurwale, R. (2021) A review on advances in 3D metal printing. *Materials Today: Proceedings*, 45(**1**), 277–283. DOI: https://doi.org/10.1016/j.matpr.2020.10.436
6. Matthews, N. (2018) Chapter fifteen — Additive metal technologies for aerospace sustainment. *Aircraft Sustainment and Repair*, **2018**, 845–862. DOI: https://doi.org/10.1016/B978-0-08-100540-8.00015-7
7. Gisario, A., Kazarian, M., Martina, F., Mehrpouya, M. (2019) Metal additive manufacturing in the commercial aviation industry: A review. *J. of Manufacturing Systems*, **53**, 124–149. DOI: https://doi.org/10.1016/j.jmsy.2019.08.005
8. Yamazaki, T. (2016) Development of a hybrid multi-tasking machine tool: Integration of additive manufacturing technology with CNC machining. *Procedia CIRP*, **42**, 81–86. DOI: https://doi.org/10.1016/j.procir.2016.02.193
9. Peleshenko, S., Korzhyk, V., Voitenko, O. et al. (2017) Analysis of the current state of additive welding technologies for manufacturing volume metallic products (Review). *Eastern-European J. of Enterprise Technologies*, 3–1(**87**), 42–52. DOI: https://doi.org/10.15587/1729-4061.2017.99666
10. Kumar, P., Jain, N.K. (2020) Effect of material form on deposition characteristics in micro-plasma transferred arc additive manufacturing process. *CIRP J. of Manufacturing Sci. and Technol.*, **30**, 195–205. DOI: https://doi.org/10.1016/j.cirpj.2020.05.008
11. Wang, H., Jiang, W.H., Valant, M., Kovacevic, R. (2003) Microplasma powder deposition as a new solid freeform fabrication process. *Proc. of the Institution of Mechanical Eng., Pt B: J. of Eng. Manufacture*, 217(**12**), 1641–1650. DOI: https://doi.org/10.1243/095440503772680578
12. Ovchinnikov, O.V., Duryagina, Z.A., Romanova, T.E. et al. (2021) *Powder titanium alloys for additive technologies: Structure, properties, modeling.* Kyiv, Naukova Dumka [in Ukrainian].
13. Rezydent, N., Stepanova, N. (2023) Using the solid works flow simulation CFD package to study the performance indicators of the cyclone-utilizer. *Modern Technology Materials and Design in Construction*, 33(**2**), 192–197. DOI: https://doi.org/10.31649/2311-1429-2022-2-192-197
14. Akca, E., Trgo, E. (2015) Metallographic procedures and analysis — A review. *Periodicals of Eng. and Natural Sci. (PEN)*, 3(**2**), 9–11. DOI: https://doi.org/10.21533/pen.v3i2.51
15. Korzhyk, V., Gao, S., Khaskin, V. et al. (2024) Features of the stress-strain state of 3D metal objects produced by additive microplasma deposition of the powder of a Fe–Cr–Ni–B–Si system. *Applied Sci.*, **14**, 4159. DOI: https://doi.org/10.3390/app14104159
16. Sidharth, Rana R., Pandey S. (2023) Configuring microplasma for material process optimization. *Materials Today: Proceedings*. DOI: https://doi.org/10.1016/j.matpr.2023.01.339

ORCID

V.Yu. Khaskin: 0000-0003-3072-6761,
K.M. Sukhyi: 0000-0002-4585-8268,
O.V. Ovchynnykov: 0000-0001-5209-7498,
O.V. Zaichuk: 0000-0001-5209-7498

CONFLICT OF INTEREST

The Authors declare no conflict of interest

CORRESPONDING AUTHOR

V.Yu. Khaskin
E.O. Paton Electric Welding Institute of the NASU
11 Kazymyr Malevych Str., 03150, Kyiv, Ukraine.
E-mail: khaskin1969@gmail.com

SUGGESTED CITATION

V.Yu. Khaskin, K.M. Sukhyi, O.V. Ovchynnykov, O.V. Zaichuk (2025) Application of microplasma deposition for 3D printing of aerospace engine parts. *The Paton Welding J.*, **4**, 12–21.
DOI: https://doi.org/10.37434/tpwj2025.04.03

JOURNAL HOME PAGE

https://patonpublishinghouse.com/eng/journals/tpwj

Received: 05.03.2025
Received in revised form: 24.03.2025
Accepted: 08.05.2025

DOI: https://doi.org/10.37434/tpwj2025.04.04

WAYS TO INCREASE THE FATIGUE FRACTURE RESISTANCE OF WELDED JOINTS OF HIGH-HARDNESS ARMOR STEELS

O.A. Gaivoronsky[1], **V.D. Poznyakov**[1], **A.V Safinsky**[2], **A.V. Zavdoveev**[1], **T.O. Alekseenko**[1], **V.A. Yashchuk**[1]

[1]E.O. Paton Electric Welding Institute of the NASU
11 Kazymyr Malevych Str., 03150, Kyiv, Ukraine
[2]DP "Zhytomyr Armor Tank Plant"
1 Druzhby Narodiv Str., 12441, Zhytomyr Region, Novoguyvinske Urban Settlement, Ukraine

ABSTRACT

The influence of mechanical impact methods of treatment on the fatigue resistance of joints of high-hardness armor steels, compared to low tempering, in welding with high-alloy welding materials was studied. The paper presents the results of tests by cyclic out-of-plane bending of welded joints of HB500MOD armor steel, made using KhORDA 307Ti wire (08Kh20N9G7T alloying system), which were additionally subjected to layer-by-layer low-frequency peening of the deposited metal during welding, high-frequency peening of the fusion zone and adjacent HAZ metal and shot peening of the joint surface after their welding. It was established that thermal tempering of armor steel joints with a high-alloy weld does not contribute to an increase in the fatigue resistance. The most effective methods to increase the fatigue resistance of joints are mechanical high-frequency peening or enhanced shot peening after welding.

KEYWORDS: high-hardness armor steel, welded joints, fatigue fracture resistance, low tempering, mechanical low-frequency peening, mechanical high-frequency peening, shot peening

INTRODUCTION

The required set of mechanical and service properties of high-hardness armor steels is achieved through a special level of alloying with elements that strengthen ferrite and increase the steel temperability (C, Cr, Ni, Mo, V, B) and appropriate heat treatment — hardening followed by low tempering. High indices of strength ($\sigma_{0.2} \geq 1200$ MPa) and hardness ($HB \geq 500$) combined with relatively high ductile properties ($d_5 \geq 8$ %) ensure adequate bullet resistance of structures in light armored vehicles (LAV). High-hardness armor steels include domestic steel grade 71 and its foreign analogues, such as HB500MOD, ARMOX500, RAMOR500, etc.

According to the alloying system, high-hardness armor steels are classified as medium-carbon alloy steels. Welding of these steels is associated with the main problem — a high probability of cold crack formation in the HAZ metal of welded joints, which is predetermined by the formation of hardening structures of increased brittleness [1, 2]. This requires additional technological solutions in the manufacture of LAVs. Thus, to prevent the occurrence of cracks in welding with low-alloyed materials of the Mn–Si–Mo–Ti system, it is necessary to preheat welded joints, the temperature of which, depending on the level of steel alloying, can exceed 150 °C. If a high-alloyed wire of the Cr–Ni–Mo–Ti system is used, it is possible to weld without preheating due to the formation of hardening structures in the near-weld HAZ metal with a significantly lower level of internal stresses. This is evidenced by the results of studies described in detail in [3]. This welding method produces a hardenable martensitic-bainitic metal structure in the HAZ near-weld zone with an increased ability to microductile deformation without the formation of microcracks. The weldability of high-hardness armor steels in this area was studied in detail and technologies for welding LAV armor structures with high-alloy materials were developed, which are now used in production and ensure high-quality welded joints.

However, there is another problem in welding high-strength steels. It is associated with a limited durability and the formation of fatigue cracks in welded joints during the operation of products [4]. This is especially true for welded joints of armor structures located near the fasteners of the product propulsion system, which was repeatedly observed during the inspection of these areas. The mentioned cracks are located in the transition zone from the weld to the base metal and are initially small in size (up to 10 mm), but if they are not repaired in due time, they will further propagate actively with a transition to the base metal (Figure 1). In Soviet times, when armor steels were of lower hardness and less alloyed, and low-alloy materials were used in welding of LAV products, it was mandatory to perform a low tempering of a product no later than 24 hours after its welding to reduce the stress level and the probability of crack formation in welded joints during operation. Regarding the conditions for welding LAV structures with high-alloy materials, the feasibility of low tempering has not yet been fully determined. It should also be noted that this

Copyright © The Author(s)

technological operation requires specialized large-sized equipment, significant energy consumption and time. At the same time, the cost of low tempering can amount up to 30 % of the total cost of armored structures.

At present, less energy-consuming technological methods are known that provide an increase in the fatigue resistance of welded joints during long-term operation; they are scientifically substantiated and tested in the manufacture of civilian metal structures [5–7]. Among them, the most common are deformation technologies, in which, due to the introduction of mechanical energy, ductile deformation of welded joint areas occurs and the metal structure is refined. Under the influence of deformation, it is also possible to significantly reduce residual stresses in the welded joint and their concentration level in the transition zone from the weld to the base metal. All these positive changes should contribute to an increase in the crack resistance of welded joints of armor steels under cyclic loads and their durability in general. Such deformation technologies may include mechanical impact treatment methods, among which the most common are low-frequency (up to 10 Hz) layer-by-layer peening of weld metal during joint welding and post-weld high-frequency (over 5 kHz) peening of the fusion zone and overheating area of HAZ. Impact methods also include shot peening of metal, including welded joints, which is a common technological operation in the manufacture of LAVs.

In this regard, studies to determine the possibility of using energy-saving treatment technologies without low tempering to increase the crack resistance and durability of high-hardness armor steel joints are relevant.

THE AIM

of this work was to conduct a comparative assessment of the effect of mechanical impact treatment methods for welded joints of high-hardness armor steels, in the manufacture of which high-alloy welding materials are used, on their resistance to fatigue crack formation. This will allow making a final determination of the feasibility of low tempering and the choice of effective technological operations in the modern manufacture of LAVs to increase their service life.

MATERIALS AND METHODS OF RESEARCH

Welded joints of typical high-hardness armor steel HB500MOD of the following composition were used as an object of the studies, wt.%: 0.26 C; 0.21 Si; 0.78 Mn; 0.42 Cr; 0.74 Ni; 0.27 Mo; 0.06 V; 0.002 V. For comparative tests, V-groove butt joints of 400×480 mm in size and 10 mm thick were prepared, which were produced with a full penetration and a partial root welding on the back side. The joints were mechanically welded in a mixture of shielding gases (82 % Ar + 18 % CO_2) using high-alloyed KhORDA

Figure 1. Fatigue crack in a welded joint of a LAV product after long-term operation

30 7Ti wire of domestic production (analogue of Sv-08Kh20N9G7T wire) with a diameter of 1.2 mm on the following mode: welding current 160–180 A, arc voltage 26–28 V, welding speed 12–15 m/h. No preheating was used during their welding. To compare the effect of low tempering, in welding under similar conditions using low-alloyed Sv-10GSMT wire (Soviet era technology), the metal preheating was 100 °C.

The following technological operations (methods) of treatment were used to prepare welded joints for their testing:

- No. 1 (basic) — without low tempering of the joint and any impact treatment methods;
- No. 2 — low tempering (230 °C, 3 h) within 15–20 h after welding;
- No. 3 — low-frequency peening (up to 10 Hz) of the deposited metal layers during the welding process;
- No. 4 — high-frequency peening (more than 5 kHz) within 4 days after welding;
- No. 5 — shot peening within 4 days after welding of the joint according to the accepted technology of LAV manufacturer;
- No. 6 — enhanced additional shot peening of the weld metal and HAZ area along the welded joint.

The peculiarities of using impact treatment methods for welded joints were as follows. For example, low-frequency layer-by-layer peening of the deposited metal was performed during the welding process after the joints were cooled to a temperature of 100–50 °C. Since the thickness of the metal was 10 mm and the butt joint was welded in three layers, only the 2nd layer of the weld was peened (until the surface pattern of the deposited metal changed by 70–90 %). The root and final layers were not peened, as is recommended when using this method. To implement the peening process, a conventional electromechanical tool with a diameter of 3–5 mm at the tip of the strike was used. The rate of treatment of the weld layer surfaces was 100 mm per 1 min.

High-frequency (more than 5 kHz) peening was performed on the surface of the fusion zone and the

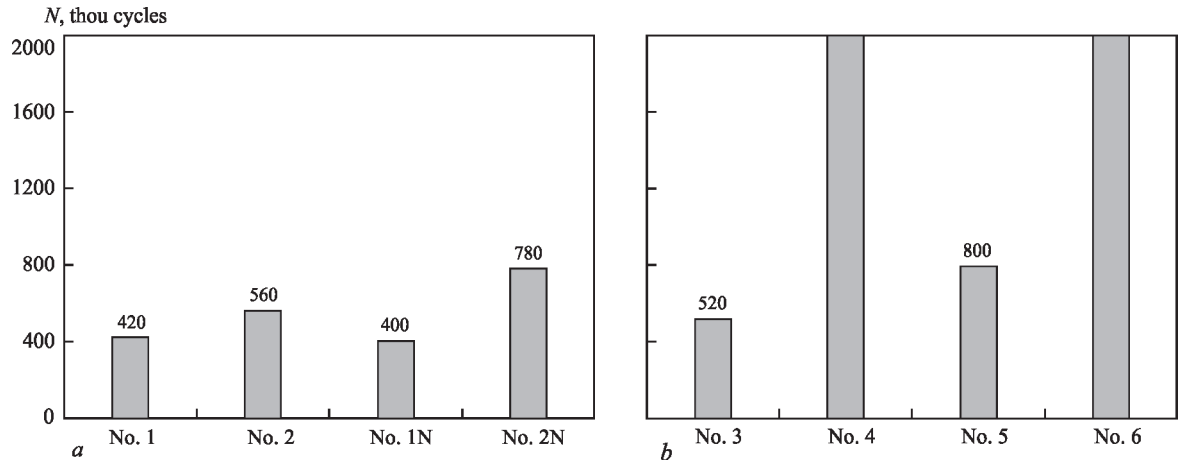

Figure 2. Fatigue cracks resistance of welded joints of armor steel HB500MOD made using KhORDA 307 Ti and Sv-10GSMT wire (N marking), Nos 1–6 — treatment methods: *a* — effect of low tempering; *b* — effect of impact treatment methods

adjacent HAZ metal of the welded joint, the width of the treated area was 2.0–2.5 mm. Here, a specialized tool was used according to the developed recommendations for the use of this method [7, 8]. The speed of the tool movement during peening was 1 mm/s. At the same time, a characteristic round-shaped groove of 0.3 mm deep was formed in the treatment area.

Shot peening is a technological operation in the manufacture of LAV products at specialized enterprises, which is necessarily performed on a finished product before its painting. In our work, shot peening of welded joints was performed under the conditions of the SE "ZhBTZ" with the equipment and treatment technology used in mass production. The shot diameter was 2–3 mm. Shot peening was performed on the facial and back sides over the entire surface of welded plates using conventional technology (No. 5) and with enhanced additional treatment of the joint surface (No. 6). The treatment rate was 100 mm per 1 min.

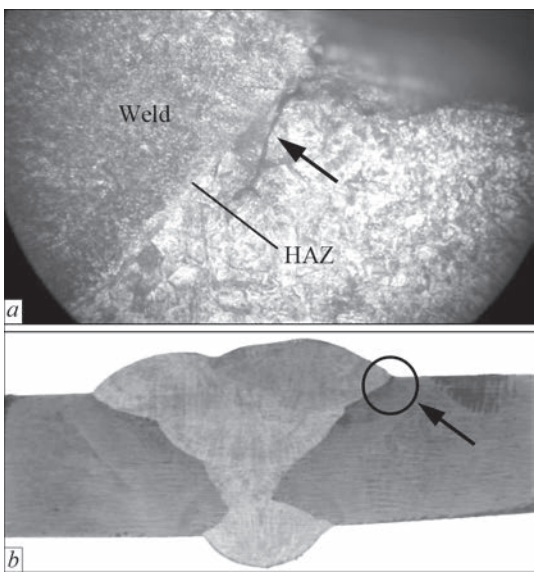

Figure 3. Typical fatigue crack formation and propagation (*a*, ×100) in welded joints (*b*) of armor steel HB500MOD

Then, from each butt joint prepared by the mentioned method (Nos. 1–6), 3 specimens of 480×120 mm were cut out, which were tested at cantilever bending under symmetrical cyclic loading with maximum cycle stresses of 60 MPa in accordance with generally accepted methods for testing the durability of welded joints [9, 10]. For this purpose, a specialized fatigue resistance testing machine of the UMP-1 type was used. The cyclic loading frequency was 14 Hz. The evaluation criterion was the number of loading cycles (N), at which a critical fatigue crack of 3 mm length was formed in the welded joint. If no typical signs of a crack were detected within 2 mln cycles, the loading was stopped and this was an index of the best resistance of welded joints to fatigue crack formation.

Metallographic examinations of welded joints were performed using light microscopy (Versamet-2, Neofot-32), microhardness was measured in the Leco M-400 microhardness tester.

RESEARCH RESULTS AND THEIR DISCUSSION

The summarized results of comparative fatigue tests of welded joints under cyclic out-of-plane bending are shown in Figure 2. It should be noted that under all the considered welding and treatment variants, fatigue cracks were initiated at the transition from the weld to the base metal and further propagated deep into the welded joint in the HAZ metal (Figure 3).

As is seen from the data in Figure 2, *a*, low tempering of joints with high-alloy welds, which was performed after the specimens had been aged for 15–20 h (No. 2), had a negligible effect on increasing their durability. The number of load cycles before the formation of fatigue cracks increased by 30 % (from 420000 to 560000, respectively), and in welding with low-alloy material (No. 2N), the value increased almost twice (from 400000 to 780000 cycles). In the initial state without heat treatment, the durability of joints in welding with high- and low-alloy materials is

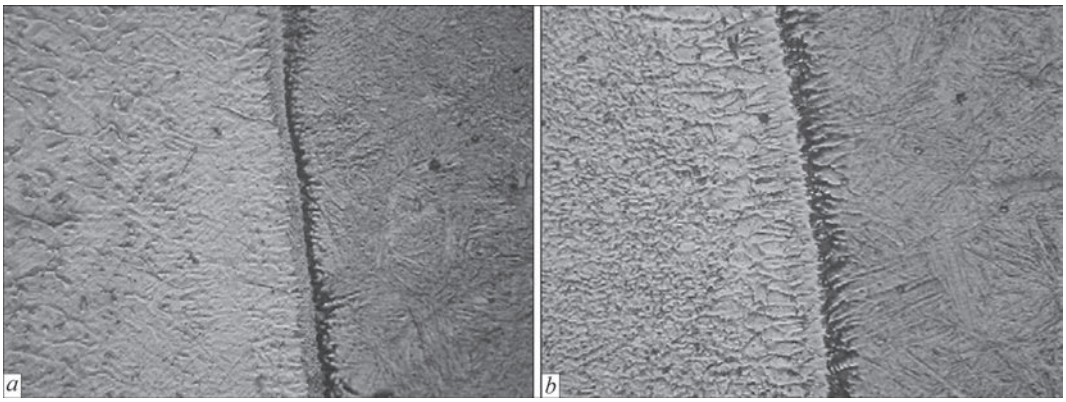

Figure 4. Typical fusion zone in welded joints of HB500MOD steel with high-alloy weld (×500): *a* — in the middle part of the joint; *b* — in the upper part of the joint

approximately the same (No. 1 and No. 1N). A slightly higher fatigue cracking resistance (by about 5 %) of the joints made using KhORDA 307 Ti wire is associated with the peculiarities of hardened structure formation in the HAZ metal when using high-alloy wire.

In our opinion, a slight increase in the resistance to fatigue fracture of welded joints of steel with a high-alloyed weld is associated with the embrittlement of the fusion zone at thermal tempering due to the development of carbon diffusion processes. The formed brittle interlayers are small in size (up to 5 μm) (Figure 4), but their presence is sufficient to reduce the resistance of metal to fatigue crack formation under external load.

Layer-by-layer peening of the deposited metal during the welding process promoted an increase in the durability of the joint by only 25 %. The number of cycles before fatigue crack formation increased from 420 to 520 thou (Nos 1 and 3). However, it should be considered, that in welding with high-alloy materials, this treatment method can be used to reduce deformations in joints and preserve the geometric dimensions of the armor structure.

The greatest impact on an increase in the durability of welded joints of armor steel HB500MOD with a high-alloy weld was caused by a high-frequency peening of the fusion zone and the adjacent HAZ metal. At the same time, a fatigue crack did not form in the welded joint even under a load of 2 mln cycles or more (the test was stopped at 3 mln cycles).

Metallographic examinations have demonstrated that the structure of armor steel welds in the initial state is austenitic-ferritic, with a microhardness in the weld centre *HV* 2210–3660 MPa. A bainitic-martensitic (B–M) structure with a microhardness of 3360–4640 MPa and a package size of 40–200 μm is formed in the metal of the HAZ overheating area. The structure in the base metal is also B–M, but of a lower hardness (3220–4010 MPa) and more dispersed (25–70 μm). After high-frequency peening, the microhardness of the metal increases by an average of 1.2 times (up to 3360–4210 MPa) in the adjacent deformed weld area. The structure refinement to 10–30 μm is observed. Similar changes occurred in the HAZ overheating area. At a depth of up to 125 μm, the size of packages is already 25–50 μm (4 times decreased), and the microhardness increases to 4640–5520 μm. Typical changes in the metal structure after high-frequency peening are shown along the fusion line in Figure 5, *a*. For comparison, Figure 5, *b* shows the changes in the structure when namely the base metal was peened. It also shows the structure refinement from 25–70 to 15–25 μm and an increase in the microhardness from 3220–4010 to 4210–4880 MPa to a depth of 125 μm.

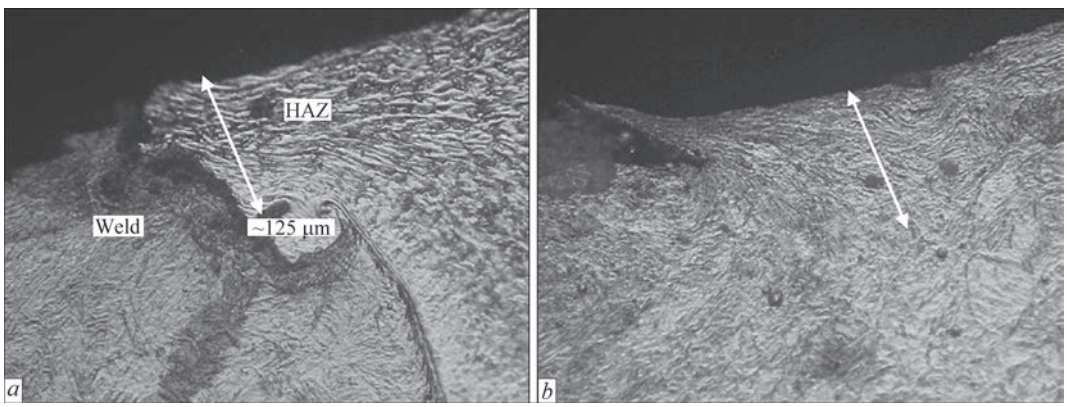

Figure 5. Changes in the weld metal and HAZ structure (*a*) after high-frequency peening along the fusion line of the welded joint and in the base metal (*b*) (×500)

Shot peening of the entire surface of the plates after welding using conventional LAV preparation technology (No. 5) can increase the fatigue fracture resistance of the joint by almost 2 times, up to 800 thou cycles. After enhanced additional treatment (No. 6) of the joint itself, fatigue tests did not cause crack formation even at a load of 2 mln cycles or more, as in the case of high-frequency peening. Metallographic examinations were not carried out at this treatment variant, but it can be assumed that similar structural changes occur in the metal structure of the joints. The physics of the processes of their influence on the formation of metal properties in both methods is approximately the same. As a result of the treatment, the weld metal and HAZ are cold work hardened, and compressive stresses are formed in the surface layer of the joints. Such positive changes contribute to a significant increase in the durability of welded joints of armor steel HB500MOD.

CONCLUSIONS

1. Low tempering of welded joints of high-hardness armor steel HB500MOD made using low-alloy materials such as Sv-10GSMT with preheating allows increasing their fatigue fracture resistance twice. In welding of armor steel joints without preheating using high-alloy KhORDA 307 Ti wire, the use of low tempering is not effective, which is associated with embrittlement of the fusion zone during thermal tempering due to the development of carbon diffusion processes.

2. Layer-by-layer peening of the deposited metal during welding of high-hardness armor steel using high-alloy materials contributes to an increase in the durability of fatigue fracture resistance of joints by 25%. This is a slight increase, but this treatment method can more effectively reduce the level of deformations in joints and preserve the geometric dimensions of armor structures during their manufacture.

3. It is possible to significantly increase the durability of welded joints of armor steel HB500MOD without the formation of fatigue cracks at a load of 2 mln cycles or more by high-frequency peening of the fusion zone and near-weld metal of HAZ joints or by their enhanced shot peening. In this case, the structure is refined several times in the near-surface metal layer to a depth of 125 μm, and compressive stresses are formed in the treatment area, which has a positive effect on the resistance of welded joints to fatigue fracture.

REFERENCES

1. Efimenko, M.G., Radzivilova, N.O. (2003) *Metal science and thermal processing of welded joints*. Kharkiv, NTU KhPI [in Ukrainian].
2. Anokhov, A.E., Korolkov, P.M. (2006) *Welding and heat treatment in power engineering.* Kyiv, Ekotekhnologiya [in Ukrainian].
3. Gaivoronskyi, O.A., Poznyakov, V.D., Berdnikova, O.M. et al. (2020) Influence of low-temperature tempering on structure and properties of welded joints of high-strength steel 30Kh2N2MF. *The Paton Welding J.*, **6**, 20–26. DOI: https://doi.org/10.37434/tpwj2020.06.04
4. Dronov, V.S., Golovin, S.A. (2004) Limited durability and crack resistance of high- and medium-strength steels. *Materialoznavstvo*, **12**, 41–47 [in Ukrainian].
5. Paton, B.E. (2000) Modern trends toward increase in strength and life of welded structures. *The Paton Welding J.*, **9–10**, 3–8.
6. Lashchenko, G.I., Demchenko, Y.V. (2008) *Energy-saving technologies for post-welding processing of metal structures.* Kyiv, Ekotekhnologiya [in Ukrainian].
7. Knysh, V.V., Kuzmenko, A.Z. (2005) Increasing the fatigue resistance of welded joints by high-frequency mechanical peening. *Svarshchik*, **2**, 19–21.
8. Bonnen, J.J., Mandapati, R., Kang, H., Iyengar, R.M. et al. (2009) Durability of advanced high strength steel gas metal arc welds. *SAE Inter. J. of Materials and Manufacturing*, 2(**1**), 155–171.
9. Kovalchuk, V.S., Knysh, V.V., Poznyakov, V.D., Kasatkin, S.B. (2007) Method for increasing cyclic and service life of welded steel structures. *The Paton Welding J.*, **3**, 37–38.
10. Cabrilo, A., Sedmak, A., Burzic, Z., Perkovic, S. (2019) Fracture mechanics and fatigue crack propagation in armor steel welds. *Engineering Failure Analysis*, **106**, 104155. DOI: https://doi.org/10.1016/j.engfailanal.2019.104155

ORCID

O.A. Gaivoronsky: 0000-0002-8146-7790,
V.D. Poznyakov: 0000-0001-8581-3526,
A.V. Zavdoveev: 0000-0003-2811-0765,
T.O. Alekseenko: 0000-0001-8492-753X

CONFLICT OF INTEREST

The Authors declare no conflict of interest

CORRESPONDING AUTHOR

V.D. Poznyakov
E.O. Paton Electric Welding Institute of the NASU
11 Kazymyr Malevych Str., 03150, Kyiv, Ukraine.
E-mail: paton39@ ukr.net

SUGGESTED CITATION

O.A. Gaivoronsky, V.D. Poznyakov, A.V Safinsky, A.V. Zavdoveev, T.O. Alekseenko, V.A. Yashchuk (2025) Ways to increase the fatigue fracture resistance of welded joints of high-hardness armor steels. *The Paton Welding J.*, **4**, 22–26.
DOI: https://doi.org/10.37434/tpwj2025.04.04

JOURNAL HOME PAGE

https://patonpublishinghouse.com/eng/journals/tpwj

Received: 12.10.2024
Received in revised form: 21.01.2025
Accepted: 07.05.2025

DOI: https://doi.org/10.37434/tpwj2025.04.05

ELECTRON BEAM WELDING OF GAS VALVE ELEMENTS FROM Mo–Ti–Zr ALLOY

V.I. Zagornikov, V.M. Nesterenkov, K.S. Khripko, O.N. Ignatusha

E.O. Paton Electric Welding Institute of the NASU
11 Kazymyr Malevych Str., 03150, Kyiv, Ukraine

ABSTRACT

The technological techniques of electron beam welding (EBW) are considered, the application of which would allow obtaining the required quality of joints of gas valve parts made of Mo–Ti–Zr (TZM) alloy, which is used in difficult conditions of the nuclear industry. It is known that in order to produce a welded joint with relatively high ductility indices, the oxygen content should not exceed thousandths of a percent. Alloys produced by vacuum arc and electron beam melting are used for welded structures. They have a much lower tendency to form porosity in welded joints than similar alloys made by powder metallurgy methods. Such alloys can be welded, but these joints cannot always be used under dynamic loads. When choosing the optimal welding technique for gas valve parts, technical requirements for edge preparation, quality of welded joints, availability of appropriate equipment and technological tooling were taken into account. The problems of assembly and subsequent welding of gas valve parts made of Mo–Ti–Zr (TZM) alloy revealed during the investigations caused the need in changing design of the joints. As a result, a scheme for welding gas valve parts was proposed, which uses flanging of weld butt edges. This led to optimizing the penetration shape. The proposed welding parameters and flange geometry made it possible to lower the degree of saturation of the weld metal with gases due to the reduction in the penetration depth under the conditions of rapid heat removal and, as a result, to produce sufficiently high-quality welded joints. In addition, with all the variety of technological techniques used during the investigations, the priority of the correctly selected design of the circumferential butt and the accuracy of the welding assembly was proven.

KEYWORDS: Mo–Ti–Zr (TZM) alloy, electron beam welding (EBW), microstructure, porosity, gas valve, flanging of welded edges

INTRODUCTION

Molybdenum and its alloys have many unique characteristics, which makes them indispensable in such areas as aerospace, power, chemical defense, and metallurgy. The use of molybdenum-based alloys in nuclear engineering in future thermonuclear reactors is challenging, since these alloys, along with high strength and fatigue resistance at high temperatures, have good thermophysical properties and are not activated by irradiation. The use of molybdenum as the base of a structural alloy is constrained by its two disadvantages: easy oxidation at temperatures above 500–700 °C and reduced ductility at room temperature [1]. Molybdenum alloying practically does not help to eliminate the first drawback, but it can significantly increase the recrystallization temperature, strength, and creep resistance at high temperatures, and, in case of dispersive hardening, for example, with lanthanum oxide, increase heat resistance and improve the ductile properties (reduce the brittleness threshold).

It is known that the presence of impurities in the base metal in quantities significantly exceeding their solubility limit is an objective obstacle in producing high-quality welded joints on molybdenum alloys [2, 3]. The quality of welded joints, mechanical characteristics of welds, and especially their low-temperature ductility are very sensitive to the structural state of the initial material. To obtain a sufficiently high ductility of the welded joint, especially at low temperatures, it is necessary that the base metal has a homogeneous initial structure and sufficiently high resistance to ductile-to-brittle transition. This can be achieved by selecting the most favorable conditions for preliminary hot treatment of the metal to be welded (for example, rolling mode for sheet alloys), as well as heat treatment before welding (for example, for molybdenum alloys at a temperature of 1400–1800 K, depending on their composition) [4].

It should also be taken into account that any alloys of refractory metals of the VIa subgroup of the periodic table (including molybdenum alloys) produced by vacuum arc or electron beam remelting have a much lower tendency to form porosity in welded joints than similar alloys produced by powder metallurgy. This is usually predetermined by the fact that powdered metals have a higher content of gas impurities. However, welded joints made with powdered alloys, even with lower impurity content than those made with conventionally produced alloys, tend to reveal porosity. During the welding process, gases can expand rapidly in the molten pool, which seriously degrades the quality of welded joints of molybdenum and molybdenum alloys [5–7].

Copyright © The Author(s)

The use of powdered Mo–Ti–Zr (TZM) molybdenum alloy is constrained by its low processability and especially weldability. The weld and heat-affected zone (HAZ) are relatively wide, and the grains are highly coarsened after welding, so penetration impurities such as C, N and O are fully diffused and concentrated at the grain boundaries, resulting in a significant weakening of the bond strength at the grain boundaries. At the combined effect of intrinsic brittleness of materials and segregation of impurities at grain boundaries, the sensitivity to welding cracks is high, and the strength and ductility of joints of molybdenum and its alloys are low [8, 9]. At even the lowest level of impurities-gases in the weld, it is impossible to ensure sufficient ductility of welded joints with their typical coarse-crystal structure and eliminate the tendency to cold crack formation. Producing high-quality welded joints requires the use of alloys doped with expensive elements that reduce the harmful effect of impurities on welds (e.g., deoxidizers such as titanium, zirconium, etc.) and improve their structure (e.g., with rhenium) [10]. Therefore, parts or structures made of molybdenum and molybdenum alloys often have to be manufactured by powder metallurgy rather than by welding from parts.

Since the most perfect shielding of the weld from atmospheric gases is achieved in EBW, this method is most effective for joining chemically active refractory metals, since it is performed in a vacuum and provides relatively low heat input. For refractory and chemically active metals, the possibility of their preliminary cleaning by degassing in a vacuum is of great importance. To reduce contamination of the weld metal, welding is usually performed without filler metal.

The relatively small width of the HAZ becomes a great advantage in welding refractory metals such as molybdenum. The weld and the near-weld zone (recrystallization zone) are much less strong and have a much higher ductile-brittle transition temperature than the base material itself. This difference in strength leads to a concentration of strain in the weld zone, and the triaxial stress created by the confinement of the base metal can initiate fracture. It should be noted that although vacuum electron beam welding facilitates the removal of impurities and gases, it increases the evaporation of alloying elements.

Experimental works are mainly devoted to clarifying the role of welding conditions and parameters, or more precisely, their role in improving weld quality (tempering brittleness, limitation of continuous grain growth). The information provided in the literature on the effect of heating and cooling rates on the low-temperature ductility of molybdenum alloys is contradictory. Morito et al. [11] compared the ductility of HAZ in welding molybdenum alloys (Mo > 99.9 wt.%) under two heat treatment conditions, i.e., at cooling in a furnace and rapid cooling by quenching. It was found that rapid cooling after welding can significantly reduce the ductility of the HAZ of a welded joint of molybdenum alloys, mainly because grain boundary segregation in the HAZ is greater at rapid cooling by quenching. Stutz et al. [12] systematically studied the influence of EBW process parameters on the sizes of the melting zone and HAZ, pore and crack sensitivity in a butt welded joint made of TZM alloy with a thickness of 2 mm.

The results show that pore formation is seriously affected by excessive heat input during welding. A small (insignificant in terms of the degree of manifestation) heat input can not only suppress pores, but also obviously reduce the grain size in the melting zone.

It was found in [5] that although it is not possible to completely avoid pore formation in welding powdered metals, the porosity in the melting zone at a limited heat input is significantly reduced. By increasing the welding speed and reducing the heat input, the ductility of the welded joint of molybdenum can be significantly improved by refining the weld structure. This results in a significant reduction in the thickness of the MoO_2 oxide film located at the grain boundaries. Reducing the thickness of the oxide film along the grain boundaries increases the intercrystalline bonds and, consequently, the ductility [13].

THE AIM

of the research is to develop a technique for electron beam welding of circumferential welds while joining gas valve parts made of Mo–Ti–Zr molybdenum alloy.

RESEARCH METHODOLOGY

EBW opens up the possibility to clean the metal from gases before welding by heating the butt edges with a defocused electron beam. Hydrogen is removed most successfully, oxygen and nitrogen are removed least successfully, and only from the surface layers of the metal. It is assumed in [14] that preheating of the butt reduces pores and helps to remove surface contaminants of adsorbed gases that cause porosity, calmer formation of the substructure in the weld, and prevents the formation of cold cracks in the studied alloy due to the overall expansion of the future welding zone. It is noted that heating at temperatures above 900 °C is inappropriate due to possible deformation of parts and the beginning of the recrystallization process.

A necessary condition for producing high-quality welded joints is the accuracy of the assembly (and fixation) of the butt for welding. For example, when welding circumferential joints made of molybdenum

alloys, it is recommended that the edge displacement should not exceed ±50 μm. Assembly of parts for welding should be carried out in particularly precise devices. These devices must ensure that the edges to be welded are pressed tightly together, as effective heat removal is required to reduce welding deformations [15]. The Mo–Ti–Zr alloy, which is produced by powder or pellet metallurgy, guarantees chemical compliance of the basic alloying elements and mechanical strength in the delivery state, i.e. it can be used for technical tasks that do not require metal remelting. However, this material is problematic for structures joined by electron beam welding.

In our work, the technological methods of electron beam welding are considered, the application of which makes it possible to obtain the required quality of welded joints of gas valve parts made of Mo–Ti–Zr alloy, including the conditions for assembling parts for welding. We studied the effect of the joint type of parts with circumferential welds produced by electron beam welding on the strength and ductility of such a joint. Such joints are the most critical in terms of crack formation and are problematic at an attempt to produce a serviceable welded joint. The work also touched the issue of the influence of gases, primarily oxygen (O_2) on weldability at different types of gas valve part joints produced by electron beam welding.

The design of the nipple joint to the gas valve body is fixed in the assembly fixture on a welding rotary positioner (rotator). The rotator being a part of the installation kit allows mounting in two spatial positions: with a horizontal or vertical axis of rotation (Figure 1). Using an indicator post and a clock-type indicator, the nipple was aligned with the positioner's axis of rotation. The deviation was within 0.1 mm.

Welding was carried out in an electron beam installation of the KL-211 type with a pressure in the working volume of the chamber not higher than $5 \cdot 10^{-4}$ mm·Hg. The accelerating voltage is set at a level of 60 kV. Electronic optics was used, designed for 500 mA of electron beam current. It included a metal cathode with an emitting surface with a diameter of 3 mm. The experiments were carried out at a working distance of 250 mm from the end of the welding gun to the facial surface of a product.

The influence of the input energy was studied, namely three fixed values of the welding speed: 5, 10 and 15 mm/s, in the range of heat input q = 320–540 J/mm.

Figure 1. KL-211 installation. Device for assembling and welding gas valve simulator in two spatial positions: with horizontal (*a*) and vertical axis of rotation (*b*)

Metallographic examinations of the weld penetrations were carried out in the Neophot-32 optical microscope at different magnifications. The grain size was calculated by the linear method. The hardness of the phase components was measured in the M-400 microhardness tester from LECO, the load was 1 N, the holding time was 10 s.

The composition of the alloy was checked using an X-Ray Spectrometer X'Unique II — Rh 80 kV LiF220 Ge111 TIAP. The obtained data of chemical and gas analysis of the alloy are presented in Table 1.

The first EBW test specimens showed elevated brittleness of the weld metal and the base metal itself. In order to prevent the formation of unacceptable pores and cold cracks in the studied alloy, the techniques were used, which are discussed below.

The initial selection of welding modes was carried out on a set of 50×240×25 mm plates with non-through and through penetration. To obtain an acceptable formation of a facial weld bead, the specimens were welded by changing the parameters of the elec-

Table 1. Chemical composition of molybdenum TZM alloy

Elements	Mo	Ti	Zr	Al	Si	Cr	La	C	O_2	N_2
wt.%	≤99.23	≤0.53	≤0.13	≤0.046	≤0.041	≤0.013	≤0.037	≤0.031	≤0.0092	≤0.001

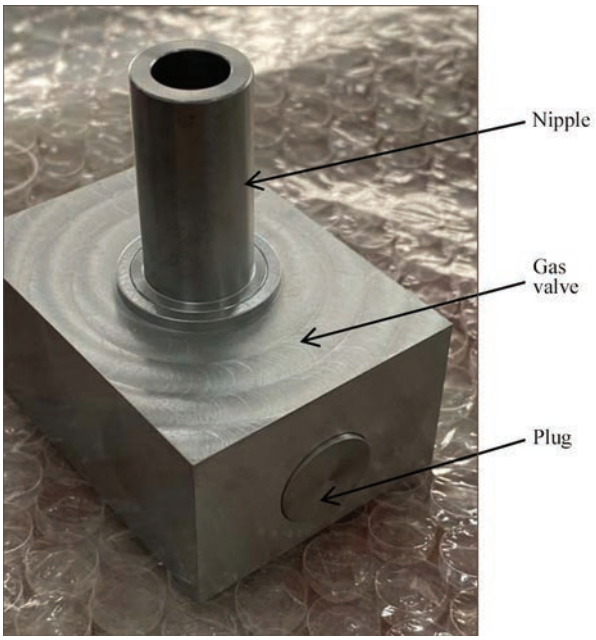

Figure 2. Assembled parts of Mo–Ti–Zr alloy gas valve simulator

tron beam focusing, its current and welding speed. In accordance with the recommendations [14], to increase the deformability of the metal, preheating of the joint was used. The reference surface temperature was 900 °C. The following mode of electron beam heating of the welding zone was selected: accelerating voltage 60 kV, beam current 30 mA and heating time 12 min.

Each joint was welded separately, followed by cooling in vacuum for 30 min. After welding, mechanical tensile tests were performed on the specimens at temperatures of 20 and 1200 °C.

The influence of the welding input energy per unit time was studied. Different welds were produced by varying the beam current from 30 to 60 mA and the welding speed from 5 to 15 mm/s. The use of the focused electron beam is not rational, since it does not allow obtaining the required shape of the penetration zone. An acceptable level of electron beam concentration reduction of ±7 mA of the focusing current from its value at a sharp focusing (measured at minimum beam power) was experimentally determined. The weld geometry was optimized by using technological electron beam scanning.

Modes of welding the nipple with the gas valve body and two cylindrical plugs on opposite walls of the same body were tested (Figure 2).

ANALYSIS OF RESULTS AND TECHNOLOGICAL RECOMMENDATIONS

MICROSTRUCTURE OF WELDED JOINTS OF Mo–Ti–Zr *ALLOY*

Due to the effect of the thermal cycle of welding, grain growth in the near-weld zone, thickening of intergranular interlayers and their enrichment with impurities and a sharp increase in the brittleness of the metal in this zone occurs. The alloy is sensitive to the thermal cycles of welding and, above all, to the cooling rate, which is associated with the precipitation of the second phase. Therefore, the orientation of the weld metal crystals, the shape of the grain boundaries and the level of residual stresses mainly depend on the welding speed.

It was found that low heat input (q = 320 J/mm) due to increased welding speed leads to significant grain refinement in the melting zone.

Reduction in the speed to lower than 5 mm/s (q = 540 J/mm) increased the formation of pores. In addition, more pores are fixed in the fusion zone than in the volume of the weld. Also, welds with a high "wedge-like" penetration and a large total width of the penetration zone are formed. With an increase in the welding speed, both the average size of pores and their number decrease. On the other hand, the welding speed was limited, because welding at a speed exceeding 15 mm/s led to a decrease in the stability of the welded joint formation and the appearance of defects in the form of oscillations of the facial bead surface (Figure 3, *c*). At the same time, without scanning of the electron beam or at a small scanning width, a very sharp weld root with a high probability of root defects is naturally formed. By increasing the scanning width to 0.8 mm, a compromise was achieved between the

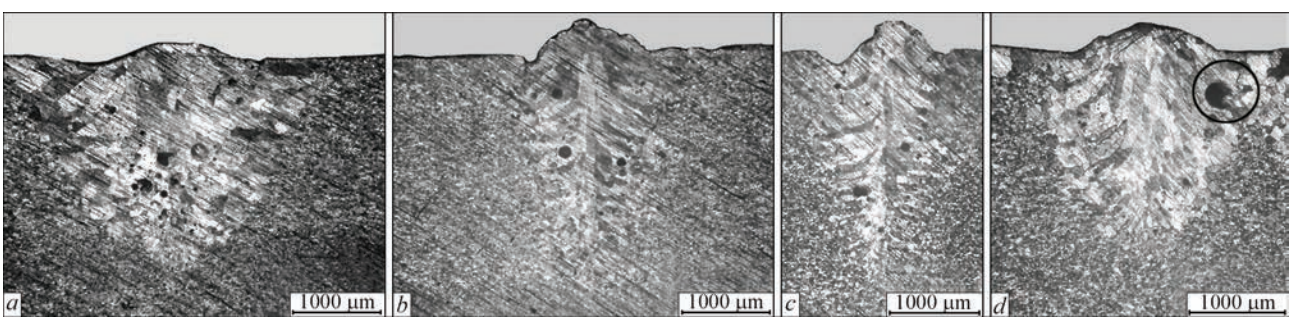

Figure 3. Penetration zone (×30): *a* — V_w = 5 mm/s, A_s = 0.8 mm, I_w = 45 mA, q = 540 J/mm; *b* — V_w = 10 mm/s, A_s = 0.8 mm, I_w = = 55 mA, q = 330 J/mm; *c* — V_w = 15 mm/s, A_s = 1.6 mm, I_w = 80 mA, q = 320 J/mm; *d* — with repeated penetration at V_w = 5 mm/s, A_s — 0.8 mm, I_w = 40 and 45 mA, respectively

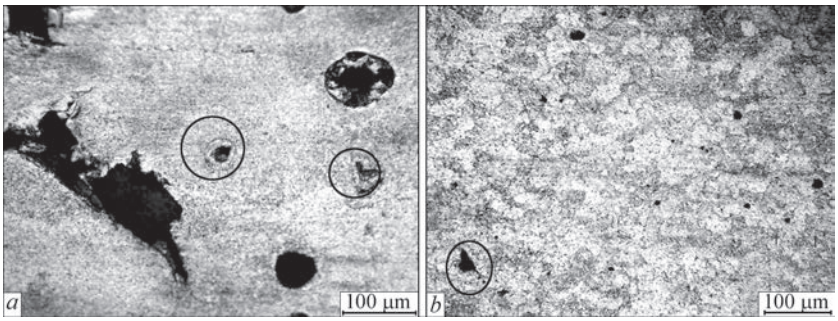

Figure 4. Defects in weld metal (*a*), defects in HAZ metal (*b*) (×200)

total width, the "wedge-like" shape of the penetration zone and the shape of the weld root (Figure 3, *a, b*).

In all the investigated weld penetrations, in addition to the macropores mentioned above, micropores were found in the weld metal. Defects are mainly globular in shape, but there are also single defects of irregular shape (Figure 4, *a, b*). The size of defects varies within 38–375 μm.

In the HAZ and in the base metal of the studied specimens, single micropores were also found, as well as inclusions of various sizes and in large amount. The bulk of these inclusions has a size of 2.5–5.0 μm, quite a lot of inclusions of 18–20 μm and a small number of large inclusions of 37.5–50 μm. The hardness (*HV*1) of the inclusions is in the range of 10180–12500 MPa.

To confirm the influence of an increased content of gas impurities in the base metal on the weld porosity, experiments on double metal remelting were conducted. We performed experiments on double metal remelting: both welding passes at similar parameters, but the first pass at 0.8–0.9 of the beam power at the second pass. I.e., at the second pass we completely remelted the weld metal from the first pass and touched a small interlayer of previously unremelted base metal. As was expected, in the center of the weld metal after remelting the number of pores decreased noticeably, but near the fusion zone there are still many of them as before (Figure 3, *d*).

Apparently, despite some «refining» of the weld metal as a result of the first pass, the high concentration of gases in the boundary interlayer and partial diffusion of gases from the base metal, as before, initiate the propagation of pores, and increased gaps — cracks.

The structure of the weld in all the studied cases represents coarse grains, elongated from the center of the weld in the direction of heat removal (Figure 3). The size of grains in the weld at a welding speed of 5 mm/s is 185–250 μm, and at a speed of 10 mm/s — 100–180 μm. The weld microstructure is everywhere two-phase, consisting of a light α-phase matrix (solid solution based on molybdenum) and an excess phase in the form of small inclusions of irregular shape (Figure 5, *a*).

The hardness (*HV*1) of the weld metal at a welding speed of 5 mm/s is 2280–2360 MPa, and near the fusion line it decreases to 2060 MPa. The hardness of the weld metal at a welding speed of 10 mm/s is somewhat higher — 2360–2660 MPa, and near the fusion line — 2280 MPa, respectively. The fusion line is not pronounced.

The HAZ microstructure is two-phase with embeddiments of inclusions described above (Figure 4, *b*). The grain size at a welding speed of 5 mm/s is 90–125 μm, the hardness (*HV*1) is 2210–2270 MPa, and at 10 mm/s — 60–100 μm and 2180–2430 MPa, respectively. The structure of the base metal is fibrous, retains the deformation texture, consists of two phases and precipitations (inclusions), the grains are not pronounced (Figure 4, *c*), the hardness (*HV*1) of the metal is in the range of 2790–3220 MPa (Figure 6).

All welded joints of a gas valve require a relatively small depth of partial penetration, namely 3–4 mm. With an increase in the thickness of the welded metals, serious difficulties arise due to overheating of the weld metal, an increase in HAZ and, as a result, the

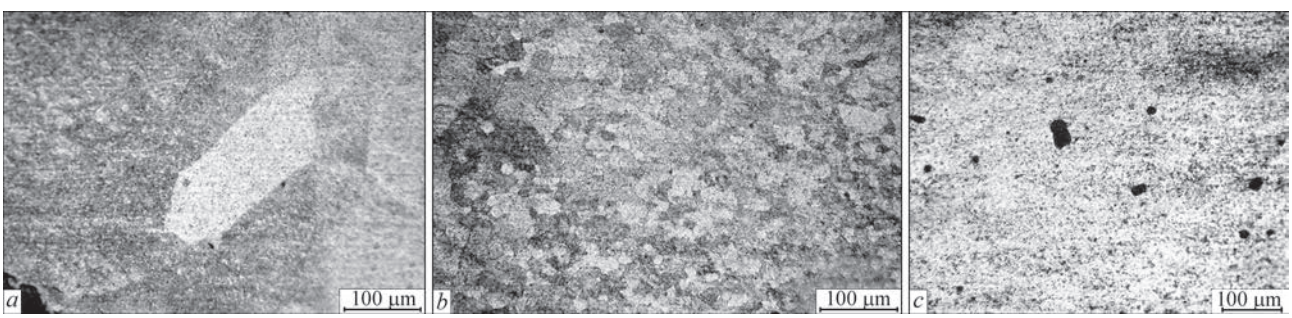

Figure 5. Typical structure of weld metal (*a*), HAZ metal (*b*), base metal (*c*) (×200)

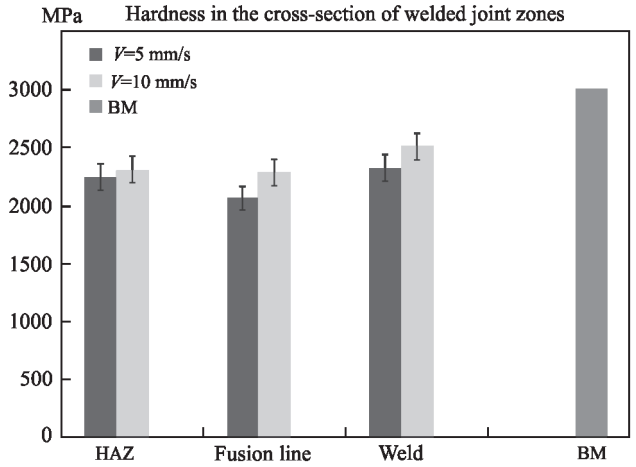

Figure 6. Average hardness of different welded joint zones at EBW and in the base metal

formation of pores and cracks. The use of the electron beam scanning technology made it possible to obtain the required shape of the penetration zone with a much lower tendency to porosity formation.

Taking into account the results of the choice of modes on plane specimens, a number of welding experiments were carried out to select and work out the welding modes of gas valve parts, namely three joints: a nipple with a valve body and two plugs on the opposite walls of this body. Two 16-mm diameter plug holes and one nipple connection were welded to a casing hole of 20 mm diameter. To exclude possible crystallization cracks, the shortest possible sections of the electron beam current input and output were selected. The actual valve parts were assembled in a device that allows welding of all parts of the assembly simultaneously.

GENERAL SEQUENCE OF WELDING-ON FITTINGS TO THE VALVE BODY

Welding algorithm: increment in the welding current to the specified value, holding this current constant during a 360° angular welding movement, then overlapping the initial section and, finally, gradual reduction in the welding current. The overlap length was chosen to prevent lack of penetration in the initial section of the joint and to prevent the formation of an end crater.

Parameters of local tacks (sections 10 mm each): beam current — 25 mA; beam focusing current — 560 mA; movement speed — 5 mm/s; circular beam scanning diameter — 1.0 mm.

The operation for preparing preheating of the butt remained relevant. To provide a uniform heating of the body and nipple, the electron beam was shifted from the butt towards the body by 8 mm. Heating parameters: beam current — 25–30 mA; beam focusing current — 500–510 mA. Movement speed — 5 mm/s; circular beam scanning diameter — 8 mm; number of passes — 15; reference temperature on the surface — 900 °C.

After heating, the subprograms for continuous tack welding and full penetration were run sequentially. Parameters of continuous tack: welding current — 25 mA, focusing current — 510 mA. Welding speed: 5 mm/s. Beam scanning — diameter circle of 1.0 mm.

Welding mode parameters were changed within the following limits: welding current — 30–48 mA, welding was performed with a defocused electron beam, focusing current — 560 mA. The welding (rotation) speed was 7–10 mm/s. Beam scanning — a circle with a diameter of 0.5–1.0 mm (Table 2).

Table 2. Parameters of preheating and EBW modes for gas valve parts

Parameters of preheating on the surface	
Nipple (bushing)	Plugs
Temperature — 900 °C; Number of passes — 15; Rotation speed — 5 mm/s; Current — 25–30 mA; Beam scanning — 8.0 mm circle, the beam is shifted at 8 mm towards the body from the joint; Focusing current — 500–510 mA	Temperature — 900 °C; Number of passes — 15 first, 10 second; Heating time — 10 min; Rotation speed — 7 mm/s; Current — 5–8 mA; Beam scanning — 2.0 mm circle; Focusing current — 500 mA

EBW stages	EBW stage parameters							
	Nipple (bushing)				Plugs			
	V_w, m/s	I_w, mA	I_f, mA	Beam scanning, appearance, size, mm	V_w, m/s	I_w, mA	I_f, mA	Beam scanning, appearance, size, mm
Short tacks (10 mm)	5	25	560	Circle, 1.0	5	25	510	Circle, 1.0
Solid tacks	5	25	570	Circle, 0.5	5	25	560	Circle, 0.5
Main weld	7–10	45–48	560	Circle, 0.5	10	40	560	Circle, 0.5
Smoothing pass	12	30	700	10	12	30	700	10

During the assembly, it was found that the gap value between the gas valve parts to be welded reached 0.1 mm, which does not meet the requirements specified for assembling units for EBW made of molybdenum alloys. The initial condition of providing the accuracy of the butt assembly was not met. Due to an increased gap in the butt during assembly, the risk of arising shrinkage cracks and root defects in the area with a crater increased. Nevertheless, the valve fittings were welded. Repeated penetration allowed forming the upper bead, but to correct the root defects, it was necessary to drill out the plug and insert a new part with a subsequent rewelding. Such a long and labour-intensive process was recognised as poorly manufacturable and was not considered further.

The research results showed that low heat input helps to delay pore growth and reduce grain size in the melting zone. The heat input was decreased by reducing the welding current, increasing the speed to a certain limit and optimizing the shape and sizes of the electron beam scanning.

Preparation of end surface of edges to be welded to reduce the porosity is necessary but not sufficient. In addition, preheating and remelting of this joint turned to be ineffective as a method of combating metallurgical pores. These operations do not solve the problem of increasing the ductility of a welded joint, but they were not cancelled due to the possible prospect of having a positive impact on the rate of phase and structural transformations without deteriorating the weld structure. It was necessary to search other ways to improve the weld quality. Difficulties that appeared during forming welds on gas valve parts made it necessary to change the design of the welded joint body-nipple and body-plugs.

It is known that one of the widely used technological methods aimed at increasing the resistance of the weld metal to pore formation and crystallization cracks is the change in the penetration shape (ratio of weld width to penetration depth). The carried out studies have shown challenge in terms of joining with flanging of welded edges, where primary crystallites are joined by side faces rather than apexes in the process of melt solidification. Such welds are more resistant to cracking.

STAGES OF WELDED ASSEMBLY MODERNIZATION

In the process of step-by-step changing in the assembly scheme and the design of the welded assembly, a solution was found to improve the manufacturability of the welding process. Figure 7, *a–c* shows the se-

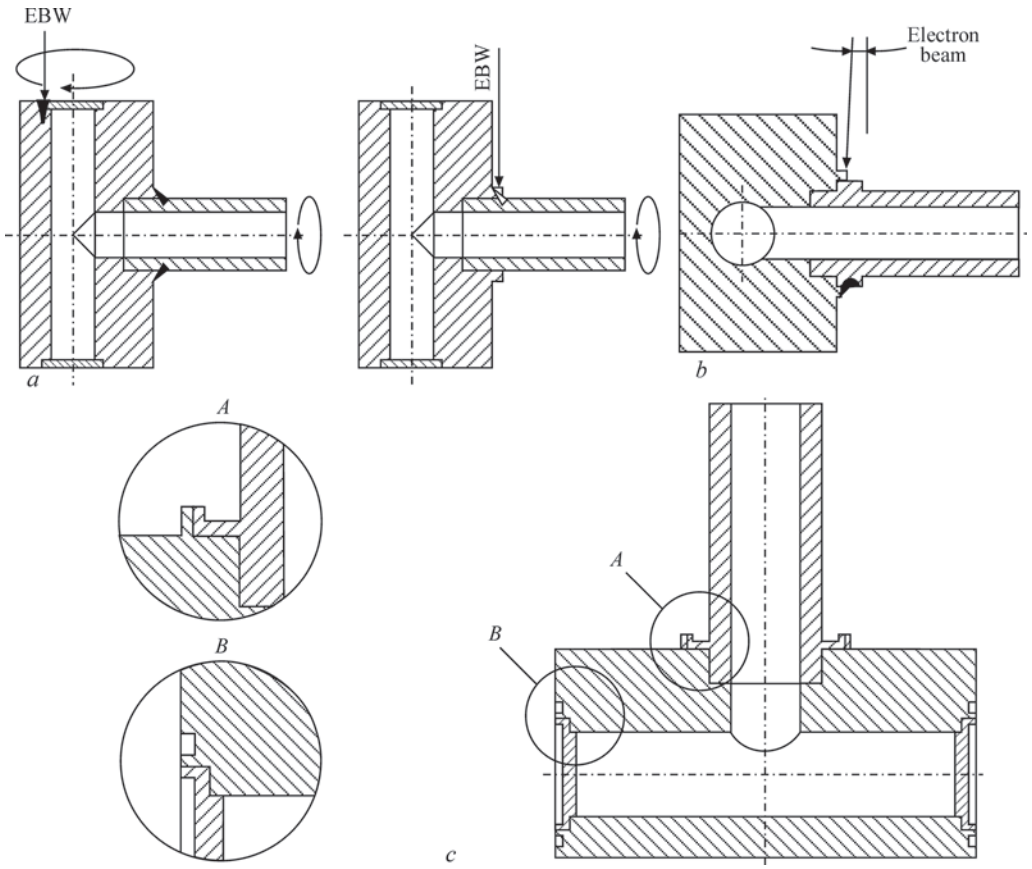

Figure 7. Three stages of modernization of the assembly welded joint design: fish-mouth welding of the nipple with the body is replaced by a scheme with a "collar" fused to the nipple wall, the body with plugs is fish-mouth welded (*a*), the nipple is modified for welding with an inclined electron beam (*b*), modernization of fitting joints in the form of flanging the joint edges (*c*)

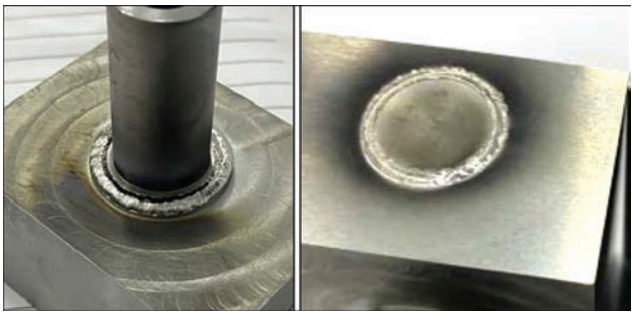

Figure 8. Formation of circumferential welds with edge flanging, imitating nipple-body and plug-body joints

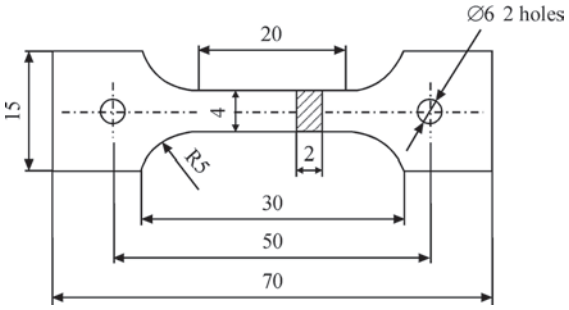

Figure 10. Tensile test specimen

quence of step-by-step transformation of joint variants, which was carried out as a result of the carried out studies.

Variant "*b*". The deflection angle and focus location of the electron beam have been clarified. It became possible to weld three butts within one evacuation of the welding chamber. However, the subsequent welding of gas valve parts, fittings and plugs, due to inacceptable gaps in the butt, did not provide the required tightness, as was shown by hydraulic tests. Therefore, it was proposed to fit the H7/p6 joint, which provides a small guaranteed tension in the joint. The operations to eliminate the gap in the butt joints before welding by high-precision grinding of gas valve parts provided the highest guaranteed tightness of the joint by obtaining the required fit.

Variant "*c*" was accepted as the basic one, and the drawings of gas valve parts were made in accordance with Figure 7, *c*. This variant simplifies the positioning of a part before welding. There is no need to weld with an inclined beam, as was assumed in one of the previous schemes.

All welds made with a "tight" joint (without a gap in a butt) had a fairly stable formation of the outer bead (Figure 8).

The advantages of this joint design include, first of all, the fact that it allows radically reducing the heat input during welding. The use of edge flanging makes it possible to achieve the most favourable ratio of the pool depth to its width. I.e., welding can be performed with a fairly wide and shallow weld at a moderate electron beam concentration. The presence of root defects in this case is not significant. Due to the thermophysical properties of the molybdenum alloy, the penetration shape of such welds in the cross-section remained rather wedge-shaped, but with a rounded root part. Figure 9 shows penetration shapes on the selected welding modes.

Selected modes for producing circumferential welds of joining fittings to the valve body:

- for plugs — V_w = 10 mm/s, focusing current 560 mA, beam scanning A_s = 0.5–0.8 mm, I_w = = 45–55 mA;
- for nipple — V_w = 7 mm/s, focusing current 570 mA, beam scanning A_s = 0.8–1.0 mm, I_w = = 30–45 mA.

Molybdenum is very sensitive to undercuts and therefore, they should be avoided as well as craters. The use of an additional smoothing pass reduces possible stress concentrators (including undercuts) and porosity in the most dangerous near-surface area. A smooth transition from the weld to the base metal is provided. The weld width is uniform, the surface is smooth and mirror-like on the facial side, and craters are absent.

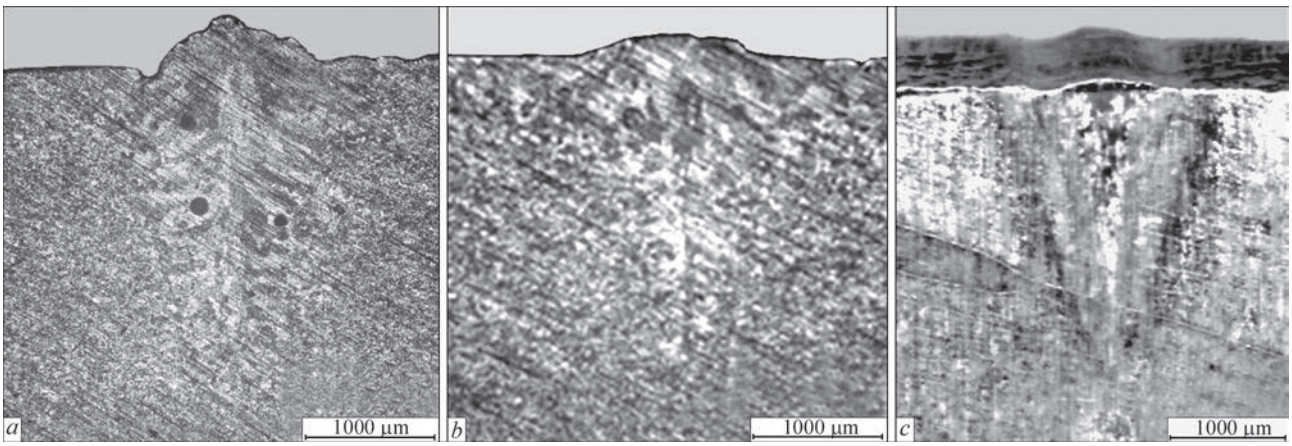

Figure 9. Cross-sectional view of the penetration zone under selected modes of producing circumferential welds: *a* — for plugs: V_w = = 10 mm/s, A_s = 0.8 mm, I_w = 55 mA; *b* — for nipple: V_w = 7 mm/s, A_s = 0.8 mm, I_w = 30 mA; *c* — the same with a smoothing pass V_w = 10 mm/s, I_w = 45 mA

Table 3. Mechanical properties of base metal and welded joint metal at different test temperatures

Test temperature, °C	$\sigma_{t.BM}$, MPa	$\sigma_{t.WJ}$, MPa	K_{str}
20	570	490	0.85
1200	189	144	0.76

Notes. 1. Average values of testing four specimens are given. 2. Ultimate tensile strength was tested on plane specimens, Figure 10. 3. Strength factor — $K_{str} = \sigma_{t.WJ}/\sigma_{t.BM}$.

The prospect of using welding modes with adjustable distribution of the electron beam power density along the butt edges by rapid oscillation from one extreme position to another is noted [15, 16].

Accordingly, the mode of smoothing passes along the facial side of the preliminary cooled weld: V_w = = 12 mm/s, focusing current — 700 mA, transverse beam scanning with adjustable distribution of its power density along the scanning trajectory A_s = 10 mm, I_w = 30 mA.

The disadvantages of the above design may include the difficulty of manufacturing welded assemblies and the inability to weld the entire assembly within a one evacuation.

The technological process of joining gas valve parts was completed by heat treatment in a furnace for a complete removal of residual welding stresses. Treatment mode: heating rate 25 °C/min = 0.42 °C/s to a temperature of 1150 °C, holding within 60 min, cooling in the furnace.

After welding and heat treatment, X-ray inspection of welded joints was carried out. The X-ray inspection showed a maximum pore diameter of 0.723 mm. The minimum distance between pores is 4.345 mm. Each valve has three welds. After the works on modernization of the design of welded assemblies and optimization of the welding mode, the number and size of pores became non-critical for the gas valve serviceability. X-ray inspection of the welds showed the maximum pore diameter in the range of 0.35–0.43 mm. Their number and sizes do not exceed the requirements of the technical specifications.

The hydraulic tests were also carried out on the welded gas valves. All valves passed the tests successfully. The pressure of 20 MPa was maintained for 2 min without leakage, which meets the requirements of the technical assignment.

After testing the welding technology for the new design of the assembly joint, as well as mechanical tests on industrial specimens, this design and the parameters of EBW welding of gas valve joints of real valve parts were finally selected.

CONCLUSIONS

1. Porosity is a complex problem in fusion welding of molybdenum and its alloys because of the already existing inner defects, first of all related to the powder metallurgy process. Preheating of the butt with a defocused electron beam leads to an overall volume expansion of the future welding zone and facilitates the removal of surface contaminants from adsorbed gases. The latter can significantly reduce the formation of pores, but does not guarantee their complete elimination.

2. The carried out experiments confirmed that the formation of metallurgical pores in EBW, in addition to the influence of harmful gas impurities, is closely related to the assembly conditions, welding speed and weld cross-sectional shape. Preparing end surface of the welded edges and the accuracy of the butt assembly are essential conditions for producing a high-quality welded joint, especially with a satisfactory combination of strength and ductility.

3. The results of the analysis of the mechanical properties and structural state of the welded joints confirmed the correct choice of welding mode parameters with minimum values of the input energy and adjustable distribution of power density of the electron beam scanning trajectory. The use of this mode made it possible to reduce the grain size and a number of voids in the melting zone. This shortens the length of the heat-affected zone, reduces the size of crystallites, and changes the crystallization pattern of the weld metal, which has a favourable effect on the mechanical properties of welded joints, and especially on the low-temperature ductility.

4. To obtain the required quality of welds, changes were made to the design of the gas valve welded joints. A series of welding experiments on the joints of gas valve parts made it possible to modernize the design of welded assemblies using flanging of welded edges, which allowed producing serviceable circumferential welded joints.

REFERENCES

1. Trefilov, V.I., Milman, Yu.V., Firstov, S.A. (1975) *Physical basis of the strength of refractory metals.* Kyiv, Naukova Dumka [in Russian].
2. Platte, W.N. (1956) Influence of oxygen on soundness and ductility of molybdenum weld. *Weld. J.,* 35(**8**), 369–381.
3. Platte, W.N. (1957) Effects of nitrogen on the soundness and ductility of welds in molybdenum *Weld. J.,* 36(**6),** 301–306.
4. Gurevich, S.M. (1975) *Welding of chemically active and refractory metals and alloys.* Kyiv, Naukova Dumka [in Russian].
5. Miao-Xia Xie, Yan-Xin Li, Xiang-Tao Shang et al. (2019) Effect of heat input on porosity defects in a fiber laser welded socket-Joint made of powder metallurgy molybdenum alloy. *Materials,* **12**, 1433. DOI: https://doi.org/10.3390/

ma12091433 https://www.semanticscholar.org/paper/Effect-of-Heat-Input-on-Porosity-Defects-in-a-Fiber-Xie-Li/ff3980832c812389e46ff4ffb4fe22d56e40a494
6. Zhang, L.J., Liu, J.Z., Pei, J.Y. et al. (2019) Effects of power modulation, multipass remelting and Zr addition upon porosity defects in laser seal welding of end plug to thin-walled molybdenum alloy. *J. Manuf. Process.,* **41**, 197–207. DOI: https://doi.org/10.1007/s00170-020-06482-5
7. Xie, M.X., Li, Y.X., Shang, X.T. et al. (2019) Microstructure and mechanical properties of a fiber welded socket-joint made of powder metallurgy molybdenum alloy. *Metals*, **9**, 640. DOI: https://doi.org/10.3390/met9060640
8. Zhang, L.L., Zhang, L.J., Long, J. et al. (2019) Enhanced mechanical performance of fusion zone in laser beam welding joint of molybdenum alloy due to solid carburizing. *Mater. Des*., **181**, 107957. DOI: https://doi.org/10.1016/j.matdes.2019.107957
9. Zhang, L.L., Zhang, L.J., Long, J. et al. (2019) Effects of titanium on grain boundary strength in molybdenum laser weld bead and formation and strengthening mechanisms of brazing layer. *Mater. Des.,* **169**, 107681. https://www.sciencedirect.com/science/article/pii/S0264127519301182 https://doi.org/10.1016/j.matdes.2019.107681
10. Mushegyan, V.O. (2009) Electron beam melting of reduced molybdenum concentrate. *Advances in Electrometallurgy,* **4**, 225–228.
11. Krajnikov, A.V., Morito, F., Slyunyaev, V.N. (1997) Impurity-induced embrittlement of heat-affected zone in welded Mo-based alloys. *Inter. J. of Refractory Metals and Hard Materials,* 15(**5–6**), 325–339. DOI: https://doi.org/10.1016/S0263-4368(97)87507-5
12. Stütz, M., Oliveira, D., Rüttinger, M. et al. (2016) Electron beam welding of TZM sheets. *Mater. Sci. Forum*, **879**, 1865–1869. DOI: https://doi.org/10.4028/www.scientific.net/MSF.879.1865
13. Korneev, N.I., Pevzner, S.B., Razuvaev, E.I., Skugarev, I.G. (1967) *Pressure processing of refractory metals and alloys*. Moscow, Metallurgiya [in Russian].
14. *Wang* Jiteng, Wang Juan, Li Yajiang and Zheng Deshuang (2014) Progress of research on welding for molybdenum alloys. *High Temp. Mater. Proc.* 33(**3**), 193–200. DOI: https://doi.org/10.1515/htmp-2013-0037
15. https://www.researchgate.net/publication/272570992_Progress_of_Research_on_Welding_for_Molybdenum_Alloys14
16. Skryabinskyi, V.V., Nesterenkov, V.M., Rusynyk, M.O. (2020) Electron beam welding with programming of beam power density distribution. *The Paton Welding J.,* **1**, 49–53. DOI: https://doi.org/10.37434/tpwj2020.01.07
17. Kovbasenko, S.N., Yakubovsky, V.V., Ivashchenko, G.A. et al. (1987) *Method of electron beam welding of high-strength steels*. USSR Cert. 1355411, Int. Cl. 3 V23K 15/00. PWI [in Russian].

ORCID
V.I. Zagornikov: 0000-0003-0456-173X,
V.M. Nesterenkov: 0000-0002-7973-1986,
K.S. Khripko: 0000-0002-4893-5441

CONFLICT OF INTEREST
The Authors declare no conflict of interest

CORRESPONDING AUTHOR
V.I. Zagornikov
E.O. Paton Electric Welding Institute of the NASU
11 Kazymyr Malevych Str., 03150, Kyiv, Ukraine.
E-mail: zagornikov@technobeam.com.ua

SUGGESTED CITATION
V.I. Zagornikov, V.M. Nesterenkov, K.S. Khripko, O.N. Ignatusha (2025) Electron beam welding of gas valve elements from Mo–Ti–Zr alloy. *The Paton Welding J*., **4**, 27–36.
DOI: https://doi.org/10.37434/tpwj2025.04.05

JOURNAL HOME PAGE
https://patonpublishinghouse.com/eng/journals/tpwj

Received: 20.06.2024
Received in revised form: 25.10.2024
Accepted: 09.05.2025

DOI: https://doi.org/10.37434/tpwj2025.04.06

TECHNOLOGICAL STRENGTH OF 25KhN3MFA STEEL JOINTS IN SUBMERGED ARC WELDING

A.K. Tsaryuk, V.Yu. Skulskyi, V.P. Yelagin, I.G. Osipenko

E.O. Paton Electric Welding Institute of the NASU
11 Kazymyr Malevych Str., 03150, Kyiv, Ukraine

ABSTRACT

Weldability of 25KhN3MFA steel was studied and requirements for the possibility of its application in manufacture of welded structures in heavy mechanical engineering were established. Investigations of weldability of 25KhN3MFA steel showed that hot and cold cracks form during welding of this steel. To prevent cold cracking in the welded joints, welding should be performed with preheating and interpass heating up to 250–300 °C and mandatory post-weld tempering at 570 °C. Hot cracks form in welding the root layer of the weld metal, which is related to a significant fraction of the base metal (> 50 %) at mixing with the deposited metal. To enable manufacturing welded structures from this steel, it is necessary to use only automatic narrow-gap submerged arc welding and to remove the root layer from the inner side of a welded joint. When it is impossible to remove the root weld, welded structures from 25KhN3MFA steel are not allowed for operation.

KEYWORDS: complex-alloyed steels, narrow-gap submerged arc welding, weldability, cold cracks, hot cracks, preheating and interpass heating, structure

INTRODUCTION

For the manufacture of large-sized thick-walled structures in heavy engineering, complex-alloy Cr–Ni–Mo body steels of 20KhNMFA, 20KhN3MA, 25KhN3MFA type, etc. are used [1]. These steels have the required ductility and toughness at high values of strength after appropriate heat treatment. However, their susceptibility to hardening and a high level of mechanical properties cause a number of difficulties in their welding. This primarily concerns the formation of hot and cold cracks and the production of equally strength welded joints [2]. To solve this problem, it is necessary not only to correctly set the thermal mode of welding and select welding consumables, but also to choose the correct welding method that ensures the quality of welded joints. At manufacturing of the first hydraulic cylinder bodies of 20KhN3MA steel for presses with a capacity of 30 thou t at PJSC NKMZ (Kramatorsk), electroslag welding (ESW) was the main welding method. However, the cylinders produced using ESW were not reliable enough. During operation under variable load conditions, cracks formed in the welded joints, which caused fracturing of the hydraulic cylinders. The nature of these cracks is largely determined by the specifics of the ESW process. The causes of defects and disadvantages of ESW of complex-alloyed steels were studied in [3–5].

Studies of full-scale models of hydraulic press cylinder bodies made by ESW and narrow-gap submerged arc welding of 20KhN3MA steel have shown that the most challenging welding method is automatic narrow-gap submerged arc welding. This method [6, 7] ensures a minimal penetration of the welded edges and dilution of the weld metal with the base metal, a narrow heat-affected zone, homogeneity of chemical composition and mechanical properties along the height of the edge preparation, a limited volume of deposited weld metal at its fine-grained structure and minimal residual stresses and strains. In addition, unlike ESW, in narrow-gap submerged arc welding, a single high tempering provides a sufficiently complete reduction of residual stresses and improves the structure and properties of welded joints. At the same time, high-temperature heat treatment is required after ESW, and for complex-alloyed steels, in several stages [6].

Thus, narrow-gap submerged arc welding of massive thick-walled products made of complex-alloyed steels not only ensures high quality welded joints with high process efficiency, but also is one of the reserves of energy saving, which is very important at the present time.

For the manufacture of hydraulic cylinders for pressing equipment, it is necessary to use large-sized cylindrical forged billets of thick metal (≥ 500 mm thick) made of high-strength steels welded with girth welds. In this case, 25KhN3MFA steel can be considered a promising option, as a high carbon (0.25 %) and nickel (more than 3.5 %) content ensures a sufficient hardenability throughout the entire thickness, which contributes to the stability of the strength values and service properties of thick metal. However, information on the technological strength of welded joints of this steel is very limited.

Copyright © The Author(s)

Table 1. Chemical composition of the studied steel and metal deposited using the applied welding wire, wt.%

Steel/wire grade	C	Si	Mn	Cr	Ni	Mo	V	S	P
								Not more than	
Steel									
25KhN3MFA TU 108.11.917–87	0.20–0.25	0.17–0.37	0.20–0.50	1.40–1.80	3.00–3.75	0.30–0.50	0.08–0.15	0.020	0.020
25KhN3MFA	0.25	0.26	0.36	1.60	3.50	0.33	0.15	0.020	0.020
Wire									
Sv-08KhN2GMYu GOST 2246–70	0.06–0.11	0.25–0.55	1.00–1.40	0.70–1.10	2.00–2.50	0.40–0.65	–	0.030	0.030
Sv-08KhN2GMYu	0.11	0.31	0.95	0.80	2.00	0.60	–	0.02	0.025

THE AIM

of this study was to investigate the weldability of 25KhN3MFA steel and determine the possibility of its using for critical welded structures in heavy engineering.

MATERIALS AND METHODS FOR EXPERIMENTS AND RESEARCH

The chemical composition of 25KhN3MFA steel is shown in Table 1. To produce welded joints, a combination of Sv-08KhN2GMYu wire (Table 1) and AN-17 flux [8] was used, which finds its application in power engineering for the manufacture of products from low-alloy steels.

The regularities of forming the structure of 25KhN3MFA steel depending on the thermal conditions of welding were studied using the experimentally obtained continuous cooling transformation (CCT) diagram [9]. To model the corresponding structural changes and simulate the thermal cycles of welding, a high-speed dilatometer of the PWI design was used. In the experiments, the special test specimens were heated to a temperature of 1300–1350 °C, followed by cooling in accordance with the thermal cycles of manual welding, automatic submerged arc welding (with and without preheating), electroslag welding, and welding with significant heat removal. The cooling time was counted down from the A_{C3} temperature determined in advance using a Chevenard dilatometer. After the specimens had cooled completely, metallographic analysis and hardness measurements were performed.

Microstructural examinations were performed in the Neophot-32 light microscope equipped with an Olympus P-5060 optical module with computer-controlled image capture. The microstructure in polished sections was revealed by electrolytic etching in a 10 % aqueous (distilled water) solution of chromic acid at the following conditions: voltage 12–15 V, etching time 10–15 s; in the process of preparing microsections, the etched surfaces were repolished on the cloth with the application of powdered chromium oxide. A 30 % solution of iron chloride ($FeCl_3$) was used to etch the macrosections of welded joints. The Vickers hardness was measured using a TP-5 hardness tester at a load of 10 kg.

For a qualitative assessment of the susceptibility of welded joints to cracking, butt joints of the type of technological samples of the Lehigh University ("L" sample) [10] with a modified edge configuration - from U- to X-shaped were used (Figure 1). The sample design elements were corrected to enable submerged arc welding, since the original "L" sample was designed for manual arc welding. The tests were carried out at different preheating temperatures, but under constant welding conditions: 2.0 mm diameter wire, one-sided welding, I_w = 320–340 A, U_a = 36–38 V, V_w = 18 m/h. The cooling rate was set by the preheating temperature in the range of 20–300 °C. For each preheating temperature, 3 specimens were welded.

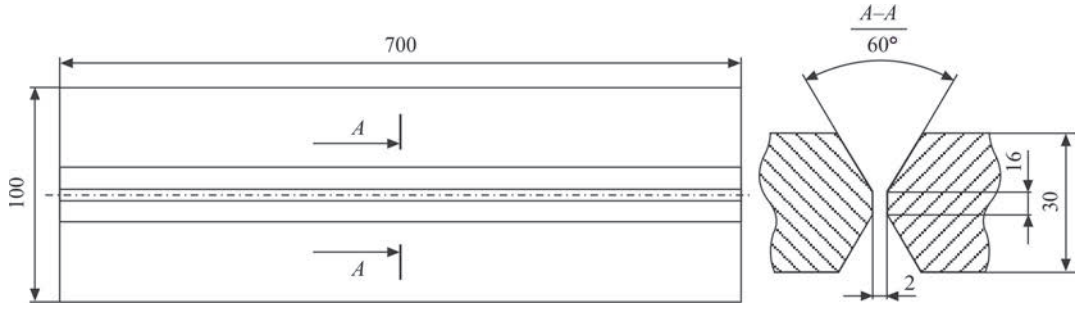

Figure 1. Technological sample

The preheating temperature sufficient to prevent cold cracking was estimated based on the analysis of the constructed thermokinetic diagram of austenite transformation.

RESEARCH RESULTS AND THEIR DISCUSSION

Typically, the weldability of hardening steels before welding is assessed by analysing their response to the thermal deformation cycle of welding and the nature of the formed phases. Such regularities are described by the results of dilatometric studies. Thus, Figure 2 shows the CCT diagram of 25KhN3MFA steel, constructed at cooling rates in the range of 600–500 °C ($w_{6/5}$) within 0.3–100 °C/s.

In the initial state, the microstructure of the tempered steel consists mainly of sorbite (Figure 3, *a*) with a hardness of *HV* 246. When heating to the austenitic state and cooled within the specified range of cooling rates, the phase transformation can occur

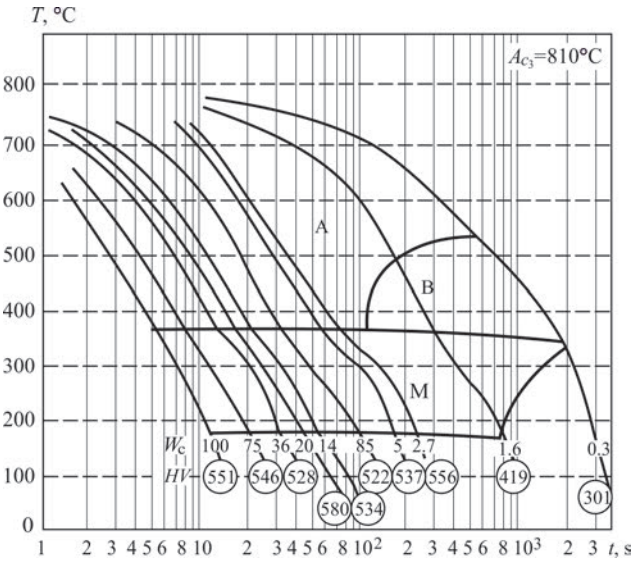

Figure 2. CCT diagram of 25KhN3MFA steel

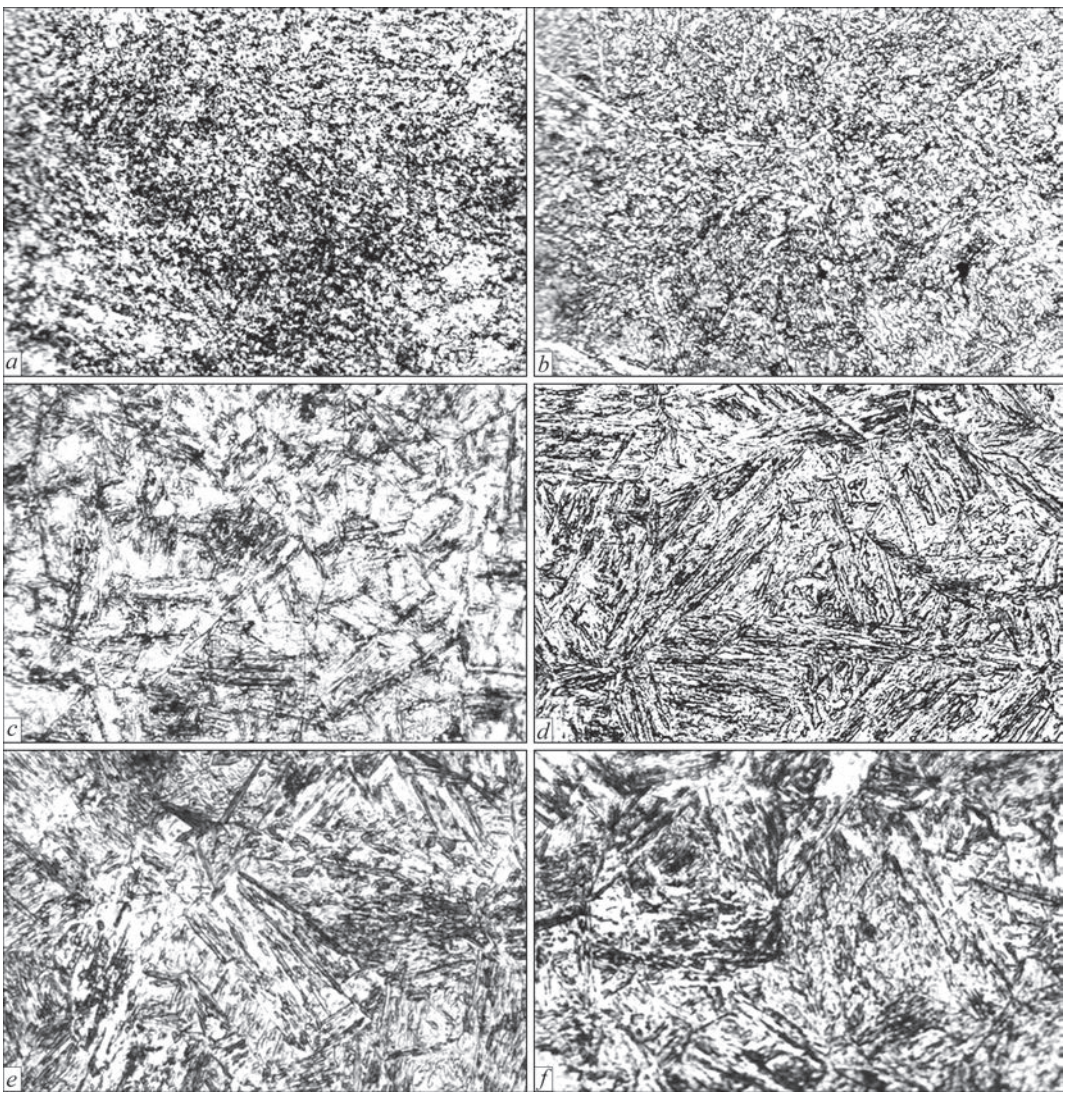

Figure 3. Microstructure of 25KhN3MFA steel after modeling different thermal cycles: *a* — initial state; *b* — $w_{6/5}$ = 0.3 °C/s; *c* — 1.6; *d* — 2.7; *e* — 20; *f* — 100 (×300)

in the bainitic and martensitic regions. No ferrite or pearlite transformation was observed.

At a cooling rate of 0.3 °C/s, a predominantly single-phase bainitic transformation occurs with the formation of granular bainite (Figure 3, *b*). With an increase in the cooling rate from 0.3 to ~2.7 °C/s, the transformation takes place both in the bainitic and martensitic regions and is accompanied by an increase in hardness from *HV* 419 to 556. The structure typical of this range, obtained at $w_{6/5}$ = 1.6 °C, is shown in Figure 3, *c*: the structural components are lamellar bainite and martensite. At $w_{6/5} \geq 2.7$ °C/s, only martensitic transformation occurs with the formation of acicular martensite (Figure 3, *d–i*); the hardness level remains high in the entire range of applied cooling rates ($w_{6/5}$ = 2.7–100 °C/s) and is approximately *HV* 520–580.

An approximate estimate of the steel susceptibility to cold cracking during welding can be performed based on the results of studying the temperature of end of martensitic transformation at different cooling rates in terms of hardness level, as well as the value of carbon equivalent C_E determined with regard to chemical composition. For example, in this case, the IIW expression can be used [11], developed for low-alloy steels with alloying limits that are close to those of the studied steel:

$$C_E = C + \frac{Mn}{6} + \frac{Cr + Mo + V}{5} + \frac{Cu + Ni}{15}, \%.$$

It is assumed that if C_E is higher than 0.40 %, there is a risk of cold cracking. For 25KhN3MFA steel with the actual composition given in Table 1, the calculation gives C_E = 0.97 %, which indicates the probability of crack formation in welded joints. However, this index has a drawback, as it does not take into account the behaviour of steel during welding [11]. It is also generally accepted that steel is prone to cold cracking when martensitic transformation ends at temperatures below 300 °C and the hardness of the transformation products exceeds *HV* 350–360 [12–14].

The analysis of the thermokinetic diagram of the transformation of austenite in 25KhN3MFA steel shows that at cooling rates $w_{6/5}$ = 1.6–100 °C/s, the end temperature of the martensitic transformation is in the range of 170–180 °C. Only at $w_{6/5}$ = 0.3 °C/s, at which partial martensite formation was still observed, the end temperature of martensitic transformation grew to 320 °C, and the hardness of the transformation products decreased to *HV* 300.

In real welding, the cooling rate of the welded joint metal may be slightly higher than the minimum rate obtained in dilatometric experiments. The approximate cooling rate can be estimated using analytical equations from the theory of welding thermal processes; to calculate the instantaneous cooling rate, the equation of the following type was used [15]:

$$w = 2\pi\lambda[(T-T_0)^2/(q/v)],$$

where w is the cooling rate when the bead is deposited on the surface of a massive body (the calculation scheme is chosen taking into account the probable heat dissipation during welding of a thick-walled product); λ is the thermal conductivity coefficient; T and T_0 are the temperature for which w is calculated and the initial temperature of the steel; v is the welding speed; $q = \eta IU$ is the thermal power of the welding arc, which is determined by the product of the effective heating efficiency of a part by the arc (η), welding current (I) and voltage (U).

For the calculations, the values of η = 0.9 (for submerged arc welding) and $\lambda \approx 30$ W/(m·°C) (according to the data for 30KhN2MFA steel, which is similar in alloying) were chosen. For a temperature of T = 550 °C, which is an average in the range of 600–500 °C, and an initial heating temperature of T_0 = 200, 300 and 350 °C, the following values of the average cooling rate $w_{6/5}$ were obtained:

- 10.5 °C/s at preheating up to 200 °C;
- 5.4 °C/s at preheating up to 300 °C;
- 3.4 °C/s at preheating up to 350 °C.

At welding without preheating — $w_{6/5}$ = 24.07 °C/s.

Therefore, under submerged arc welding conditions, martensitic transformation will occur in welded joints in the range from $M_s \approx 380$ °C to $M_f \approx$ 170–180 °C with the resulting steel hardness significantly exceeding the approximate critical level of *HV* 350.

Thus, a preliminary assessment of the weldability of 25KhN3MFA steel based on the value of the calculated carbon equivalent and the analysis of austenite transformation regularities indicates a high susceptibility of its welded joints to cold crack formation. To prevent cracking in all types of mechanized welding, preheating and accompanying heating is required.

Typically, welding of complex-alloyed power engineering steels is supposed to be carried out with preheating up to 350 °C and higher. However, both preheating and a high temperature of this operation complicate the technological process. In addition, an excessive preheating temperature can lead to an increase in residual stresses and cause microstructure deterioration. From a physical and metallurgical point of view, during welding of steels with martensitic transformation, it is advisable to preheat and maintain the interpass temperature within the M_s–M_f range, giving preference to temperatures close to M_f. This approach enables martensitic transformation in the

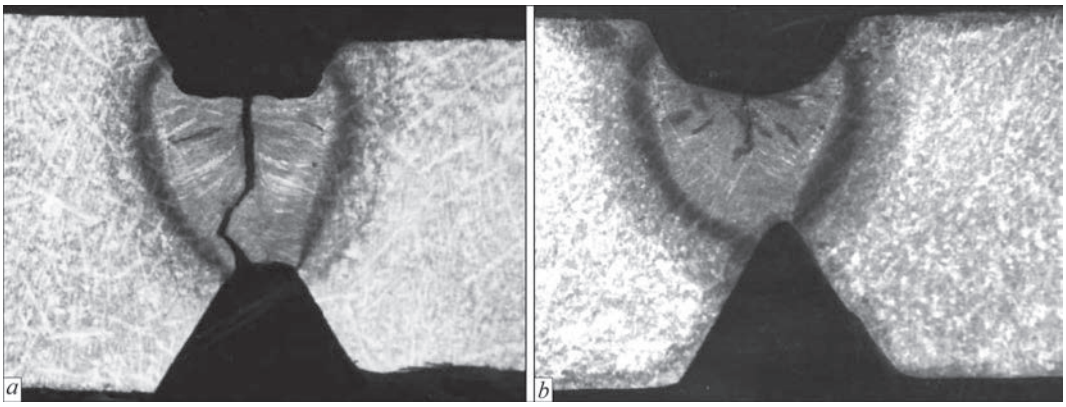

Figure 4. Solidification cracks in welds when welding samples of 25KhN3MFA steel using Sv-08KhN2GMYu wire: *a* — with a diameter of 3 mm; *b* — 2 mm

area of the last produced pass, and repeated welding heating, activating diffusion processes, causes partial martensite decomposition — tempering of hardened layers, as well as a decrease in the concentration of diffused hydrogen in them; the result is an increase in resistance to delayered fracture [16]. Limiting the preheating level also simplifies the production process itself.

It is advisable to clarify the preheating temperature by welding technological samples. Preliminary tests as well as practical experience have shown that cracks in the welded joints of 25KhN3MFA steel were mainly observed in the weld metal zone. For this reason, "L" type samples from the Lehigh University were used, the configuration of which facilitates the initiation of cracks namely in the welds.

It was experimentally established that in all cases of welding specimens without preheating and with preheating to 150, 200, 250 and 300 °C, cracks occurred in the weld zone. The cracks were detected in the hot metal immediately after the slag crust was removed.

Based on practical experience, it is known that preheating at the level of 250–300 °C is usually sufficient to eliminate cold cracks in the joints of hardening power mechanical engineering steels. In addition, their formation occurs after the end of welding and cooling of the metal, and in some cases it occurs within several tens of hours. In this case, cracks formed in the weld metal during welding and under the condition of preheating, which eliminates the probability of namely cold cracking. Therefore, it can be assumed that cracks in the welds formed during welding with preheating do not belong to cold cracks.

After a full cycle of research, it was found that cracks on 25KhN3MFA steel samples are hot cracks formed during solidification of the weld metal.

The formation of such cracks in the welds occurred under different experimental conditions. Changing the wire diameter from 2 to 3 mm in order to influence the shape of the pool and orientation of the solidification elements did not lead to positive results (Figure 4). Considering the complex alloying of the used wire, welding was performed using low-carbon Sv-08GA wire. Such a measure also did not prevent the appearance of solidification cracks. Cracks were also formed when beads were deposited on the surface of 25KhN3MFA steel, both in reverse and direct polarity (Figure 5).

Analysis of the chemical composition of the weld metal welded using Sv-08KhN2GMYu wire showed an increased carbon content (0.17–0.18 %) near the crack. The average composition of sulphur and phosphorus was within acceptable limits (S — 0.025 %, P — 0.020 %). However, metallographic examinations using local electron probe mictroanalysis re-

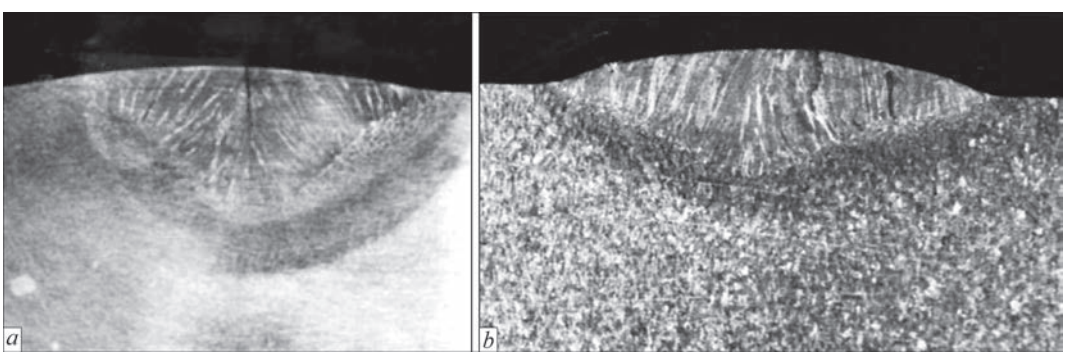

Figure 5. Solidification cracks when depositing bead on the surface of 25KhN3MFA steel using Sv-08GA wire with a diameter of 3 mm: *a* — reverse polarity; *b* — direct polarity

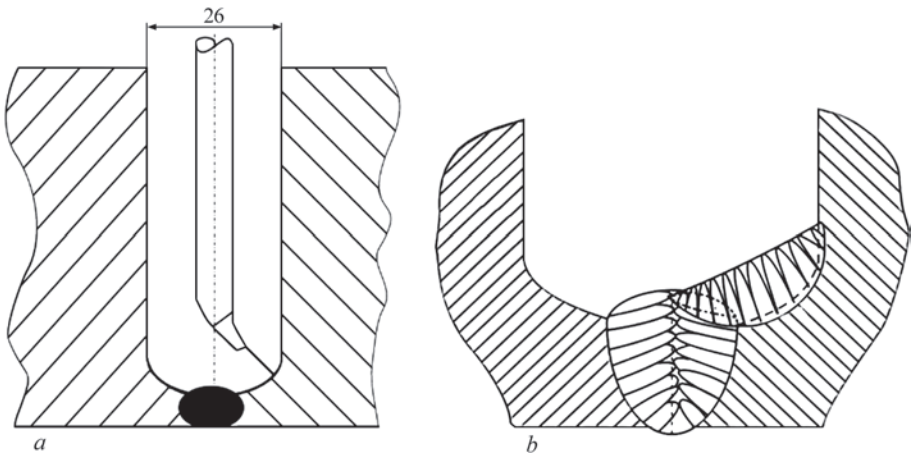

Figure 6. Layout schemes of the mouthpiece in a narrow groove (*a*) and the nature of beads solidification (*b*)

vealed segregation of sulphur and phosphorus in the area of crack initiation and propagation, which can be considered one of the factors that may contribute to the formation of such defects.

Also, an increased susceptibility of welded joints of 25KhN3MFA steel to hot crack formation can be associated with the high content of carbon and nickel in the base metal [13], which, for example, is reflected by the HCS index (Hot Cracking Susceptibility) [12]:

$$HCS = \frac{C\left(S + P + \frac{Si}{25} + \frac{Ni}{100}\right)\cdot 10^3}{3\,Mn + Cr + Mo + V}.$$

Hot cracks do not form in a welded joint if HCS < 4.0; in the case of large-thick high-strength steels, hot cracks will not form if HCS < 1.6–2.0. In our case, for 25KhN3MFA steel, HCS = 6.7, which indicates a high susceptibility of weld metal with such chemical composition to form solidification cracks.

During narrow-gap submerged arc welding of 25KhN3MFA steel, hot cracks formed in the first root layer when the arc was located at a right angle to the surface of the metal being welded. In this process, the fraction of the base metal at stirring with the deposited metal was ~50 %. At further filling of the gap with the arc orientation at an acute angle towards the edges, the penetration depth decreased (Figure 6), the fraction of the base metal also decreased, but it did not exceed the maximum level of 30 %. Under these conditions, except for the root layer, no cracks formed in the weld.

For comparison, the chemical composition of the metal of the root and filling passes was evaluated. The content of each of E_{WMi} elements in the weld was calculated as a total amount of this element transferred from the base metal and filler wire, according to the expression:

$$E_{WMi} = \Sigma(D_{PM}E_{PMi} + D_{WR}E_{WRi}),$$

where D_{PM}, D_{WR} are fractions of the base metal (*PM*) and welding wire (*WR*) at stirring in the weld (for the root pass D_{PM} and D_{WR} are assumed to be equal to 50 and 50 % and for the filling passes — 30 and 70 %); E_{PMi}, E_{WRi} are concentrations of the *i*-th element in the base metal and in the welding wire.

The approximate composition of different areas of the weld metal and the corresponding values of HCS index are shown in Table 2. For the root pass, the rounded value of HCS is ~3.8 (actually 3.778), exceeding the corresponding value for the filling passes, which was calculated to be 3. However, it should be noted that HCS ≤ 3 % should be considered for the filling passes, since for these conditions, as noted above, $D_{PM} \leq 30$ %.

As is seen from the calculation results, in both cases, HCS values were less than the critical level of HCS = 4, but cracks still occurred in the root pass. In addition, this value for the filling passes was higher than the critical value for a thick-walled joint of increased hardness (HCS = 2), although no cracks formed in the metal of the filling passes. Thus, the obtained research data indicate that there is no unambiguous explanation for the cause of solidification crack formation, which, for example, is seen from the inconsistency of welding results and evaluation of the technological strength according to HCS criterion. In general, solidification crack formation has a complex mechanism, in which both metallurgical and force factors are simultaneously manifested [13, 15]. Depending on the chemical composition, the segregation

Table 2. Results of calculated chemical composition of root and filling passes and HCS indices

Weld zones	C	Si	Mn	Cr	Ni	Mo	V	S	P	HCS
Root	0.180	0.285	0.655	1.20	2.75	0.465	0.075	0.020	0.022	3.8
Filling pass	0.152	0.295	0.773	1.04	2.45	0.519	0.045	0.020	0.021	3.022

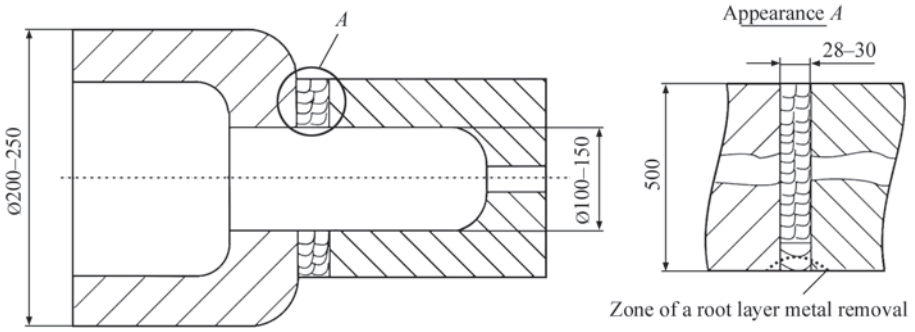

Figure 7. Scheme of a welded hydraulic press cylinder

of the most harmful impurities — S and P, or C and Ni can have a prevailed effect; in low-alloy welds which are free from impurities, the crack formation is dominated by the segregation of the latter two elements [13, 17]. According to [17], in iron-carbon welds, low technological strength was observed at approximately 0.1 % C and at C > 0.17 %. In Fe-Ni type welds, an increase in crack susceptibility occurred at Ni > 2–3 %. The role of C and Ni in the mechanism of crack formation is also associated with their influence on the nature of primary solidification [17]. The study of the combined effect of C and Ni using the concentration index Ni_{eq} (Ni_{eq} = Ni + *k*C, where *k* is a coefficient depending on the C content) showed that a significant increase in the susceptibility to solidification cracks occurred at Ni_{eq} is greater than ~3.4 %. Under this condition, the primary solidification with the formation of δ-phase (according to the L → δ scheme) transferred to the solidification of δ + γ through the peritectic reaction (L → δ + (L + δ = γ) → δ + γ). A decrease in resistance to crack formation may be a consequence of:

a) increased liquation of S and P at a decrease in their solubility in the γ-phase, in which Ni and C were also more soluble;

b) an additional (to the overall thermal reduction) increase in the level of microdeformations near the solidification boundary as a result of volumetric changes caused by the formation of the γ-phase at a two-phase solidification of δ + γ.

In the considered case of welding 25KhN3MFA steel, the weld metal, depending on the degree of stirring the base and weld metals may have a resulting C and Ni content that increases its susceptibility to solidification cracks. For example, when making root passes due to a significant fraction of the base metal (up to 50 %), the weld is enriched with carbon (up to 0.18 %). This level of carbon in the weld metal contributes to the formation of hot cracks. The segregation of harmful impurities (S, P) at their normal admissible content in steel is also an important metallurgical factor in reducing technological strength. Nickel creates an additional effect, enhancing the liquation of these elements and contributing to the formation of crack initiation sites. The negative impact of a significant dilution of the deposited metal with the base metal is also shown on the example of beads deposited on steel using Sv-08GA wire, when the fraction of the base metal was 60–80 %. In turn, a reduction in the HCS index for the filling passes relative to the root passes can contribute to an increase in crack resistance. In addition, the shape of the weld cross-section and the corresponding directions of crystallite growth during weld pool solidification are also important factors in the formation and prevention of hot cracks [13, 15]. The root pass is characterized by deep penetration relative to the width of the weld pool and trancrystalline (counter) growth of solidification elements from the pool walls. The formation of liquid enriched with impurities in the axial zone at the joining of crystallites in this pool shape contributes to the appearance of cracks under the influence of welding deformations (Figure 6).

At a wider and shallower shape of the pool with the crystallite growth directed towards the zenith and displacement of the low-melting liquid into the upper

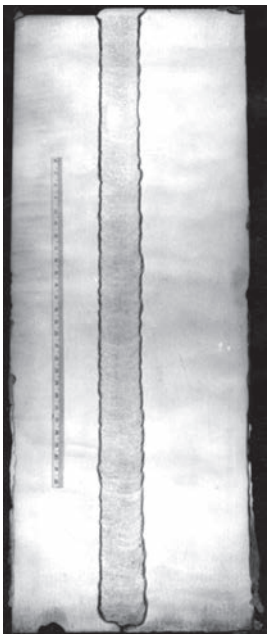

Figure 8. Macrosection of a butt joint with a weld depth of 500 mm

Table 3. Mechanical properties of welded joint of 25KhN3MFA steel, welded using Sv-08KhN2GMYu wire under AN-17 flux in the state after high tempering

Weld metal					Welded joint	
σ_t, MPa	$\sigma_{0.2}$, MPa	δ, %	ψ, %	*KCU*, J/cm^2	σ_t, MPa*	*KCU*, J/cm^{2**}
Requirements for properties of welded joints						
≥ 600	≥ 500	≥ 12	≥ 40	≥ 50	≥ 600	≥ 50
Test results						
786	583	16.6	55.6	115	633	72.0
783	575	16.3	51.0	137	735	62.0
788	583	16.6	55.6	122	705	115.0
785***	580***	16.5***	54.0***	124***	691***	83.0***

*Fracture over HAZ.
**Notch along the fusion line.
***Average value for three tests.

part, the resistance to hot cracking grows. Such solidification is characteristic of filling passes. Practicing the technology on models of industrial products confirmed the existence of the problem of hot cracking only for the root passes.

For the industrial production of the hydraulic cylinder body from 25KhN3MFA steel, it was agreed to use narrow-gap submerged arc welding, which is characterized by high efficiency and generally high quality of thick-walled joints (Figures 7, 8). However, considering that reaching a high quality of the root passes is problematic, after the groove had been completely filled, it was mandatory to remove the root layer of the weld metal by mechanical method using machine-tool (Figure 7).

To temper the hardening structures in the joint zone, maximize the removal of residual stresses and improve the ductility and toughness of the metal, a welded product is subjected to mandatory high tempering. Taking into account the existing recommendations and conducted tests, the tempering mode at a temperature of 570 °C for 30 h was selected, which provides the necessary mechanical properties of welded joints (Table 3). At the manufacturing stage and after heat treatment, it is recommended to carefully apply all methods of non-destructive quality testing.

The developed technological process of welding and heat treatment of powerful hydraulic cylinder bodies was introduced in the production of equipment intended for the manufacture of damaged elements of civilian structures and parts of weapons and equipment for the Armed Forces of Ukraine by press stamping, in particular, assemblies of long-range guns, cruise and ballistic missiles, which is relevant for the military-industrial complex of Ukraine.

CONCLUSIONS

1. It is shown that under conditions of automatic submerged arc welding of 25KhN3MFA steel using a combination of AN-17 flux and Sv-08KhN2GMYu wire, the metal in the joint zone undergoes hardening with the formation of a predominantly martensitic structure with a hardness of up to *HV* 520–580, which causes the risk of cold cracking. The elimination of cold cracks is achieved by preliminary/accompanying heating to 250–300 °C.

2. During laboratory tests and narrow-gap submerged arc welding of industrial mock-ups, it was established that for the manufacture of thick-walled products from 25KhN3MFA steel, the main problem is the formation of solidification cracks when producing root passes; at further filling of the groove, hot cracks were not observed.

3. Taking into account the results of experiments and modern theoretical provisions, it was assumed that in the considered case, the occurrence of solidification cracks has a complex nature. The main factors may include the enrichment of the weld metal with C and Ni due to an increase in the fraction of the base metal in the pool melt to 50 %, which is typical for root passes, the corresponding intensification of the processes of segregation of C, S and P with the formation of low-melting fracture sites, as well as an unfavourable shape of the pool with the transcrystalline type of growth of solidification elements. Filling passes form when the fraction of the base metal in the weld is reduced to 30 % or lower, as well as with a pool shape that is favourable for the displacement of low-melting constituent elements to its surface during solidification, which in combination causes the absence of hot cracks.

4. For the industrial manufacture of critical products from 25KhN3MFA steel with a wall thickness of up to 500 mm, the technology of automatic narrow-gap submerged arc welding was introduced, which involves the removal of a metal layer with a root pass using a machine-tool after welding the joint.

The final operation is high tempering at a temperature of 570 °C.

REFERENCES

1. Bashnin, Yu.A., Tsurkov, V.N., Korovin, V.N. (1985) *Heat treatment of large-sized products and semi-products at metallurgical works.* Moscow, Metallurgiya [in Russian].
2. Paton, B.E. (1974) *Technology of electric fusion welding of metals and alloys.* Moscow, Mashinostroenie [in Russian].
3. Makara, A.M., Kovalev, Yu.Ya., Novikov, I.V. (1972) Tears in near-weld zone during electroslag welding of structural steels. *Avtomaticheskaya Svarka,* **5**, 1–5 [in Russian].
4. Eregin, L.P., Malaj, A.E. (1978) Conditions of formation of near-weld cracks-tears in electroslag welding of chrome-nickel-molybdenum steels. *Svarochnoe Proizvodstvo,* **10**, 26–27 [in Russian].
5. Makara, A.M. (1963) *Investigation of problems of technology and metals science of welding of alloyed structural steels:* Collection. Kyiv, Izd-vo AN Ukr. SSR [in Russian].
6. Kasatkin, B.S., Tsaryuk, A.K., Levenberg, N.E., Pilipenko, N.V. (1984) Technological possibilities of narrow-gap submerged arc welding of medium-alloy thick steels. *Avtomaticheskaya Svarka,* **7**, 41–44 [in Russian].
7. Tsaruk, A.K., Skulsky, V.Yu., Moravetsky, S.I. (2016) Mechanized narrow-gap submerged arc welding of thick-walled cylindrical products. In: *Medovar Memorial — Symposium 7–10 June, Kyiv, Ukraine*, 82–90.
8. Kasatkin, B.S., Kravchenko, N.F., Ivanenko, V.D. et al. (1989) Narrow-gap submerged arc welding of thick-walled cylindrical products. *Avtomaticheskaya Svarka,* **5**, 31–35 [in Russian].
9. Lebedev, Yu.M., Kravchenko, L.P., Danilyuk, N.N. (1978) Procedure of modeling of welding thermodeformational cycles. *Avtomaticheskaya Svarka,* **12**, 31–33 [in Russian].
10. Kihara, H., Suzuki, H., Makamura, H. (1962) Weld cracking test of high strength steel and electrodes. *Welding J.,* **41**, 36–38.
11. (1992) *Steel:* A Handbook for Materials Research and Engineering. Vol. 1: Fundamentals. Springer-Verlag Heidelberg and Verlag Stahleisen m.b.H., Dusseldorf.
12. Hrivnak, I. (1984) *Weldability of steels.* Moscow, Mashinostroenie [in Russian].
13. Lippold, J.C. (2015) *Welding Metallurgy and Weldability*. Wiley & Sons.
14. (2017) *Materials for ultra-supercritical and advanced ultra-supercritical power plants*. Ed. by Augusto Di Gianfrancesco. Elsevier Ltd.
15. Sindo, Kou (2003) *Welding Metallurgy.* Second Ed. Wiley & Sons.
16. Skulsky, V.Yu., Moravetsky, S.I., Nimko, M.A. et al. (2019) Effect of reheating in multipass submerged-arc welding on delayed fracture resistance of rotor steel welded joints. *The Paton Welding J.,* **3**, 11–14. DOI: https://doi.org/10.15407/tpwj2019.03.02
17. Shankar, V., Devletian, J.S. (2005) Solidification cracking in low alloy steel welds. *Sci. and Technol. of Welding and Joining*, 10(**2**), 236–243.

ORCID

A.K. Tsaryuk: 0000-0002-5762-5584,
V.Yu. Skulskyi: 0000-0002-4766-5355,
V.P. Yelagin: 0000-0002-4335-5130,
I.G. Osipenko: 0000-0001-6645-7853

CONFLICT OF INTEREST

The Authors declare no conflict of interest

CORRESPONDING AUTHOR

A.K. Tsaryuk
E.O. Paton Electric Welding Institute of the NASU
11 Kazymyr Malevych Str., 03150, Kyiv, Ukraine.
E-mail: tsaryuk@paton.kiev.ua

SUGGESTED CITATION

A.K. Tsaryuk, V.Yu. Skulskyi, V.P. Yelagin, I.G. Osipenko (2025) Technological strength of 25KhN3MFA steel joints in submerged arc welding. *The Paton Welding J*., **4**, 37–45.
DOI: https://doi.org/10.37434/tpwj2025.04.06

JOURNAL HOME PAGE

https://patonpublishinghouse.com/eng/journals/tpwj

Received: 04.12.2024
Received in revised form: 16.01.2025
Accepted: 08.05.2025

DOI: https://doi.org/10.37434/tpwj2025.04.07

SUBSTANTIATION OF NEW DIAGNOSTIC PARAMETERS OF PIPELINE SYSTEMS EFFICIENCY

I.V. Rybitskyi[1], O.M. Karpash[2], V.Yu. Zapeka[2], P.M. Reiter[1], A.V. Yavorskyi[1], N.I. Chaban[3]

[1]Ivano-Frankivsk National Technical University of Oil and Gas
15 Karpatska Str., 76019, Ivano-Frankivsk, Ukraine
[2]Kharkiv Ivan Kozhedub National University of the Air Force
228 Klochkivska Str., 61045, Kharkiv, Ukraine
[3]King Danylo University
35 Konovaltsia Str., 76018, Ivano-Frankivsk, Ukraine

ABSTRACT

One of the main tasks of technical diagnostics of pipeline systems is to ensure their reliable and at the same time energy-efficient operation. In this work, we have searched for and developed the basis for constructing mathematical models of new informative parameters for diagnosing the technical condition and efficiency of pipeline systems. It is shown that the capacity of a pipeline decreases when it acquires an elliptical cross-sectional configuration. It is substantiated that the presence of small leaks in pipeline systems causes a loss of flow stability in the pipeline, the emergence of turbulent flow zones, which reduces the efficiency of the pipeline.

KEYWORDS: technical diagnostics, informative parameters, energy efficiency, pipeline systems, mathematical model

INTRODUCTION

Technical condition of the pipeline system for transportation of oil, gas and petroleum products, compliance with its operating parameters within the established limits and efficiency of operation of a pipeline system, as a whole, directly affect the uninterrupted and reliable supply of carbohydrates to consumers.

The problem proposed for solution in this work, consists in an attempt to identify new diagnostic parameters, as well as in development of the basis for construction of mathematical models and procedures for evaluation of the influence of changes in these parameters on the technical condition and energy efficiency of pipeline systems. Such parameters, which are proposed to be used, include: geometrical parameters (wall thickness, diameter and cross-sectional shape of the pipeline), physical-chemical parameters of the transported product (viscosity, density, temperature), hydrodynamic parameters (pressure, flow rate, volumetric flow) and parameters associated with defects (leaks, cracks, deformations, corrosion or erosion damage).

Parameters, which change only slightly, while influencing the efficiency of pipeline systems operation, should include: small leaks, change in physical-chemical characteristics of the transported products, as well as a change in the cross-sectional geometry of the pipeline: its ovality or reduction of inner radius as a result of precipitation of heavy impurities and condensate in the pipeline cavity [1].

This kind of defects is determined by experimental methods. However, the methods of mathematical simulation of such phenomena are becoming ever wider applied, in particular, because of the complexity of implementing the hardware methods, which is related to the inaccessibility of the surfaces for implementation of the contact methods of investigation and considerable scope of the required work.

Moreover, one of the main problems of technical diagnostics of pipeline systems is ensuring their reliable and at the same time energy efficient functioning. Thus, searching for new informative parameters of diagnostics of the technical state and efficiency of operation of the pipeline systems with development of the respective mathematical models is an urgent task.

INVESTIGATION PROCEDURE

The problem of technical diagnostics and energy efficiency of pipeline system operation can be reduced to the problem of simulation of hydrocarbon flow in the pipeline with the available changes of its cross-sectional shape, presence of deposits on the pipeline inner surface, product leakage and change in the physical-chemical characteristics of the transported product proper, in order to develop the procedures and identify of the defects, and establish new informative parameters and limits of model application. When studying the technical condition of complex systems, which have been in operation for a long time, in particular, in the problems of their technical diagnostics, there are often cases, where the occurrence of emergency situations is caused by presence of minor disturbances and changes affecting the system [2].

Let us consider the problem of evaluation of the influence of a change in the cross-sectional geometrical characteristics of the pipeline and properties of the trans-

Copyright © The Author(s)

ported substance, on the technical condition and energy efficiency of a pipeline system. In the assumption that the pipe has a circular cross-section, and the fluid (oil or petroleum products) moves under the action of a stable pressure gradient along the pipe, the speed profile is determined by the Poiseuille formula [3, 4]:

$$w = \frac{i}{4\mu}(a^2 - r^2), \tag{1}$$

where w is the longitudinal flow speed of a viscous fluid; μ is the fenid viscosity; a is the radius of the pipe, through which the fluid flows; i is the specific pressure gradient per a unit of pipe length; r is the radial coordinate. Here, the fluid speed profile is the paraboloid of revolution.

The volumetric fluid flow rate calculated by (1) is as follows:

$$Q = \int_0^a w 2\pi r dr = \frac{i\pi a^4}{8\mu}. \tag{2}$$

Here, it should be noted that the volume flow rate significantly depends on pipe radius and is proportional to the fourth power of its radius. Analyzing (1) and (2), we can draw the following conclusions: with the change of pipe radius that may occur during deposition of sediments on its internal wall, as was noted in [1], the volumetric flow rate reacts to it the most. Let a_1 be the design radius of the pipeline, a_2 — its radius after long-term service, $a_1 > a_2$, then in each point $r = r_1$ the speed gradient Δw will be equal to:

$$\Delta w = \frac{i}{4\mu}(a_1^2 - a_2^2). \tag{3}$$

Here, a deficit of the capacity occurs, which can be assessed using (2) as follows:

$$\Delta Q = \frac{i\pi}{8\mu}(a_1^4 - a_2^4). \tag{4}$$

Using (4) transformation, ΔQ value can be presented in the form of:

$$\Delta Q \approx \frac{i\pi}{8\mu} 4R^3 \Delta\delta, \tag{5}$$

where $\Delta\delta$ is the change in the cross-sectional radius.

To compensate for such a deficit of the transported fluid, it is necessary to increase the relative pressure gradient, which can be determined from the following relationship:

$$i_1 = \frac{i(R - 4\Delta\delta)R^3}{(R - \Delta\delta)^4}. \tag{6}$$

It is obvious that $i_1 > i$. Note that increase in the pressure gradient reduces the energy efficiency of the system operation.

Another important moment and possible informative parameter is the transported substance viscosity. While at the initial moment of time the dynamic viscosity of the fluid is equal to μ_1 and at a certain moment of time it rose to the value of μ_2, allowing for (1) and (2), we will have:

$$\Delta w = \frac{i}{4\mu_1}(a^2 - r^2) - \frac{i}{4\mu_2}(a^2 - r^2) = \\ = \frac{i}{4}\frac{\mu_2 - \mu_1}{\mu_2\mu_1}(a^2 - r^2); \tag{7}$$

$$\Delta Q = \frac{i\pi a^4}{8\mu_1} - \frac{i\pi a^4}{8\mu_2} = \frac{i\pi a^4}{8}\frac{\mu_2 - \mu_1}{\mu_2\mu_1}. \tag{8}$$

To compensate for this ambiguity of the product, by analogy with (6), we can derive the value of a certain pressure gradient, required to compensate for the deficit:

$$\frac{i_1\pi a^4}{8\mu_2} = \frac{i\pi a^4}{8\mu_1} - \frac{i\pi a^4}{8}\frac{\mu_2 - \mu_1}{\mu_2\mu_1}; \tag{9}$$

$$\frac{i_1}{\mu_2} = \frac{i}{\mu_1} - i\frac{\mu_2 - \mu_1}{\mu_2\mu_1}; \tag{10}$$

$$\frac{i_1}{\mu_2} = \frac{i(\mu_2 - \mu_2 + \mu_1)}{\mu_2\mu_1} = \frac{i}{\mu_1}. \tag{11}$$

Finally, after carrying out the transformation, we get:

$$i_1 = i\frac{\mu_2}{\mu_1}. \tag{12}$$

It is obvious that $i_1 > i$, as $\mu_2/\mu_1 > 1$. Again, as we can see from the above, increase in the pressure gradient along the pipeline, leads to reduction in energy efficiency of the pipeline system.

Moreover, analyzing equations (1) and (2) and doing some transformations, we can obtain a generalized formula for speed gradient:

$$\Delta w = \frac{a^2 - r^2}{4\mu}\delta i - \frac{i}{4\mu^2}(a^2 - r^2)\delta\mu + \frac{i}{4\mu}2a\delta a, \tag{13}$$

where δa, δi, $\delta\mu$ are the variations of the respective values.

Similarly, we can obtain a generalized equation for capacity deficit:

$$\Delta Q = \frac{\pi a^4}{8\mu}\delta i - \frac{i\pi a^4}{8\mu^2}\delta\mu + \frac{i\pi 4a^3}{8\mu}\delta a, \tag{14}$$

Formulas (13) and (14) allow evaluation of insufficient amount (volume) of hydrocarbon flow in the cases of unambiguous determination of insufficient relative pressure gradient and change in the pipeline cross-sec-

tional geometry as a result of deposition of technological substances on its walls and change in the fluid viscosity.

Cases also often occur, when investigation of the real geometry of pipeline systems reveals that the pipeline cross-section takes on an elliptical shape. This is due to the action of fluid-force factors (bending moment effect during shear, technological defects), which causes additional stresses in the pipeline material, and may lead to failure of its individual segments.

Analyzing the problem of fluid flow in the pipe, having the shape of an ellipse in its cross-section, we can come to the conclusion that formulas (1) and (2) can be written in the following form [3].

For the speed profile:

$$w(y,z) = A\left(1 - \frac{y^2}{a^2} - \frac{z^2}{b^2}\right); \tag{15}$$

$$A = \frac{i}{2\mu}\frac{a^2b^2}{a^2+b^2}. \tag{16}$$

For volumetric flow rate:

$$Q = \iint_G w dy dz = \frac{\pi i}{4\mu}\frac{a^3b^3}{a^2+b^2}, \tag{17}$$

where a (major semi-axis) and b (minor semi-axis) are the constants of the ellipse curve $\frac{y^2}{a^2} + \frac{z^2}{b^2} = 1$, which simulates a deformed cross-section.

Let us consider function:

$$f(x,y) = \frac{x^3y^3}{x^2+y^2}, \tag{18}$$

as the function of two variables, and let us conduct its study for the extremum. From the system of equations (19) we can show that the above function has the following critical points: $x = 0$; $y = 0$; $x = -e$; $x = y$:

$$\begin{cases} \frac{\partial f}{\partial x} = 0 = -\frac{x^3y^3 2x}{(x^2+y^2)^2} + \frac{3x^2y^3}{x^2+y^2} = 0, \\ \frac{\partial f}{\partial y} = 0 = -\frac{x^3y^3 2y}{(x^2+y^2)^2} + \frac{3x^3y^2}{x^2+y^2} = 0. \end{cases} \tag{19}$$

It is obvious that the first three conditions do not meet the physical conditions of the problem. Thus, the function has a separate extremum, which is reached at $x = y$ (x, y, z are the coordinates of the studied pipeline segment: longitudinal, transverse horizontal and transverse vertical coordinates, respectively). This condition means that function (18) in such a case takes on an extreme value. By carrying out the respective mathematical transformations, we can prove that this is the main extremum, i.e. the maximum of the function.

From a practical point of view it means than the pipeline capacity is reduced with its cross-section taking on an elliptical shape, which results in the need to increase the relative pressure gradient and leads to lowering of the pipeline system energy efficiency [5].

The next diagnostic parameter can be derived upon detailed consideration of the viscous fluid flow in pipelines, containing pipe wall defects, in particular through-thickness holes, through which pipeline leakage occurs. In this case, the technical diagnostics problem can be presented in the form of the problem of simulation of a flow with leakage [6].

Investigations of the stability of hydrodynamic processes in the small leak area is important in two respects, influencing the energy efficiency: assessment of the amount of transported hydrocarbon loss; studying the flow structure in case of small leaks of different intensity, in terms of appearance of turbulent flow zones, which may lead to actual reduction in the pipeline effective diameter [7].

Mathematical simulation of the technological fluid flow in the pipeline was performed in case of leaks of different sizes through the pipeline wall. In order to implement it, a system of Navier–Stokes equations is numerically integrated, stability parameters of numerical schemes are studied, informative parameters are selected to determine the zones affected by the leak and the limits of the model application before the flow goes into the turbulent mode are established.

Product flow in the pipelines can be described using a system of Navier–Stokes equation, written in the cylindrical system of coordinates [8]. There is, however, one peculiarity of pipeline systems in terms of their geometry, in particular flow symmetry. The local nature of the small leak zone allows reducing the dimensionality of the problem and, in particular, believing that a two-dimensional flow of viscous fluid is considered in a channel with a wall, in which fluid leakage through the surface is present in the assumption that the flow becomes stationary. This assumption is valid in particular for quasistationary processes, when it is believed that the simulated flow characteristics change only little with time (Figure 1).

In such a case, the system of Navier–Stokes equations is written in a two-dimensional domain as follows:

$$\begin{cases} U\frac{\partial U}{\partial x} + V\frac{\partial U}{\partial y} = -\frac{1}{\rho}\frac{\partial p}{\partial x} + \nu\left(\frac{\partial^2 U}{\partial x^2} + \frac{\partial^2 U}{\partial y^2}\right), \\ U\frac{\partial V}{\partial x} + V\frac{\partial V}{\partial y} = -\frac{1}{\rho}\frac{\partial p}{\partial y} + \nu\left(\frac{\partial^2 V}{\partial x^2} + \frac{\partial^2 V}{\partial y^2}\right), \\ \frac{\partial U}{\partial x} + \frac{\partial V}{\partial y} = 0, \end{cases} \tag{20}$$

where U and V are the components of the speed vector in the rectangular Cartesian system of coordinates; ρ

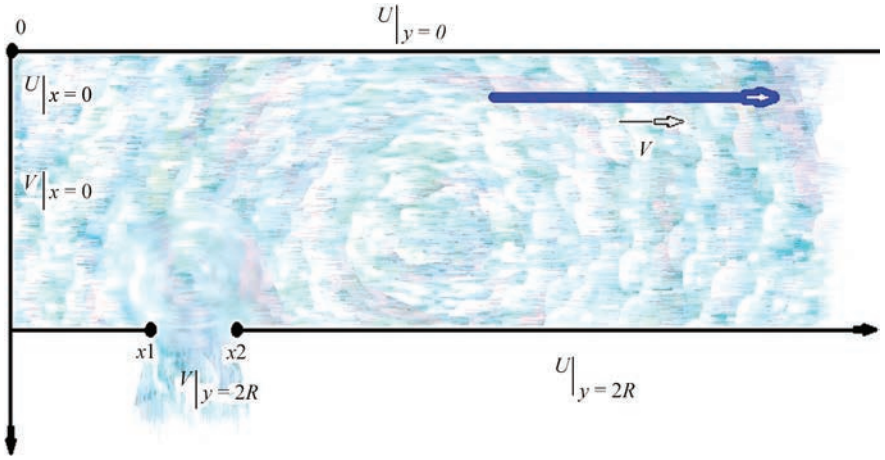

Figure 1. Flow schematic in a two-dimensional channel with leaks

is the density of the transported products; v is the coefficient of kinematic viscosity; p is the fluid pressure.

Boundary conditions are assigned as follows:

$$\begin{cases} U\Big|_{x=0} = -\dfrac{ky^2}{4\mu} + \dfrac{kR_y}{2\mu}, \\ U\Big|_{y=0} = U\Big|_{y=2R} = 0, \\ V\Big|_{x=0} = V\Big|_{y=0} = 0, \\ V\Big|_{y=2R} = \begin{cases} 0 & x < x_1, x < x_2, \\ V_{\text{leak}} & x \in [x_1; x_2], \end{cases} \end{cases} \quad (21)$$

where $[x_1, x_2]$ is the leak zone; μ is the dynamic viscosity of the transported products; R is the channel radius. For speed component $U|_{x=0}$ it is assumed that it is calculated as in the known Poiseuille model [9], which describes a stationary flow of a viscous fluid in a pipe of a round cross-section. V_{leak} is the fluid leak rate through this domain. Boundary conditions (21) can be different, depending on how the fluid leak zones are located: if they are located on different channel boundaries, then for the component of speed V the speed values will be nonzero in different segments, both at $y = 0$, and at $y = 2R$. The method of solving the above problem is known [9]. A peculiarity of solving it is the presence of discontinuous boundary conditions (21) and absence of the correct boundary conditions for pressure.

Differentiating the first equation of system (20) with respect to variable x, and the second equation with respect to variable y and allowing for the third equation of system (20), we will get Poisson's equation for determination of pressure:

$$\frac{\partial^2 p}{\partial x^2} + \frac{\partial^2 p}{\partial y^2} = -2\rho\left(\frac{\partial V}{\partial x}\frac{\partial U}{\partial y} - \frac{\partial U}{\partial x}\frac{\partial V}{\partial y}\right). \quad (22)$$

The further solution scheme is as follows:

a) a certain initial approximation of pressure $p_0(x, y)$ is assigned;

b) system (20) is solved with boundary conditions (21) with this distribution of $p_0(x, y)$;

c) after defining speed components U and V, the right-hand parts of equation (22) are calculated;

d) equation (22) is calculated with the following boundary conditions:

$$p\big|_{\partial G} = p_0(x, y); \quad (23)$$

e) after deriving the new pressure distribution, the above algorithm returns to item (*a*).

This procedure should be repeated to achieve the convergence of the iterative process. System (20) with boundary conditions (21) is solved using absolutely convergent implicit schemes of the method of alternating directions [10], and equation (22) is solved by the method of successive over-relaxation. The convergence and stability of the above iteration method was proved in work [11].

Initial approximation of pressure distribution was selected with the assumption of the existence of a linear pressure gradient along the channel, used to simulate a pipe with a leak:

$$p = p_0 - kx. \quad (24)$$

Using equation (24) for calculation of the speed field, we can establish the dependencies between the leak intensity and the change in flow configuration.

Simulation of a flow in a pipeline with defects through which the fluid leaks, is conducted for the following flow parameters, pipe geometry, properties of fluids and gases, and linear pressure gradient along the pipe length: average fluid speed in the pipeline is 2–8 m/s; characteristic small leak rate is up to 50 cm/s; dynamic viscosity of the fluid is 0.001 kg/m/s; kinematic viscosity is 0.000001 m^2/s; pressure gradient characteristic K = 0.064–0.096; step along the longitudinal coordinate is 0.08 m; step along the transverse coordinate is 0.025 m, which corresponds to a pipeline 1.25 m in diameter with 50 control points along the transverse coordinate; number of steps along the

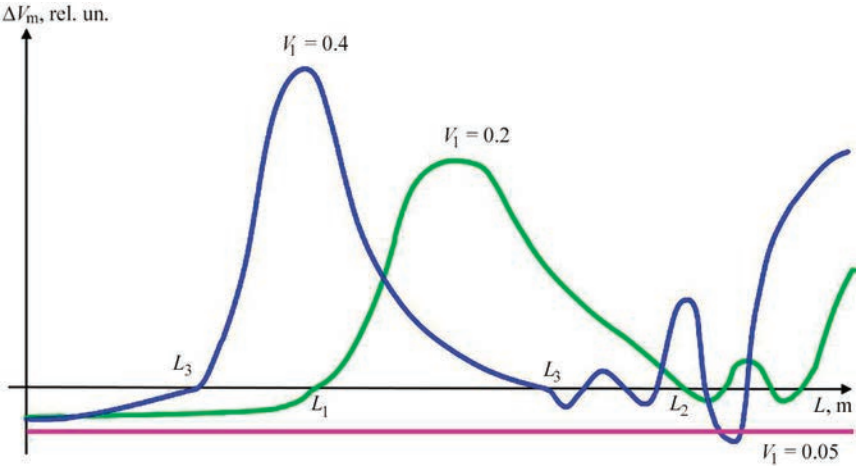

Figure 2. Dependence of the longitudinal component of speed ΔV_m and the distance to the defect at different model values of the leak rate given in conditional units

longitudinal coordinate is 90000, which allows calculation of the speed field for a 7.2 km pipe with an 8 cm step.

Analyzing the behaviour of the longitudinal component of speed in the near-wall zone, we can note a regularity, which depends on the leak rate: the greater the leak rate, the faster is the speed field monotonicity violated on the leak side (Figure 2). Moreover, the following regularity was observed: monotonicity violation, which can be defined as the difference in the speed in two points of the grid, closest to the wall:

$$\Delta V_m = V(N) - V(N-1),$$

where $N + 1$ is the number of points in the computational grid along the transverse coordinate.

Violation of the speed field monotonicity occurs by the following pattern: initially, the first monotonicity violation occurs, then the monotonicity is restored and its subsequent loss leads to loss of stability by the computational process, schematically shown in Figure 2.

Points L_3 and L_1 can serve as a flow response to a small disturbance, they correspond to the minimal distance at which the effect of the disturbance is already noticeable, while points L_4 and L_2 are the points of the loss of stability of the difference scheme. In such a case points, L_3 and L_1 can be a diagnostic feature, while L_4 and L_2 cannot be such a feature. The content of the processes occurring after these points can be as follows: either the stability of the computational procedure is lost, or the physical pattern of the flow changes, i.e. it moves from the laminar into a turbulent mode and further description of the flow requires application of other models. From the technical viewpoint such a behaviour is explained by the fact that with fluid slowing down along the pipe it is necessary to pump it up to ensure a certain pressure, flow speed and specified supply volumes, respectively. This leads to lowering of energy efficiency of the pipeline system. An important result, given in Figure 2, is the fact that at certain values of the leak rate ($V = 0.05$), no loss of fluid monotonicity is observed at all. Thus, the higher the leak rate, the faster the flow reacts to it by changing the speed monotonicity in the near-wall zone.

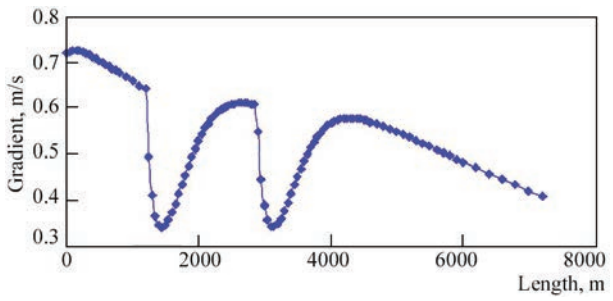

Figure 3. Dependence between the gradient of the longitudinal component of speed and presence of two leaks of different intensity located at a distance, leak coordinates $x = 1.2$ and $x = 2.88$ km

After making the appropriate calculations, we can show that at leak rate values ($V = 0.05 – 0.15$) the flow preserves its stability, i.e. both the stability of the hydrodynamic process, and the stability of the numerical scheme are in place. With increase of the leak rate, however, the pattern of distribution of the longitudinal component of the speed in the near-wall zone at different leak rates takes on a different character. In particular, the stability of the flow is lost, which is attributable to appearance of turbulent effects of the flow and a possible loss of stability of the difference method.

The developed model and numerical scheme of its implementation can be also used in diagnostics of small leaks, located at a certain distance from each other (Figure 3).

Proceeding from the results of numerical simulation of fluid flow through a channel with its leakage through the surface, the method of assessment of the coordinate of the leak point and its dependence on the leak rate was determined. It was confirmed that the problems of technical diagnostics of various-purpose systems in mathematical terms are the problems of studying the stability of the respective processes and numerical schemes of implementation of the models of such processes.

CONCLUSIONS

As a result of the conducted studies, it was proposed to take into account new informative parameters (geometrical, physical-chemical, hydrodynamic, flaw detection) during assessment of the actual technical condition and efficiency of pipeline system operation, namely:

1. Change in the cross-section of the pipeline system due to deposits of the transported technological substances, changes in the dynamic viscosity of the transported substance, and specific pressure gradient lead to development of additional stresses in the pipeline material and even appearance of an elliptical configuration of the pipeline cross-section, which may result in destruction of individual segments of the pipeline.

2. Presence of small leaks in the pipeline wall, which form as a result of corrosion, material defects, mechanical damage, leads both to loss of the transported products, and to loss of flow stability in the pipeline, formation of zones of turbulent (unstable) flow, resulting in the risk of erosion wear of the pipeline wall and development of additional stresses in the pipeline material. It this case, an inverse problem can be also solved: the developed model of fluid flow in a pipeline and numerical scheme of its realization can be used during diagnostics of small leaks, located at a certain distance from each other.

3. Value of specific pressure gradient. Increase in the specific pressure gradient results in reduction of the system energy efficiency. This lowering is indicative of insufficient supply of the transported product. Both these factors lead to violation of the standard mode of pipeline operation, and, accordingly, to changes in the physical-chemical characteristics of pipeline material.

Further investigations should be aimed at improvement of the methods of small leak detection, development of new approaches to real-time monitoring the state of pipelines and integration of mathematical models into the systems of automatic control of pipeline systems. It will allow ensuring a more accurate assessment of the technical condition of pipeline systems and preventing significant energy losses.

REFERENCES

1. Rybitskyi, I.V., Oliynyk, A.P., Yavorskyi, A.V. et al. (2019) Impact assessment of non-technological fluid accumulations in the cavity of an existing gas pipeline on the energy efficiency of its operation. *Physics and Chemistry of Solid State*, 20(**4**), 457–466. DOI: https://doi.org/10.15330/pcss.20.4.457-466
2. Doroshenko, Y., Rybitskyi, I. (2020) Investigation of the influence of the gas pipeline tee geometry on hydraulic energy loss of gas pipeline systems. *Eastern-European J. of Enterprise Technologies*, 1(**8**), 28–34. DOI: https://doi.org/10.15587/1729-4061.2020.192828
3. Konstantinov, Yu.M., Gizha, O.O. (2002) *Technical mechanics of fluids and gas:* Manual. Kyiv, Vyshcha Shkola [in Ukrainian].
4. Koichi Nakabayashi, Osami Kitoh, Voshitaka Katoh (2004) Similarity laws of velocity profiles and turbulence characteristics of Couette–Poiseuille turbulent flows. *J. of Fluid Mechanics*, **507**, 43–69. DOI: https://doi.org/10.1017/S0022112004008110
5. Dickerson, P., Worthen, J. (2024) Optimizing pipeline systems for greater precision, efficiency & safety using emerging technologies. In: *Proc. of PSIG Annual Meeting*, *Charleston, South Carolina, 7–10 May 2024*, PSIG-2426.
6. Larson, R.G. (1992) Instabilities in viscoelastic flows. *Rheol. Acta*, **31**, 213–263. DOI: https://doi.org/10.1007/BF00366504
7. Frigaard, I.A., Howison, S.D., Sobey, I.J. (1994) On the stability of Poiseulle flow of a Bingham fluids. *J. of Fluid Mechanics*, **263**, 133–150. DOI: https://doi.org/10.1017/S0022112094004052
8. Dubrulle, B., Laval, J.-P., Nazarenko, S., Zaboronski, O. (2004) A model for rapid stochastic distortions of small-scale turbulence. *J. of Fluid Mechanics*, **520**, 1–21. DOI: https://doi.org/10.1017/S0022112004001417
9. Zeytounian, R.K., Platzer, M.F. (2004) Theory and applications of viscous fluid flows. *Applied Mechanics Reviews,* 57(**3**), B15–B16. DOI: https://doi.org/10.1115/1.1760521
10. Oliynyk, A.P., Shtaier, L.O. (2012) Investigation of the influence of relaxation parameters on the convergence of the numerical method of sequential upper relaxation for the Dirichlet problem. *Carpathian Mathematical Publ.*, 4(**2**), 289–296 [in Ukrainian].
11. Bennequin, D., Gander, M.J., Gouarin, L., Halpern, L. (2016) Optimized Schwarz waveform relaxation for advection reaction diffusion equations in two dimensions. *Numer. Math.*, 134(**3**), 513–567. DOI: https://doi.org/10.1007/s00211-015-0784-8

ORCID

I.V. Rybitskyi: 0000-0003-3596-3918,
O.M. Karpash: 0000-0002-9240-1623,
V.Yu. Zapeka: 0000-0003-3143-6600,
P.M. Reiter: 0000-0002-3437-2844,
A.V. Yavorskyi: 0000-0002-5970-4286,
N.I. Chaban: 0009-0009-5839-5328

CONFLICT OF INTEREST

The Authors declare no conflict of interest

CORRESPONDING AUTHOR

I.V. Rybitskyi
Ivano-Frankivsk National Technical University of Oil and Gas
15 Karpatska Str., 76019, Ivano-Frankivsk, Ukraine.
E-mail: rybitsky@gmail.com

SUGGESTED CITATION

I.V. Rybitskyi, O.M. Karpash, V.Yu. Zapeka, P.M. Reiter, A.V. Yavorskyi, N.I. Chaban (2025) Substantiation of new diagnostic parameters of pipeline systems efficiency. *The Paton Welding J.*, **4**, 46–51.
DOI: https://doi.org/10.37434/tpwj2025.04.07

JOURNAL HOME PAGE

https://patonpublishinghouse.com/eng/journals/tpwj

Received: 26.11.2024
Received in revised form: 24.12.2024
Accepted: 24.04.2025

DEVELOPED AT PWI

WELDING IN SPACE

1984

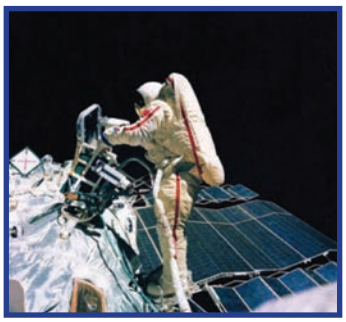

In 1984, for the first time in the world, an experiment in outer space was conducted on board the Salyut-7 orbital station to perform technological processes of welding, cutting, brazing and coating using a universal hand-held electron beam tool. The experiment lasted 3 hours and 45 minutes. This experiment is considered the beginning of the era of “space technologies”.

1998

In 1998 the equipment has passed all pre-flight testing in the NASA KS-135 flying laboratory (L. Johnson Center, NASA, Houston), six dives in the pool (at the J. Marshall Center, NASA, Huntsville) and five ascents to 6 km in the pressure chamber.

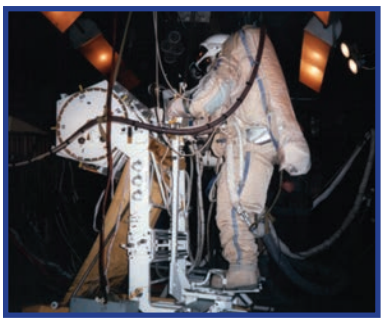

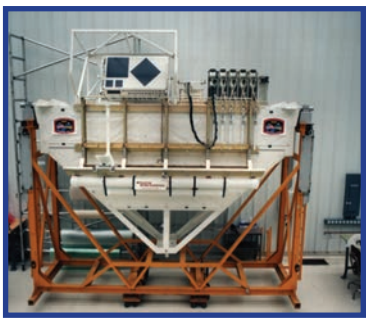

NOWADAYS

The universal electron beam gun, which is the basis of the welding tool, is capable of working both manually (when used by an astronaut-welder) and automatically as part of a robot.

For the first time, a power source that operates in a vacuum has been created.

Additive technology is being developed with application of an electron beam gun with a wire feed mechanism in a vacuum chamber for repairing damage to space objects.